

The Development of Complex Ceramic
Monoliths using Additive Manufacturing
Techniques for Methane Oxidation
Applications

C P DAVIDSON

PhD 2023

The Development of Complex Ceramic Monoliths using Additive Manufacturing Techniques for Methane Oxidation Applications

CALLUM PAUL DAVIDSON

A thesis submitted in partial fulfilment of the requirements of Manchester Metropolitan University for the degree of Doctor of Philosophy

Department of Natural Sciences

Manchester Metropolitan University

2023

Table of Contents

ABSTRACT	6
LIST OF FIGURE.....	7
LIST OF TABLES.....	10
ACKNOWLEDGEMENTS.....	11
AUTHORS DECLARATION.....	11
1. INTRODUCTION	12
1.1. Dual fuel.....	12
1.2. Natural gas	13
1.3. European emissions standards	15
1.4. Methane.....	18
1.4.1. Methane Oxidation	19
1.5. Heterogeneous Catalysis.....	20
1.5.1. Catalysis	20
1.5.2. Heterogeneous Oxidation Catalysts	21
1.5.3. Adsorption	22
1.5.4. Langmuir-Hinshelwood, Eley-Rideal and Mars-van Krevelen	23
1.6. After Treatment Systems	24
1.6.1. Catalytic Converters	24
1.7. Monoliths	27
1.8. 3D Printing Process.....	31
1.8.1. Robocast Printing	32
1.8.2. Robocast Substrates	33
1.8.3. Digital Light Processing	33
1.8.4. Ceramic Resins	34
1.9. Aims and Outlook	38
2. LITERATURE REVIEW.....	39
2.1. Methane Catalysts.....	39
2.1.1. Reaction Mechanism	40
2.1.2. Pd/Pt on Zeolite	43
2.2. 3D printed monoliths.....	44
2.3. Robocast Review.....	49
2.4. Ceramic Resin Literature Review	53
2.5. 3DP Substrate Testing	55
3. CHARACTERISATION TECHNIQUES	61
3.1. X-ray Diffraction	61
3.1.1. Crystal Structure.....	62
3.1.2. Diffraction.....	63
3.2. Brunauer-Emmet-Teller	65
3.3. Scanning Electron Microscope	67
3.3.1. Interaction of electrons with the specimen	68
3.4. X-Ray Fluorescence	70
3.5. Thermal Gravimetric Analysis	71
3.6. Shrinkage	72
4. METHODOLOGY	73
4.1. 3D Printing Methodology	73
4.1.1. Design Method	73
4.1.2. Autodesk Fusion 360.....	73
4.1.3. Ultimaker Cura.....	74
4.2. Robocast Substrate Manufacturing	74
4.2.1. Materials	74
4.2.2. Methodology	74
4.2.3. Robocast Post Processing	76

4.3. Digital Light Processing Resin Development.....	76
4.3.1. Materials	76
4.3.2. Resin Preparation	77
4.3.3. Resin Optimisation	77
4.3.3.1. Dispersant	77
4.3.3.2. Solid Loading.....	79
4.3.3.3. Photoinitiator.....	81
4.4. Digital Light Processing Manufacturing	83
4.4.1. Printing Methodology	83
4.4.2. Digital Light Processing Post-Processing	83
4.4.3. Debinding	84
4.4.4. Sintering	85
4.5. Catalyst Preparation	86
4.5.1. Materials	86
4.5.2. Sodalite Synthesis	87
4.5.3. Zeolite Precious Metal Loading	87
4.6. Catalyst Washcoat.....	89
4.7. Conclusions	89
5. SUBSTRATE MANUFACTURING RESULTS	90
5.1. Designs.....	90
5.1.1. Digital Light Processing Designs	91
5.1.1.1. Fibre Width Reduction	93
5.1.1.2. X-Plane Variation	95
5.1.2. Y-Plane Variation	97
5.1.3. Z-Plane Variation	100
5.2. Catalyst Results.....	103
5.3. 3D Printed Substrate Characterisation	106
5.3.1. Robocast Substrate Characterisation	106
5.3.2. DLP Substrate Characterisation	109
5.3.3. Conclusions	112
6. CATALYST ACTIVITY TESTING	113
6.1. Catalyst Testing Methodology.....	113
6.1.1. Testing Rig.....	114
6.1.2. Gaseous Reactant Calibration Curve	115
6.1.2.1. Methane.....	116
6.1.2.2. Carbon Dioxide.....	117
6.1.2.3. Oxygen	117
6.2. Powder Catalyst Testing Results	117
6.2.1. Substrate Testing Conditions	120
6.3. Substrate Activity Results	120
6.3.1. DLP Fibre Width	121
6.3.2. X-Axis Variation	122
6.4. Advanced DLP substrate activity testing	125
6.4.1. DLP and Commercial Substrate Comparison.....	125
6.4.2. Z-Axis Variation.....	128
6.4.3. Y-Axis Variation.....	130
6.4.4. Best Performing Substrates.....	132
6.4.5. Substrate Lifetime Study	134
7. CONCLUSIONS.....	135
8. FUTURE WORKS.....	136
9. BIBLIOGRAPHY	137

Abbreviation	Meaning
3DP	Three-dimensional printing
AM	Additive manufacturing
BET	Brunauer-Emmet-Teller
CAD	Computer-aided design
CI	Compression ignition
CC	Catalytic converter
C_d	Cure depth
C_{dmax}	Maximum cure depth
CPSI	Channels per square inch
CSL	Ceramic stereolithography
DLP	Digital light processing
D_p	Penetration depth
E_0	Applied energy dose
E_c	Critical energy dose
ECU	Engine control unit
ER	Eley-Rideal
EU	European union
HC	Hydrocarbons
LDM	Liquid deposition modelling
LH	Langmuir-Hinshelwood
LNG	Liquid natural gas
LPG	Liquid petroleum gas
MVK	Mars-van Krevelen
OEM	Original equipment manufacturer
OFA	Open frontal area
PM	Particulate matter
RI	Refractive index
SEM	Scanning electron microscope
SI	Additive manufacturing
Tcf	Trillion cubic feet
TGA	Thermal gravimetric analysis

TWCC	Three-way catalytic converter
XRD	X-ray diffraction
XRF	X-ray fluorescence

Abstract

The research presented examines the use of 3D printing for ceramic catalytic substrates. The main aim was to try and reduce the amount of methane emissions being emitted from a dual fuel exhaust stream by utilising a more effective catalytic converter and using 3D printing to achieve this. The motivation for this thesis was initiated by G-Volution Ltd, who funded this project and owns a patent for a unique dual fuel system which can be fitted to any diesel engine, but which currently emits more methane than is allowed by EU regulations. To begin, CAD software was used to design monolithic substrates with a more complex internal channel structure than those seen in conventional, extruded monoliths. These substrates were manufactured using two different AM techniques: robocasting and digital light processing. A unique, in-house, photosensitive ceramic resin was synthesised to print intricate ceramic substrates. This required intensive research to produce, as this is not something which was available in literature or on the commercial market at the time of printing. This was the most time-consuming part of the thesis due to the difficulty of the synthesis process and the number of components required and is considered as the greatest achievement of this project. Characterisation techniques for the manufacturing material and final substrates included XRF, XRD, SEM, and TGA. A total of 16 substrates were manufactured using the named AM techniques with designs based on the stacking of individual, layered fibres rotated along different axes. To compare these designs catalytically, each substrate was washcoated in the same catalyst and tested for the complete oxidation of methane using a purpose-built testing rig. A commercial 400 CPSI monolith was subject to the

same wash coating procedure for comparison. All the 3D printed designs tested outperformed the commercial 400 CPSI monolith at every temperature. The best 3D designs tested showed three times improved methane conversion at a temperature of 425 °C. The results explaining the designing, manufacturing and characterisation of these substrates, along with the catalytic testing results, will follow.

List of Figure

- Figure 1: Various depictions of the methane molecule.³⁴
- Figure 2: Energy level diagram for the complete oxidation of methane.
- Figure 3: The effect of high-temperature sintering on a catalyst's active component.⁴³
- Figure 4: An image displaying steps one to five of catalytic adsorption.⁴⁵ Figure 5: The three most common catalytic mechanisms. From left to right: Langmuir-Hinshelwood, Eley-Rideal and Mars-van Krevelen.⁴⁶
- Figure 6: The internal structure of a catalytic converter.⁴⁸
- Figure 7: A detailed breakdown of a catalytic converter.⁵²
- Figure 8: A labelled diagram of a singular monolithic channel in a catalytic converter.⁵²
- Figure 9: The relationship between a monolith and its structural parameters. Figure 10: CFD images taken from a study by A. Doyle and S. Hajimirzaee investigating 3D printed substrates, showing the turbulent kinetic energy inside the channels.⁶⁹
- Figure 11: Steps of the 3D printing process.⁷⁵
- Figure 12: (Left) Schematic of Robocast 3D printer.(Right) A Delta WASP 4070 3D printer.^{77,78}
- Figure 13: (Left) A schematic of the Digital Light Processing 3D printer. (Right) A Photocentric Liquid Crystal Precision 1.5 DLP 3D printer.⁸³
- Figure 14: Radical cleavage mechanism.⁹⁰
- Figure 15: A schematic showing the light scattering phenomena which can occur within a ceramic resin.¹⁰¹
- Figure 16: Proposed MVK mechanism for the complete oxidation of methane over a PdO surface.¹²⁸
- Figure 17: CAD designs produced by Alketan et al. ¹⁴⁸
- Figure 18: Resin substrates produced by J. Manzano et al. and their CAD designs.¹⁴⁹ Figure 19: Temperature contour of a honeycomb 400 CPSI monolith (Top) and a 3D printed diamond lattice substrate (Bottom).¹⁵⁰
- Figure 20: The two titanium ceramic allow cube designs produced by Van Noyen et al.¹⁵³
- Figure 21: The design produced by Stuecker et al., including the final ceramic substrate and the commercial substrate used for comparison.¹⁵⁴
- Figure 22: An image of the 3D printed cylindrical monolith taken from the publication by C. Leclerc and R. Gudgila referred to above.¹⁵⁵
- Figure 23: Images taken from a publication by A. Doyle and S. Hajimirzaee showing four designs printed using robocast technology.⁶⁹

Figure 24: A commercial size 3D printed catalytic converter, tested under industrial conditions, taken from a publication by A. Doyle et al.¹⁵⁶

Figure 25: Image of the Al₂O₃ 3D printed substrate used for testing by Santoliquido et al.¹⁰¹

Figure 26: CAD designs of three substrates produced for gaseous catalytic studies by Kovacev et al.¹⁷⁵

Figure 27: Images of the final washcoated substrates tested by Kovacev et al.¹⁷⁵

Figure 28: XRD pattern of a Faujasite zeolite.¹⁷⁷

Figure 29: An example of a crystal plane with the miller index (2,1,0). Figure

30: The interaction of X-rays with a crystal structure during X-ray diffraction.¹⁸³

Figure 31: Nitrogen adsorption isotherms.¹⁸⁸

Figure 32: A Micrometrics ASAP 2020 instrument.¹⁹⁰

Figure 33: A typical SEM instrument set-up.¹⁹³

Figure 34: The behaviour of an SEM electron beam with the sample surface.¹⁹⁴

Figure 35: SEM image of a 1.0 wt.% Pt/zeolite beta catalyst.¹⁹⁷

Figure 36: The behaviour of electrons within an atom during X-ray fluorescence analysis.²⁰²

Figure 37: (Top) A Perkin 400 TGA instrument. (Bottom) An example of a result graph produced by a Perkin 400 TGA instrument.^{205, 206}

Figure 38: Images of the WASP Delta 4070 robocast printer used in this study.

Figure 39: Image of the robocast substrates printed, with a variation in the X-angle, before post-processing.

Figure 40: Sedimentation height v time of 6 samples with a varying dispersant concentration, percentage recorded as a wt.% of the solid content, and a fixed solid loading (40 wt.%).

Figure 41: Viscosity v solid loading with solid loading recorded as wt. % of the total resin.

Figure 42: Seven samples with a varying photoinitiator concentration (recorded as wt.% of the total resin) v cure depth after being exposed to UV light for four separate time intervals.

Figure 43: TGA results displaying the weight loss of two samples as temperature increases.

Figure 44: The temperature profile applied to the green body sample.

Figure 45: CAD design of a 0.7 mm, 90° woodstock pile monolith.

Figure 46: CAD design of a 0.4 mm, 90° woodstock pile monolith.

Figure 47: CAD design of a 0.5 mm, 90° woodstock pile monolith.

Figure 48: The CAD design of a 0.6 mm, 90° woodstock pile monolith.

Figure 49: A series of graphs comparing the surface area, open frontal area, number of exposed faces and CPSI of 90° woodstock pile designs with a fibre width of 0.4, 0.5, 0.6 and 0.7 mm.

Figure 50: CAD design of a 0.5 mm, 30° fibre rotation in the X-plane monolith.

Figure 51: CAD design of a 0.5 mm, 45° fibre rotation in the X-plane monolith.

Figure 52: CAD design of a 0.5 mm, 60° fibre rotation in the X-plane monolith.

Figure 53: CAD design of a 0.5 mm, 75° fibre rotation in the X-plane monolith. Figure

54: A series of graphs comparing the surface area, open frontal area, number of exposed faces and CPSI of designs with a fibre width of 0.5 mm rotated in the xplane by 30°, 45°, 60° and 75°.

Figure 55: CAD design of a 0.5 mm, 5° fibre rotation in the Y-plane monolith.

Figure 56: CAD design of a 0.5 mm, 10° fibre rotation in the Y-plane monolith.

Figure 57: CAD design of a 0.5 mm, 15° fibre rotation in the Y-plane monolith.

Figure 58: CAD design of a 0.5 mm, 30° fibre rotation in the Y-plane monolith.

Figure 59: A series of graphs comparing the surface area, open frontal area, number of exposed faces and CPSI of designs with a fibre width of 0.5 mm rotated in the Yplane by 5°, 10°, 15° and 30°.

Figure 60: CAD design of a 0.5 mm, 7.5° fibre rotation in the Z-plane monolith.

Figure 61: CAD design of a 0.5 mm, 10° fibre rotation in the Z-plane monolith.

Figure 62: CAD design of a 0.5 mm, 15° fibre rotation in the Z-plane monolith.

Figure 63: CAD design of a 0.5 mm, 30° fibre rotation in the Z-plane monolith. Figure 64: A series of graphs comparing the surface area, open frontal area, number of exposed faces and CPSI of designs with a fibre width of 0.5 mm rotated in the Zplane by 7.5°, 10°, 15° and 30°.

Figure 65: XRD pattern for each zeolite synthesised and tested.

Figure 66: Images of the printed robocast substrates being measured using a microcaliper .

Figure 67: SEM images of the 90° robocast substrate after sintering but before wash coating. A & B=Cross sectional image of the substrate face in the direction of gas flow. C= Internal image of the substrate showing the build of the individual Figure 68: A-D: Images of the green body and ceramic substrate produced using DLP technology being measured using a microcaliper. E: A side image of both the green body before and after heat treatment.

Figure 69: SEM images of the DLP substrate. A: An image of the individual horizontal fibre. B: An image of the cross-section of the substrate. C: An image of the internal cross-section showing the individual layers used to build up the monolith.

Figure 70: SEM images of the ceramic substrate produced using DLP technology. A: An image of the cross-section of the substrate. B: An image of an individual horizontal fibre.

Figure 71: Image of a 0.5mm 90° wood stockpile design after the catalyst washcoat has been applied.

Figure 72: A photograph(top) and schematic(bottom) of the testing rig.

Figure 73: Calibration curve for methane. Figure 74: Calibration curve for carbon dioxide Figure 75: Calibration curve for oxygen.

Figure 76: Light-off curve for each catalyst synthesised. Flow Rate = 100ml/min. Gas Composition: He= 85 %, O₂=10 %, CH₄=5 %.

Figure 77: Light-off curves for five individual samples of the HY-PdPt batch catalyst synthesised. Flow Rate = 100ml/min. Gas Composition: He= 85 %, O₂=10 %, CH₄=5 %.

Figure 78: Light-off curve for 90° wood stockpile design, DLP printed substrates with a reducing fibre width. Flow Rate = 100ml/min. Gas Composition: He= 85%, O₂=10%, CH₄=5%.

Figure 79: Light-off curve for DLP printed substrates with 0.5mm wide fibres rotated along the X-axis. Flow Rate = 100 ml/min. Gas Composition: He= 85 %, O₂=10 %, CH₄=5 %.

Figure 80: Light-off curve for robocast printed substrates with 0.7 mm wide fibres rotated along the X-axis. Flow Rate = 100 ml/min. Gas Composition: He = 85 %, O₂ = 10 %, CH₄ = 5 %.

Figure 81: Light-off curve for three samples of a 400 CPSI commercial monolith. Flow Rate = 100 ml/min. Gas Composition: He = 85 %, O₂ = 10 %, CH₄ = 5 %.

Figure 82: Light-off curve for four 90 woodstock pile DLP printed substrates with a 0.5 mm fibre width. Flow Rate = 100 ml/min. Gas Composition: He= 85 %, O₂ = 10 %, CH₄ = 5 %.

Figure 83: Light-off curve for four DLP printed substrates with a 0.5 mm fibre width and rotation of the fibres in the Z axis. Flow Rate = 100 ml/min. Gas Composition: He = 85 %, O₂ = 10 %, CH₄ = 5 %.

Figure 84: Light-off curve for four DLP printed substrates with a 0.5 mm fibre width and rotation of the fibres in the Y-axis. Flow Rate = 100 ml/min. Gas Composition: He = 85 %, O₂ = 10 %, CH₄ = 5 %.

Figure 85: Light-off curve for the best-performing DLP printed substrate from each design category and a commercial substrate. Flow Rate = 100 ml/min. Gas Composition: He = 85 %, O₂ = 10 %, CH₄ = 5 %.

Figure 86: Light-off curve for a study of the lifetime of a 90° woodstock pile design substrate with a 0.5mm fibre width. Flow Rate = 100 ml/min. Gas Composition: He = 85 %, O₂ = 10 %, CH₄ = 5 %.

List of Tables

Table 1: Typical composition of LNG.¹⁰

Table 2: Heat value of petrol, diesel and LNG by mass and volume.¹⁴

Table 3: Euro VI emissions limits for passenger vehicles.²⁴

Table 4: Euro VI emissions limits for heavy-duty vehicles.²⁵

Table 5: Final % composition of the photosensitive ceramic resin produced.

Table 6: The physical properties of each DLP monolith design tested.

Table 7: XRF and BET data from the catalysts tested. (*=company data) Table 8: Dimensions of the 3D substrate printed using the digital light processing technique.

Table 9: Properties of the substrates designed with a reduced fibre width.

Table 10: Properties of the DLP substrates designed with rotated fibres along the Xaxis.

Table 11: Properties of a DLP-90°-0.5mm fibre width substrate and a commercial monolith.

Table 12: Properties of a DLP substrate with 0.5 mm fibres rotated along the Z-axis.

Table 13: Properties of a DLP substrate with 0.5 mm fibres rotated along the Y-axis.

Table 14: Properties of the best performing DLP substrate and a commercial monolith.

Acknowledgements

As the author of this thesis, I would like to begin by acknowledging those who helped me achieve this. Starting with a very important thank-you to G-Volution who were key in funding this project and gave me a starting point for the direction of my studies. This would not have been possible without your support and I'm extremely grateful for the opportunity. I would also like to thank my principal supervisor, Dr. Aidan Doyle, who guided me through the project and offered scientific support and professional mentorship at times when I was not even aware it was required. This project would not have become what it did without your trust to allow me to explore my somewhat unusual ideas so thank you. Thank you to the technical staff for assisting me with numerous instruments throughout the lab, namely Dr. Gary Miller and Dr. Hayley Andrews who were key in some of my most important analysis. Thank you to Dr. Lubomira Tosheva who played a more important role than probably realised. Although not directly part of my supervisory team, your presence and advice around my project were exactly what was needed at what always seemed to be the right time. Thank you to my family who had to put up with my scientific jargon talk around the dinner table on numerous occasions whilst still not understanding most of what I said. Finally, thank you to my friends who spent many late nights, coffee breaks and beers helping to keep me grounded throughout. You know who you are, and this thesis would not have been possible without the support of all of you.

Authors Declaration

I declare that this thesis has been completed solely on my own and has not been submitted in whole or part, in any previous application for a degree. Unless stated otherwise by reference or acknowledgement, the work presented is entirely my own.

1. Introduction

1.1. Dual fuel

Dual fuel systems are a thoroughly investigated alternative to purely diesel engines. Examples of dual fuels include liquid petroleum gas (LPG), biofuels and liquid natural gas (LNG).¹ Introducing these alternative fuels decreases the dependency on diesel whilst also improving the environmental effects of burning diesel alone.

Extensive research has proven that introducing these dual fuels is a viable alternative to enhance the diesel engine.² In dual fuel mode, modified CI engines can lead to higher performance, lower CO₂, particulate matter and smoke emissions, reduced running costs and the critical factor of less dependence on diesel.³

Dual fuel engines are a modified version of the diesel compression engine. They all use a combination of CI and SI engine technology to improve performance. The dual fuel of choice (called the primary fuel) is mixed with air in the engine's cylinders. The piston then begins to compress the mixture, but the fuel does not auto-ignite due to the primary fuel's high ignition temperature. A small amount of diesel is injected towards the end of the compression cycle, which auto-ignites like in a diesel CI engine. This acts as a deliberate auto igniter for the primary fuel-air mixture, which then combusts, providing further energy for the piston's power stroke and the engine's mechanical movement.⁴ The engine can also be switched back to pure diesel mode with relative ease if required. The main cost challenges come with the availability and cost of the dual fuel supply, which recent history has shown can be volatile based on international affairs.⁵ The benefits of dual fuel are, therefore, a

cost-saving by reduced use of diesel (approximately three years payback of retrofit costs) and reduced emissions by using methane/natural gas.

G-Volution, the key funder for this project, have patented a unique Optimiser system which can help manage an engine as it runs under dual fuel conditions.⁶ The technology allows one or more primary fuels to be injected to co-combust with diesel without affecting the engine operation. The optimiser imitates the primary injector's pulse signal being sent to the engine control unit (ECU), which confirms the amount of fuel required by the throttle demand. By intercepting the fuel injector control signal, the optimiser can map the original fuel demand and separate it into demands for several fuels, such as LNG being used as the dual fuel. By introducing this optimiser, the original equipment manufacturer (OEM) and the ECU remain the controlling input for the engine control loop. The optimiser acts as a ghost intermediate, translating the fuel control signal and managing the alternative fuel system, unaffected the ECU operation.

The engine power features are preserved as the engine is still constantly running on the original OEM ECU mapping – just with an unnoticed adjustment by the optimiser. The optimiser then has the power to adjust the diesel dual-fuel ratio, effectively ensuring no difference in the engine's performance or response. This includes emission control strategies and system safety operations as the OEM ECU is unaffected.⁷ Their most recent project - the conversion of a 180 Grand Central DMU freight train – including others, has primarily been fitted using LNG as the dual fuel source.⁸

1.2. Natural gas

LNG is an excellent sustainable fuel source for dual fuel systems. It is projected that global energy demand is increasing daily, increasing the output of greenhouse gas

emissions and adding further strain to the demand for diesel as the world aims to move away from unsustainable fuels.⁹ LNG mainly comprises of methane (over 85%) along with ethane, propane, butane, carbon dioxide and nitrogen, all of varying concentrations depending on the LNG source.^{10, 11}

Table 1: Typical composition of LNG.¹⁰

Name	Methane	Ethane	Propane	Butane	Pentane	Carbon Dioxide	Nitrogen
Formula	CH ₄	C ₂ H ₆	C ₃ H ₈	C ₄ H ₁₀	C ₅ H ₁₂	CO ₂	N ₂
Volume %	<85	3-8	1-2	<1	<1	1-2	1-5

LNG is a non-toxic, non-corrosive, colourless and odourless liquid which forms when natural gas is cooled to below -162 °C.¹² It can be collected from underground reserves using a technique known as fracking.¹³

Diesel and LNG heat values are similar, valued at 42-46 MJ/kg and 42-56 MJ/kg, respectively.¹⁴ When considering the density - with diesel weighing 0.846 kg/L compared to LNG at 0.428 kg/L – the energy value for diesel is around 34 - 36 MJ/L, and LNG is about 20 - 24 MJ/L, which means that LNG has approximately 42% less energy per litre of fuel.¹⁵ This has been investigated in various dual-fuel engine efficiency studies. However, with many reports only reporting a maximum decline of 2.1 % in engine efficiency, many consider it a small compromise to reduce emission output whilst simultaneously reducing diesel consumption.¹⁶

Table 2: Heat value of petrol, diesel and LNG by mass and volume.¹⁴

Fuel Type	Higher Heat Values*	
	MJ/Kg	MJ/L
Petrol	46.4	34.2
Diesel	45.6	38.6

LNG	55.2	23.6
-----	------	------

**Results vary based on changes in the exact fuel composition.*

A study in the Netherlands showed that diesel trucks using LNG dual fuel reduced greenhouse gas emissions by around 10-15%. This includes reductions in SO₂, NO_x, CO₂, and PM.¹⁷ However, increases in CO and HC can be seen when running under dual fuel mode with LNG, as reported in the literature.¹⁸ The main HC to increase is methane, mostly because the main component of LNG is methane. Although methane has a lower carbon ratio than any other HC - which partly explains the reduction in CO₂ emissions - it is also one of the most energy-intensive HCs to oxidise, which explains the higher concentration within the emissions stream. So, although methane is abundant on the planet, making it a valuable energy source when trying to move away from crude oil sources, the issue of methane slip remains a problem in the exhaust emissions of dual-fuel vehicles.^{19, 20}

G-Volution is the funder behind this project and a collaboration came about to try and solve this problem that occurs with dual fuel systems. This became the first and ultimate aim of the project, which was to reduce the amount of methane emissions produced from an engine exhaust system. The strategy for this is discussed in further detail throughout this introduction. To take their optimiser product to a larger market, they must first reduce the amount of emissions emitted by a dual fuel system. Currently, the amount of methane emitted surpasses the legal standards set by the European Union.

1.3. European emissions standards

Legislation to limit the volume of harmful vehicle emissions has been implemented since the 1970s. The European Union (EU) sets the most stringent of these.

However, this is not limited to just Europe, with 17/20 G-20 countries following the guidance set by the EU. The current European pathway consists of six stages of increasingly stringent emission limits, the most recent being the Euro VI.²¹ The Euro VI mainly focuses on reducing NO_x, HCs and PM for light- and heavy-duty vehicles, in addition to more stringent limits for diesel passenger cars.^{22, 23} Table 1 and 2 below display how the Euro emissions legislation have progressed over time for diesel vehicles.

Table 3: Euro VI emissions limits for passenger vehicles.²⁴

	Legislative Stage	Year Introduced	CO	HC	NO _x	PM
			g/km			
Passenger Vehicle	Euro I	1992	2.720	0.970	-	0.140
	Euro II	1996	1.000	0.700	-	0.080
	Euro III	2000	0.640	0.560	0.500	0.050
	Euro IV	2005	0.500	0.300	0.250	0.025
	Euro V	2009	0.500	0.230	0.180	0.005
	Euro VI	2014	0.500	0.170	0.080	0.005

Table 4: Euro VI emissions limits for heavy-duty vehicles.²⁵

	Legislative Stage	Year Introduced	CO	HC	NO _x	PM
			g/kWh			
Heavy-Duty Vehicle	Euro I	1992	4.500	1.100	8.000	0.612
	Euro II	1996	4.000	1.100	7.000	0.150
	Euro III	2000	2.100	0.660	5.000	0.100
	Euro IV	2005	1.500	0.460	3.500	0.020
	Euro V	2008	1.500	0.460	2.000	0.020
	Euro VI	2013	1.500	0.130	0.400	0.010

Since the euro emissions standards started, the accepted level of emissions has dropped drastically. For example, for heavy-duty vehicles, CO has been reduced by 66.7%, HC by 88.2%, NOx by 99.5% and PM by 98.4%. This is partly due to the development of exhaust after-treatment systems and the improvement in their technology over the last few decades. Nevertheless, is this enough?

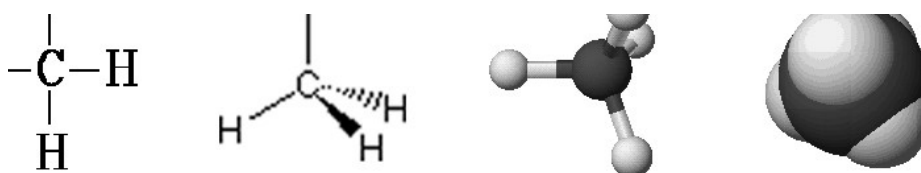
Diesel engines were accountable for powering over 90 % of heavy freight-moving vehicles throughout Europe in 2019.^{26, 27,28} They produce an array of pollutant emissions, with the main four being carbon monoxide (CO), hydrocarbons (HC) such as methane (CH₄), nitrous oxides (NOx) and particulate matter (PM).²⁹ These pollutants are partly responsible for enhancing the greenhouse effect. The increased atmospheric concentration of these gases means less heat can leave the atmosphere, increasing the environmental temperature and contributing to the climate crisis.³⁰

The transport sector contributes significantly to this problem, accounting for around 14% of all global CO₂ emissions. Other industries contributing significantly include energy systems (34 %), industry such as cement, steel, and chemicals (24 %) and agricultural land use (21 %). The largest sub-sector within transportation is road transport for passenger and freight, accounting for nearly 73% of the entire sector's emissions in 2018. This is partly due to the rapid increase of motor vehicles worldwide.³¹ The world health organisation estimated that around 2.4 million people die annually due to air pollution, with billions of pounds spent on medical bills and loss of productivity yearly. Some health effects include respiratory infection, asthma exacerbation, chronic bronchitis, and premature mortality.³² To prevent the effects of these pollutants, many organisations (EPA, OECD, IPCC, IEA, EEA) have

emphasised the importance of constantly needing to improve legal arrangements and advancing technological developments.³³

G-volution's ideas to incorporate dual fuel systems help to combat a reduction in most emissions, but this is not the case for methane. A possible solution to this problem was examined in detail, with an idea around enhancing the catalytic efficiency of the exhaust after-treatment process discussed. Firstly, a further understanding of methane and its catalytic behaviour was researched.

1.4. Methane



Methane (CH₄) is an alkane molecule with a tetrahedral 3-dimensional shape containing one carbon bonded to 4 hydrogens with a bond angle of 109.5°.³⁵ Figure 1 displays various representations of a methane molecule. Carbon has an electronic structure of 1s²2s²2p_x¹2p_y¹. The 1s² electrons are too deep within the atom to be involved in bonding, leaving the remaining 4 electrons. When carbon bonds, one of the electrons from the 2s² orbital is promoted to the 2p_z orbital (as there is only a small energy gap difference), promoting the carbon into the 'excited state'. The orbitals rearrange themselves into four identical and singly occupied orbitals called sp³ hybrids in a process known as hybridisation.³⁶ Visually, the sp³ orbitals arrange themselves as far apart as possible, with the nucleus at the centre of a tetrahedron

shape and the orbitals pointing to each corner. When hydrogen bonds with carbon, the one electron from hydrogen's sp^1 orbital, forms a covalent bond with an electron from carbon's sp^3 orbital, forming a new molecular orbital containing both electrons and creating a strong C-H σ bond.³⁷

1.4.1. Methane Oxidation

The oxidation of methane is an exothermic process hindered by a significantly high energy barrier of activation due to the highly stable C-H bonds. Figure 2 shows an energy level diagram of the reaction. When fully oxidised, CH_4 forms CO_2 and H_2O but requires substantial energy to do so. Firstly, CH_4 has the highest hydrogen-to-carbon ratio of any hydrocarbon, with the C-H bond energy lying relatively high for such compounds, around 440 kJ/mol. This is partially due to the symmetry within the molecule resulting in a lack of a dipole. The CH bonds of the first intermediate oxygen-containing species (CH_3OH) become weaker than the initial CH_4 molecules and thus oxidise more easily, meaning the reaction does not stop at the intermediate stage but continues to produce CO_2 .³⁸

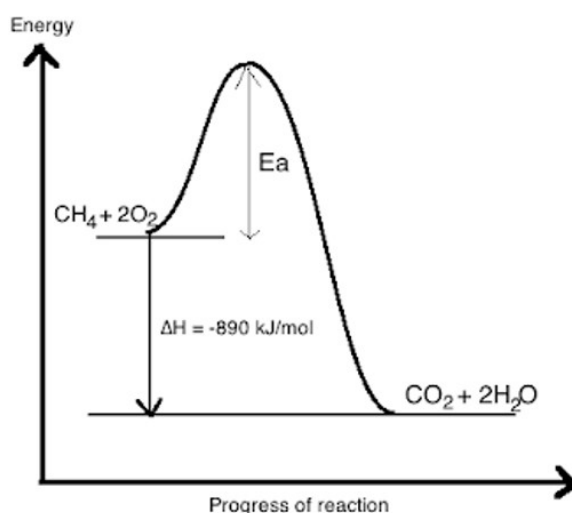


Figure 2: Energy level diagram for the complete oxidation of methane.³⁹

The donating of an electron into the C-Hs* orbital is sterically hindered and energetically tricky, reducing the susceptibility of a nucleophilic attack. CH₄ also has an extremely low pKa near 40, resulting in a very low proton affinity (544 kJ/mol), rendering activation by acid/base very difficult. The homolytic C-H bond cleavage and hydrogen atom transfer using a catalyst is generally accepted as the most common way of activating methane. This is relevant for this thesis as one of the main aims of this work is to try and reduce the amount of methane produced by an engine exhaust using catalytic techniques. The activation energies of oxidising methane are achievable within a vehicle's exhaust system, meaning the objective of catalysing the molecule is an attainable reaction. This will be discussed in further detail later in the introduction.

1.5. Heterogeneous Catalysis

1.5.1. Catalysis

Without catalysis, the 21st-century chemical industry as we know it would not exist. It is responsible for some of the most well-known reactions producing some of the world's most popular chemicals, such as the Haber-Bosch process, which produces ammonium for fertilisers.⁴⁰ A catalyst is responsible for reducing the activation energy of a reaction by providing an alternative route, all while remaining unchanged by the end of the reaction. It does so by offering a weaker intermediate bond which lowers the energy of the transition state and compensates for part of the energy required to break the activation bond in the reactant before a new bond takes over, creating a further stable product.⁴¹

Catalysts can be in the form of atoms, molecules, solid surfaces or even enzymes, all depending on the reaction. When the products/reactants are in a different phase from the catalyst, this is known as heterogeneous catalysis – a driving force behind the petrochemical industry.

1.5.2. Heterogeneous Oxidation Catalysts

As an introductory example and to stay relevant to the studies conducted in this thesis, the complete oxidation of methane will be used as an example to explain heterogeneous catalysis further. A typical catalyst for oxidation usually consists of precious metal (such as Pd or Pt) dispersed over a solid surface.³⁸

The solid surface acts as a support to help immobilise and stabilise the precious metal particles, decreasing their surface energy and preventing them from sintering together as quickly, as shown in Figure 3. This is an undesirable side effect of catalysts, as sintering hinders their performance by reducing the accessibility of the active sites.⁴² The active sites are the individual locations where adsorption occurs before a catalytic reaction takes place. The solid surface can play an essential role in the catalyst's success. Factors such as surface area, porosity, costs, and chemical stability are considered when selecting the catalyst support.⁴³

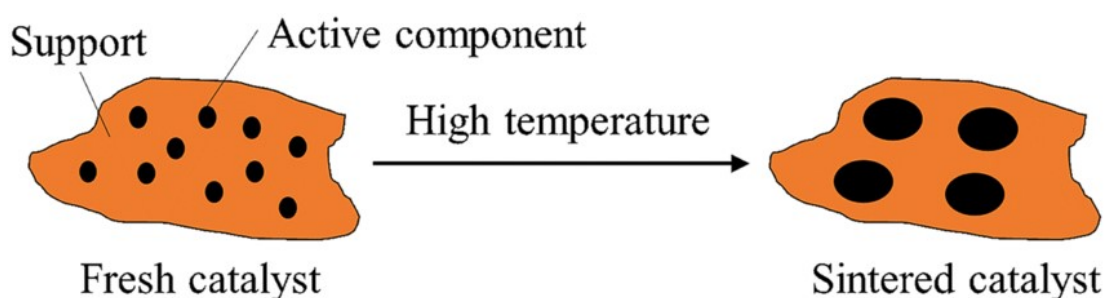


Figure 3: The effect of high-temperature sintering on a catalyst's active component.⁴⁴

As the reactants approach the catalyst, all or at least one adsorb onto the catalyst's surface, where the reaction will occur. Adsorption proceeds any heterogeneous catalytic reaction.⁴⁵

1.5.3. Adsorption

Heterogeneous catalytic reactions ultimately undergo five steps.

- 1) Reactant diffusion to the active surface.
- 2) Reactant adsorption onto the surface.
- 3) Reaction on the surface.
- 4) Product desorption from the surface.
- 5) Product diffusion away from the surface.

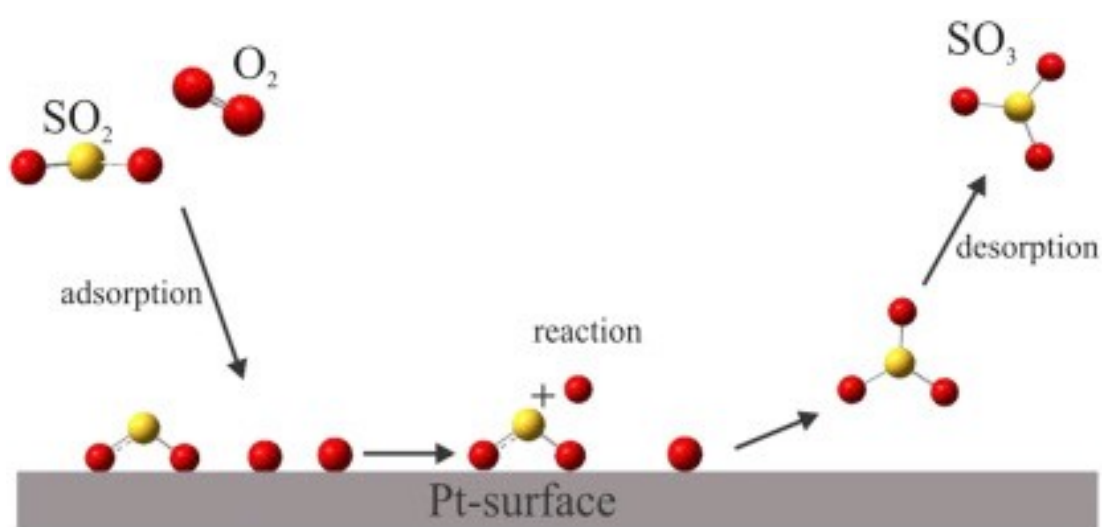


Figure 4: An image displaying steps one to five of catalytic adsorption.⁴⁶

The two main types of adsorptions are physisorption and chemisorption.

Physisorption occurs when the adsorbate gas molecules are held by physical forces such as Van Der Waals. Chemisorption occurs when the adsorbate molecule is held to the surface by chemical forces such as covalent bonds, which arise by sharing electrons. The oxidation of hydrocarbons on metallic surfaces is understood to be a

chemisorption process. Models have been created to describe further how the adsorption of reactants occurs.

1.5.4. Langmuir-Hinshelwood, Eley-Rideal and Mars-van Krevelen

Several different adsorption mechanisms have been proposed for the catalytic oxidation of some gaseous pollutants. The most common include the Eley-Rideal (ER), Langmuir-Hinshelwood (LH) and Mars-van Krevelen (MVK) mechanisms. They mainly differ as one mechanism includes one molecule adsorbed on the surface, whilst the other two include two molecules adsorbed on the surface with a slightly different reaction pathway.

During the ER mechanism, one molecule is chemisorbed onto the catalyst's surface. The second molecule passes by in gaseous form and interacts with the one adsorbed on the surface. The reaction occurs, and the newly formed molecule desorbs from the surface.

For the LH mechanism, the two reactant molecules each adsorb onto the surface. The molecules diffuse across the surface until they are close enough to react. An atomic reorganisation of the species occurs on the surface of the catalysts, and the newly formed product desorbs from the surface.

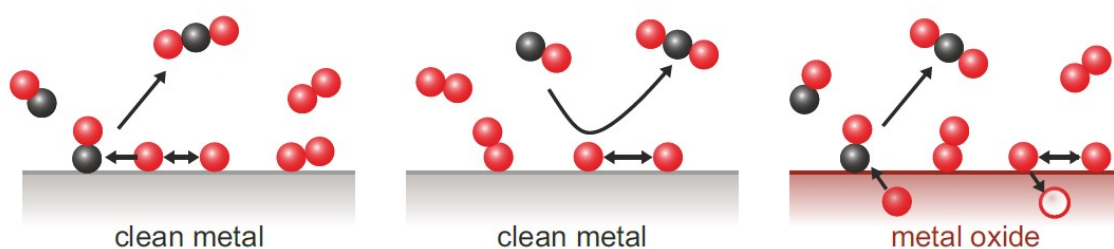


Figure 5: The three most common catalytic mechanisms. From left to right: Langmuir-Hinshelwood, Eley-Rideal and Marsvan Krevelen.⁴⁷

The third mechanism is the MVK mechanism and is most like the LH mechanism meaning they can be challenging to tell apart. The MVK method involves a redox process. The reductive reactant is adsorbed onto the catalyst surface and oxidised by a lattice O^{2-} . The product is then desorbed from the surface and diffused into the bulk gaseous phase. The oxygen vacancy site is then simultaneously replenished by the surface adsorption and diffusion of gaseous O_2 and lattice O^{2-} diffusion. Figure 5 summarises the three main mechanisms. The catalyst type can influence the mechanism. For example, the MVK mechanism relies on an oxygen-rich lattice such as an oxide catalyst.

To try and reduce the amount of methane emissions produced by an engine exhaust stream, it was concluded improving the catalysis process in the engines exhaust after treatment system was the most practical and attainable way to achieve this.

1.6. After Treatment Systems

1.6.1. Catalytic Converters



Figure 6: The internal structure of a catalytic converter.⁴⁸

Catalytic converters (CC) were introduced as a concept by Eugene Houdry in the 1950s to tackle the effect of exhaust emissions.⁴⁹ It was not until the 1970s that the

first mass-produced CC was created and added to vehicles as part of legal requirements.⁵⁰ In the last 30 years, significant advancements have made the CC the most effective technology for reducing exhaust emissions. Compared to no CC, exhaust emissions are reduced by up to 80 % making them one of the scientific success stories for environmental concerns.⁵¹ CCs simply consist of a block of material (usually a metal or ceramic) containing many microchannels coated in a catalyst. The catalyst itself is in the solid phase, whilst the reactants and products are all in the gas phase. The catalyst usually comprises of precious metals on an alumina or zeolite surface where the reaction occurs.⁵² Figure 6 shows the inside of a standard CC. The toxic gases produced after fuel combustion flow into these channels, where they react with the catalyst to produce fewer toxic gases as a product. The most common modern CC is a Three-Way catalytic converter (TWCC) and contains three main components.⁵³ These main components are the substrate (usually referred to as a monolith), the washcoat and the catalyst. Figures 7 and 8 show a CC in more detail.

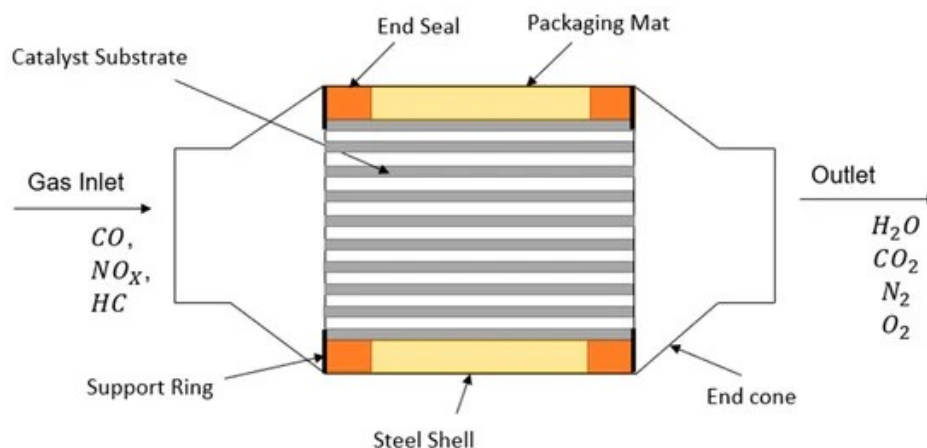


Figure 7: A detailed breakdown of a catalytic converter.⁵³

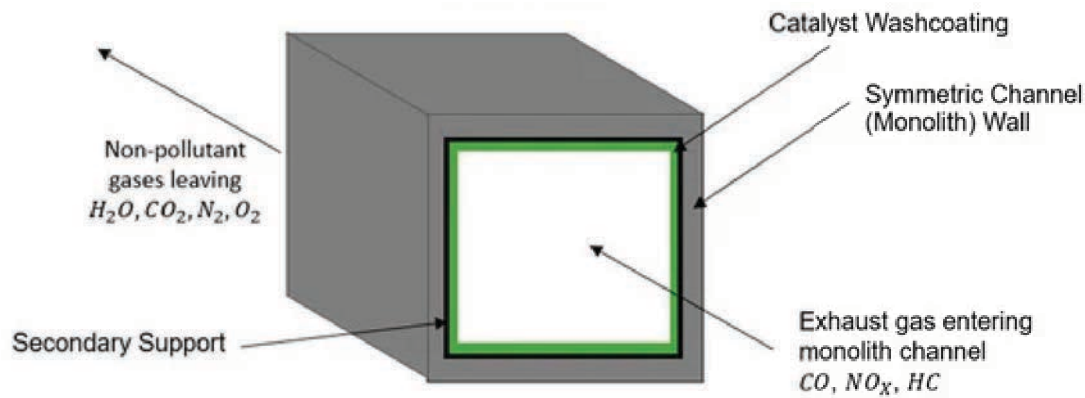
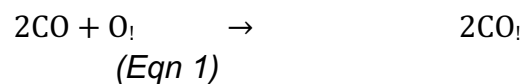


Figure 8: A labelled diagram of a singular monolithic channel in a catalytic converter.⁵³

The washcoat is a layer of material, usually a combination of alumina and silica, which creates a rigid surface/coating on the substrate, increasing the surface area for the gases to react. The catalyst would usually be added to the wash coat before being applied to the substrate. The catalyst itself is the active site responsible for the location where the chemical reaction will take place. This commonly contains precious metals such as platinum (Pt), palladium (Pd) and rhodium (Rh), depending on the reaction which is taking place.⁵⁴

The TWCC has two different jobs in reducing emissions. The first is oxidising CO and unburnt HCs to CO₂.⁵⁵



The second is to reduce the NO_x to N₂ and O₂.⁵⁶



An initial filter is also fitted, successfully filtering out around 99% of PM before entering the converter's substrate.⁵⁷ Although CCs effectively reduce emissions, they still need improvement. When considering the latest legislation on emissions, they are only somewhat effective at reducing the number of HCs released into the atmosphere, especially at low temperatures during start-up. Each component can be looked at individually for improvement to continue its development. The development of an oxidation catalyst receives the most attention of the individual components, shown by over 20x more results when searched using science direct (around 20,000 for CC compared to over 500,000 for oxidation catalyst). This is partly justified due to the higher number of uses for oxidation catalysts compared to substrates. They also have a more influential effect on activity than the substrate. However, this does not mean the substrate plays no part in the reactivity of a CC.

1.7. Monoliths

A monolith has recently been defined as 'A single block of material that contains various types of interconnected or separated channels.'⁵⁸ Benefits include stability, low thermal expansion, excellent flow-through properties, low-pressure drops, easily customised channel shapes/sizes and a sizeable geometrical surface area.^{59,60}

Monoliths have many uses in addition to catalytic converters. Examples include chemical and refining processes, water purification and ozone abatement in aircraft.^{59, 61} Monoliths traditionally have circular, triangular, hexagonal, or square channels and can broadly vary in wall thickness, cell density and specific size area.⁶² The geometry and size of the channels influence a monolith's mass and heat transfer properties and hence the catalytic performance.⁶³

Monoliths are traditionally manufactured using an extrusion method, where a ceramic paste is continuously forced through a grid producing consistent, unilateral channels extending in one direction. Although microchannels monoliths are possible to construct, with dimensions as small as 0.1 mm in wall width, the capabilities in design are relatively limited - mainly due to the simplicity of the manufacturing method.⁶⁴ There is also a limitation on the material appropriate for extrusion manufacturing, limiting the possibility of developing the material to enhance a monolith's catalytic benefit.⁶⁵

The diameter of each monolith channel is traditionally close to 1 mm. If the diameter is too small, too much back pressure is created from the flowing gas. If the diameter is too large, the reactant gases are less likely to react with the catalyst washcoat applied to the walls of the monolith. There is a balancing act between optimising the width of the monolith channels for maximum catalytic efficiency whilst not compromising the back pressure or mechanical strength of the system.⁶⁶

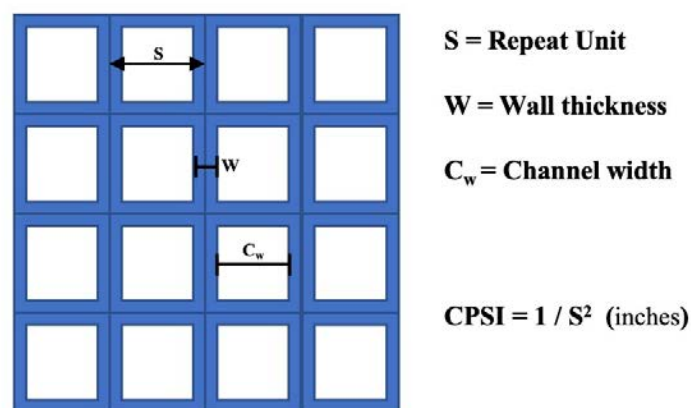


Figure 9: The relationship between a monolith and its structural parameters.

The most common monolith used for catalytic converter applications is a ceramic cylinder with 400 honeycomb or square-shaped channels per square inch (CPSI) and a wall thickness of around 0.165 mm.^{67, 68} The CPSI is a standard measurement

describing how many channels the gas can flow through. It represents the cell density of a monolith and is calculated using equation 7, where S is the width of a repeat unit measured in inches.⁶⁵

$$\text{CPSI} = \frac{1}{S} \quad \text{(Eqn 7)}$$

The frontal area is equal to the cross-sectional area from the direction in which the gas flow is applied. The open frontal area (OFA), which is effectively the void fraction of the monolith cross-section, is an essential factor to consider when trying to reduce back pressure and is calculated using equation 8 for a standard monolith, where W equals the wall thickness.⁶⁹

$$\text{OFA} = \text{CPSI} \times (S - W) \quad \text{(Eqn 8)}$$

In general, the transport phenomena of monolithic systems are highly complex. This is especially true for systems with high flow rates and varying gas input, such as a catalytic converter. The complexity increases even further when considering fluid dynamics and especially when turbulence is produced within the system. At a low flow rate, the flow is usually laminar, meaning the fluid dynamics is much simpler. However, the complexity intensifies once higher flow rates are present as turbulent flow is initiated. These factors are important to consider when designing a full-size or small-scale monolithic catalyst.

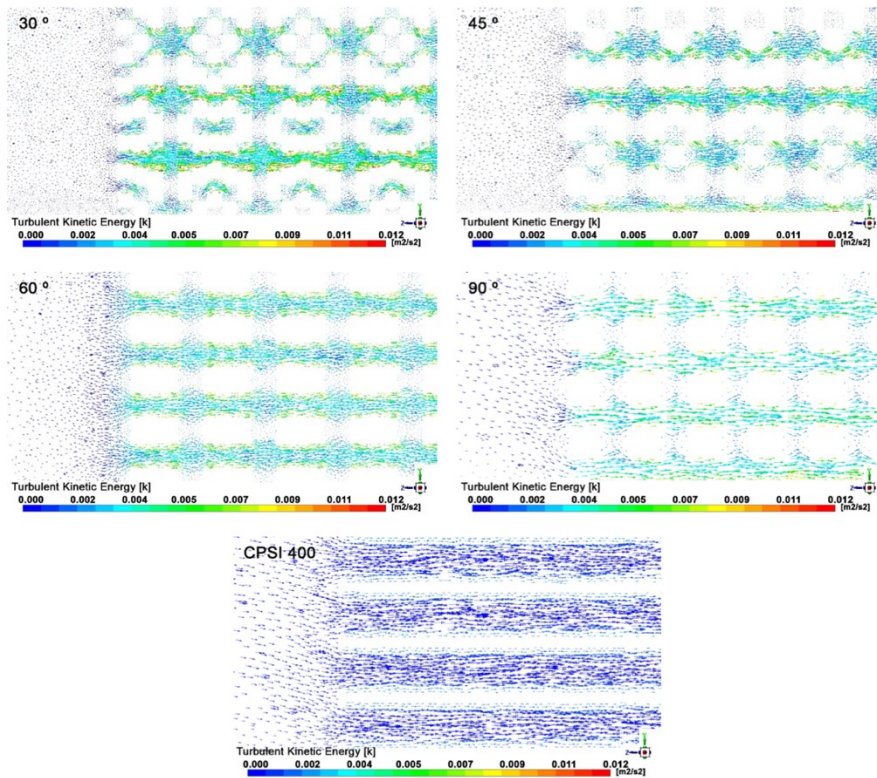


Figure 10: CFD images taken from a study by A. Doyle and S. Hajimirzaee investigating 3D printed substrates, showing the turbulent kinetic energy inside the channels.⁷⁰

After assessing the topic, it was concluded an interesting and unique way to pursue the problem of trying to improve a CC efficiency, would be to try and improve the monolith. This is where it was concluded the topic of 3D printing could have been an exciting and effective way to implement improvements to the CC substrate.

Additive manufacturing (AM) technologies have a unique advantage in addressing these issues simultaneously. Also known as 3D printing (3DP), it has recently attracted much attention as a low-cost technology for rapid manufacturing and prototyping using various materials, including ceramics.⁷¹ It differs fundamentally from traditional subtractive manufacturing methods, allowing unprecedented freedom and 'bottom-up' construction with high levels of precision and control. The technology can produce complex three-dimensional designs whilst also manipulating

the properties of a surface – such as increasing the surface roughness of a monolith, for example.⁷²

A benefit to 3D printed substrates is the ability to increase a design's internal complexity and cross-sectional pattern compared to a traditionally manufactured monolith. Improvements in the internal surface area and the number of exposed faces can be introduced whilst maintaining a consistent open frontal area. Designs can be tailored to optimise the internal structure whilst staying within the limits of any practical use. Introducing a larger surface area is beneficial as reactant gases are more likely to react with the catalyst.⁷³ Introducing more exposed faces can also encourage greater internal turbulence within the monolith, improving mass transfer as more collisions with the monolith walls can occur.⁷⁴ This can all lead to better catalytic activity when using a 3D printed monolith.

Surprisingly, the AM of monoliths is still in a very early exploratory stage, with very few cases of industrial use recorded. There are several cases of printed monoliths being applied to catalytic applications, but the process's complexity means relatively few have yet to be implemented outside scientific research. Of all the additive manufacturing techniques, Robocasting (or Liquid Deposition Modelling, LDM) and Digital Light Processing (DLP) are two of the most trialled in scientific literature to produce monolithic catalysts, with each investigated as part of this thesis.

1.8. 3D Printing Process

3DP usually begins with constructing a digital model using computer-aided design (CAD) software such as Autodesk Fusion 360. This design would then be transferred to a slicing program where the design is cut into layers, which the printer will

eventually build up to construct the final design. The same software will then translate this code into a format the printer reads, informing the printer of how to construct the model.⁷⁵

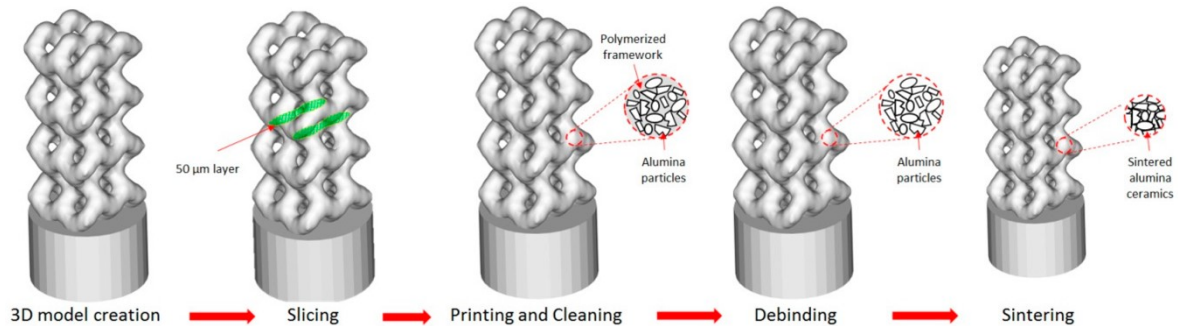


Figure 11: Steps of the 3D printing process.⁷⁶

1.8.1. Robocast Printing

Robocasting, analogous to LDM or direct ink writing, is one of the most common and easy-to-use AM techniques for ceramic applications. A typical setup would consist of clay-like material being extruded under pressure through a nozzle. The software then controls the pattern and position of the nozzle. The clay is a colloidal suspension printed in a semi-solid state, causing the material to quickly dry once extruded. The rheological properties of the print material are the most influential in this process and have the most significant effect on the printable success. Organic binders and plasticisers are usually added to alter the material's consistency. The benefit of this process is that almost any powder can form a clay-like printing material, assuming the rheological properties are correct.⁷⁷

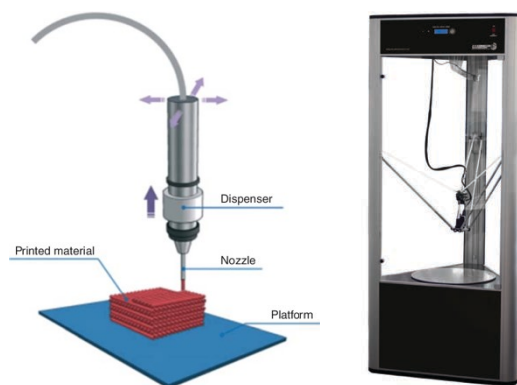


Figure 12: (Left) Schematic of Robocast 3D printer.(Right) A Delta WASP 4070 3D printer.^{78,79}

1.8.2. Robocast Substrates

Robocast was the first 3D printing technique attempted in this thesis as a proof of concept for 3D printed substrates. This is primarily due to its simplicity and cheaper start-up cost than other techniques, such as digital light processing.⁸⁰ For the application of catalytic converters, the 3D printed substrates need to be able to have a wash coat applied whilst withstanding temperatures up to 1000 °C attained in the exhaust system.⁸¹ This means the monolith is usually made from a ceramic material due to its excellent thermal stability, low thermal expansion coefficient and the ability for a catalyst to stick to its walls.⁶⁵ In literature, several studies have successfully used robocast to produce a ceramic monolith coated in a catalyst for gaseous catalytic studies.

1.8.3. Digital Light Processing

DLP is a slightly more complex printing process when compared to robocasting. The principles of DLP are based on a vat of photosensitive resin loaded with solid ceramic particles, which solidifies when exposed to light. The printing bed initially

lowers into the vat before an LCD screen projects the required layer pattern onto the resin, causing it to cure in the set pattern onto the printing bed. The printing bed will then rise out of the resin, allowing the resin to self-level before lowering back into the resin. The LCD screen will then project the next layer onto the resin, which will cure onto the previous layer and so on, eventually building up the model. Once the model is complete, the final part is a polymer-ceramic composite which then requires a post-heat treatment to remove the polymer and leave the final ceramic part. DLP allows for much more complex designs when compared to a robocast printer. This is mainly due to the ability to achieve much finer printing detail and produce overhangs in the design, as the model is self-supporting when being constructed due to the instant solidification.^{82, 83}

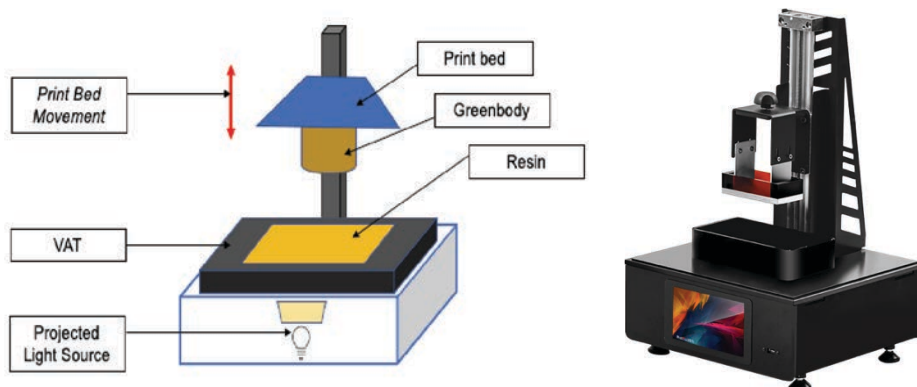


Figure 13: (Left) A schematic of the Digital Light Processing 3D printer. (Right) A Photocentric Liquid Crystal Precision 1.5 DLP 3D printer.⁸⁴

1.8.4. Ceramic Resins

A ceramic resin usually consists of monomers and/or oligomers, solid ceramic particles (known as the filler) and a photoinitiator.⁸⁵ Additional additives can be included to alter the properties of the resin. As the resin cures, the monomers bond to create a solid polymer structure around the ceramic filler and this solid model is called the 'green body'. A green body is usually stronger than a pure polymeric

part.⁸⁶ In resins, there are two more common monomers used, each undergoing slightly different chemical reactions with different photoinitiators.

The first type of monomer is epoxides, and the second is acrylates. Both will produce a green body with slightly different properties, ultimately influencing how the green body is post-treated. Epoxides require a cationic photoinitiator and undergo a reaggregating chain reaction when a Lewis or Bronsted acid (produced by the photolysis of the initiator) attacks an intra-molecular bond.⁸⁷ They are less commonly used for ceramic resins in digital light processing due to their higher costs and longer cure times.⁸⁸

Acrylate resins rely on a free radical polymerisation reaction where a radical is formed when the initiator is exposed to light.⁸⁹ A common initiator is Phenylbis (2,4,6-trimethylbenzoyl)-phosphine oxide (BAPO). Upon exposure to light, a free radical is created, which attacks the double bond of the acrylate via the α -cleavage mechanism. The unpaired carbon then reacts with other carbons creating a longchained molecule which transforms into a solid state.⁹⁰ An example is displayed in Figure 14.

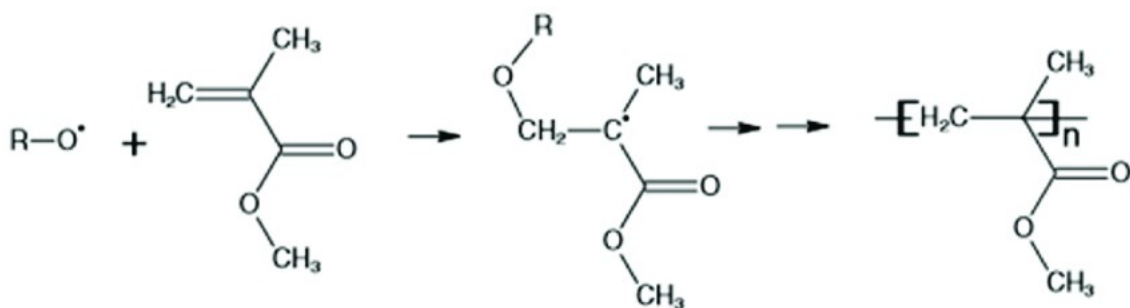


Figure 14: Radical cleavage mechanism.⁹¹

One of the resins' main properties affected by the photoinitiator is the cure depth

(C_d). C_d refers to the depth at which the resin reaches its gel point when exposed to light. The higher the concentration of photoinitiator in the resin, the deeper the resin can usually cure. However, there is a maximum (C_{dmax}) that, when surpassed, prevents the resin from curing any deeper and can hinder the curing depth.⁹² This is because if the concentration is too high, the resin closest to the light cures so quickly that it solidifies and obstructs the photons from travelling any deeper into the resin.⁹³ Additionally, once the initiator concentration passes the optimal, the collision probability of free radicals increases, meaning they are less likely to participate in the polymerisation process, resulting in self-annihilation.⁹⁴ This means an optimal intermediate is required. Ultimately, cure depth (C_d) is a result of the sensitivity of the resin and the energy dose applied (E_0). The relationship between these parameters is set out by Jacobs in the highly noteworthy publication 'Fundamentals of Stereolithography'.⁹⁵ The working curve equation is listed below:

$$C_d = D_p \times \ln \left(\frac{E_0}{E_c} \right) \quad (Eqn 9)$$

A semilog plot of C_d vs $\ln(E_0)$ produces a straight-line graph. The Y-intercept equals E_c (the critical energy dose required to initiate polymerisation) and the gradient equals D_p (the depth of penetration), which is a measurement of the specific resin's sensitivity to a change in light exposure. Equipped with D_p and E_c , the light exposure and z-axis increments can be adjusted in the printing software by the user to optimise the printing process.

The number of solid particles within the resin also affects C_d .^{96, 97} The addition of a solid filler ultimately has numerous effects on the resin. Some of these effects are a result of light scattering, where the solid particles suspended within the resin become

the scattering centre of the incident light.⁹⁸ This can result in a reduced cure depth along with over-curing or unrefined edges.⁹⁹ A raw resin alone is considered a clear, uniform medium where the light attenuation is affected only by absorption owing to the photoinitiator, which leads to the bonding of the monomers. Once a solid filler is added, the resin becomes more complex as the light undergoes a scattering effect as it encounters the solid particles.¹⁰⁰ Some of the light can be deviated from the forward direction causing it to refract into the resin.¹⁰¹ As a result, the resin can be cured outside of the initial direction the light was travelling and potentially outside of the printing design. Figure 15 helps to explain this.

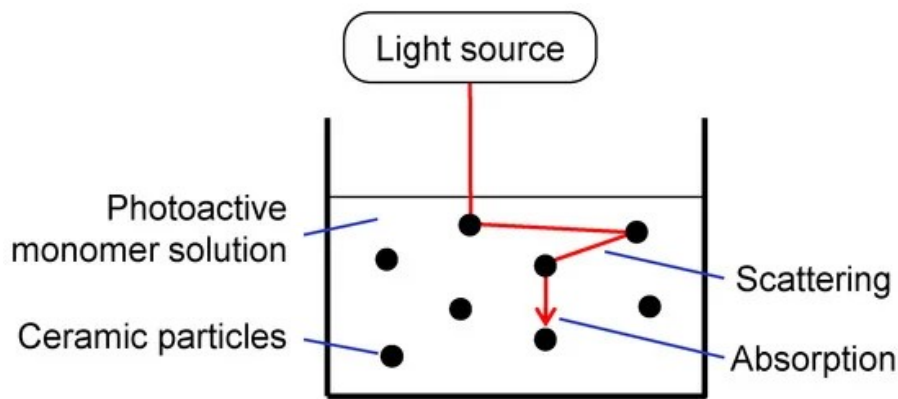


Figure 15: A schematic showing the light scattering phenomena which can occur within a ceramic resin.¹⁰²

Several variables related to solid particles can influence the scattering effect. This includes the particle size, the number of solid particles and the refractive index of the solid particles themselves. The smaller the particle size, the higher the number of interfaces available to transmit light, meaning more scattering occurs.¹⁰³ The more particles in the resin, the more opportunity for the light to encounter particles which results in more scattering. However, not enough solid particles and the final product will become too void after the polymer network has been burnout, resulting in a structure unable to support itself after sintering.¹⁰⁴ Furthermore, when the refractive index (RI) contrast between the resin and the ceramic particles is increased, the

scattering effect is greater.¹⁰⁵ As RI increases, the angle at which the light is deflected increases. This results in a larger scattering effect, reducing C_d whilst negatively influencing the cure width and finish of the final product. Therefore, the closer the refractive index of the ceramic filler and the resin, the easier the control over the photopolymerization process.¹⁰⁶

An additional but very important property to remember throughout this process is how changing any of the above variables affects the viscosity of the resin. Low viscosity is required, generally accepted within the region of 2-5 Pa.s, to ensure the resin is capable of self-levelling once the print bed raises.^{107, 108} By decreasing the particle size and increasing the solid loading, the viscosity of the resin increases so a middle ground is required where there is enough solid filler to ensure a solid final product, generally accepted at above 45 %, whilst trying to keep viscosity below 5 Pa.s.¹⁰⁹

At the time of starting this project, no suitable commercial resin could be sourced so the decision was made to try and synthesise an appropriate resin internally. In general, a photocurable resin should satisfy the requirements of a high solid loading, low viscosity, and adequate cure depth (C_d) for printing purposes.

1.9. Aims and Outlook

The ultimate aim of this project is to reduce the methane emissions emitted from the G-volution dual-fuel engine system exhaust stream. To achieve this, it was concluded that trying to improve the substrate could be a promising technique to improve the catalytic performance of a CC. Utilising 3DP creates an exclusive opportunity to manufacture complex ceramic structures, which could enhance the mass transfer of reactants and result in an upgraded catalytic performance. Firstly,

unique designs must be produced which exploit the benefits of 3DP. Secondly, a suitable material must then be manufactured which can produce ceramic substrates with extremely fine detail. Thirdly, an active catalyst must then be synthesised to be used as a washcoat for the substrates. Catalytic activity testing will then be conducted on the samples, and comparisons will be made regarding their catalytic activity.

2. Literature Review

Chapter 2 consists of a literature review around the topics discussed in the introduction. This begins with catalysts used for methane oxidation in the context of vehicle emissions. The reaction mechanism is discussed along with the role specific catalysts play in this mechanism. 3D printed monoliths are then discussed using both robocasting and digital light processing manufacturing methods. Finally, 3D printed monoliths utilised for catalytic testing are discussed including any conclusions made regarding their effect on catalytic activity.

2.1. Methane Catalysts

Noble metal catalysts (Pd, Pt and Rh) are very active catalysts for the complete oxidation of methane. Among the noble metals, palladium is usually chosen due to its superior activity.¹¹⁰ A high level of dispersion can be obtained when deposited on conventional metal oxide supports, which means a higher number of exposed active sites and generally a more active catalyst. Pt can also be added as it encourages the stability of the Pd particles on the catalyst support.^{111,112} However, numerous factors influence the activity of the catalyst, such as the precursor, the support material, the

metal loading technique, the calcination temperature, the morphology of the Pd/Pt and the catalyst pre-treatment process making the direct comparison of catalysts difficult.

In the presence of O₂ (which is the case for catalytic converters), Pt and Pd oxidise to PtO₂ and PdO, respectively. PdO forms at around 300-400 °C and is stable up to about 650-850 °C depending on the reactive conditions.¹¹³ PtO₂ is much less stable and decomposes at around 350 °C. This means Pt is usually in metallic form during catalytic methane oxidation, typically within the temperature range of 400-650 °C.¹¹⁴ The nature of active Pd/Pt catalysts for the complete oxidation of methane has been a matter of debate for a long time. The metallic Pd, Pt, Pd/Pt pairs and PdO all show catalytic activity with different active phases and specific activities. Still, it is broadly accepted that the most active compound is PdO.^{115, 116} Further complexity comes from the fact that small changes in the support used, the impregnation technique undertaken, and the calcination conditions can affect the precious metals states.^{117,118} This is not to discard the reactivity of the metallic Pd or Pt, but these are not considered as reactive as PdO.

2.1.1. Reaction Mechanism

The reaction mechanism for methane oxidation over palladium oxide has been extensively debated. There is a general agreement that the rate of reaction is first order with respect to methane and near zero order with respect to oxygen. The rate-limiting step for the reaction is the dissociative adsorption of methane via H abstraction over the PdO site.^{119,120}

Although no unanimous mechanism is concluded, many authors have suggested the reaction mechanism over PdO to be an MVK mechanism.^{121,122,123} ER and LH mechanisms have been suggested, which both differ from the MVK mechanism in

that the adsorbing surface does not partake in the reaction.¹²⁴ Isotopic labelling experiments have been conducted in literature, supporting the MVK method more so than the ER or LH mechanisms.^{125,126,127} The complexity of the reaction and the strong dependency on the reaction conditions results in these three mechanisms having been extensively debated. However, the MVK is more widely accepted and is supported by many experimental results on catalytic methane combustion.^{128,129}

For a basic MVK mechanism, the methane is first adsorbed onto the PdO surface. A methoxy $\text{CH}_3\text{O}_{\text{ads}}$ species and an OH_{ads} species are formed, which then transforms into an intermediary $\text{CH}_2\text{O}_{\text{ads}}$ species before O_2 is adsorbed from the gaseous oxygen in the reactant stream. A rearrangement occurs at the surface creating a $\text{H}_2\text{O}_{\text{ads}}$ species via hydrogen transfer before H_2O is desorbed, leaving an oxygen vacancy behind. This oxygen vacancy is then filled via the lattice diffusion of oxygen. The remaining OH_{ads} species receives a second hydrogen from the CHO_{ads} before H_2O desorbs leaving a CO_{ads} to bond to a second oxygen atom, forming $\text{CO}_{2\text{ads}}$. The CO_2 then desorbs before the oxygen void is filled via gaseous oxygen and the cycle continues.¹³⁰

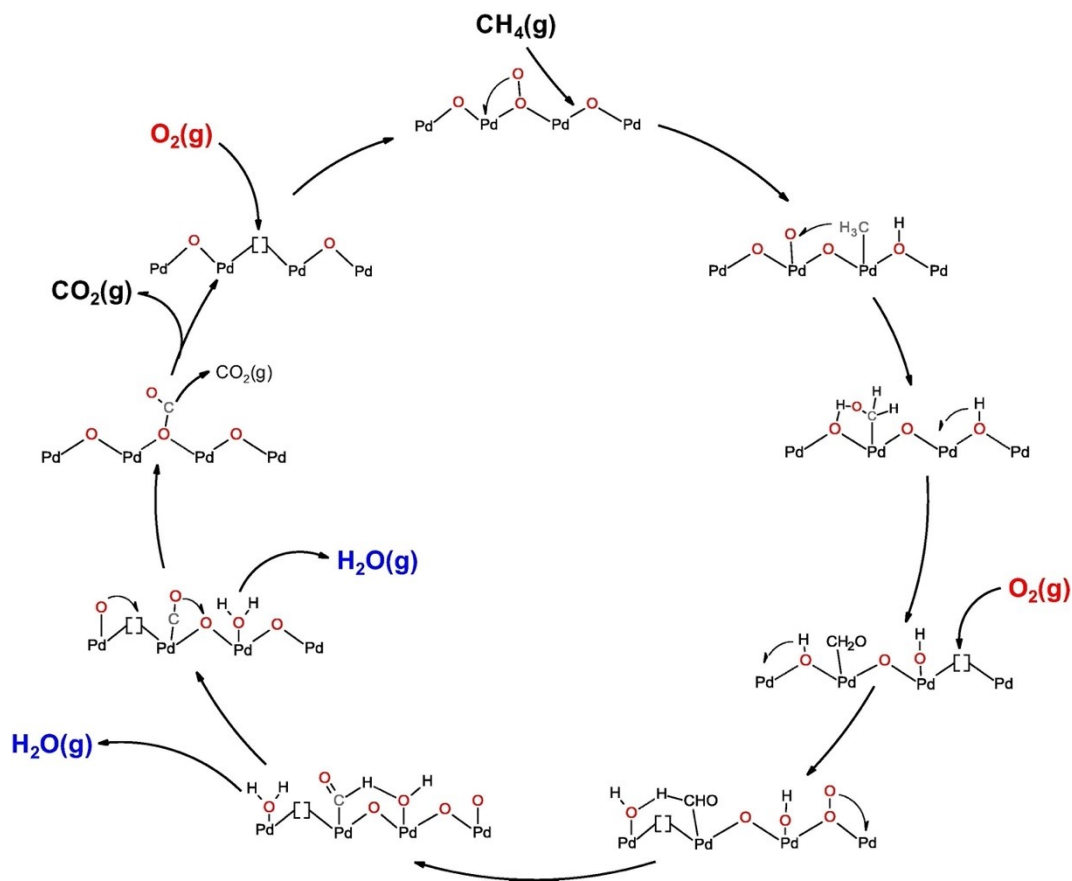


Figure 16: Proposed MVK mechanism for the complete oxidation of methane over a PdO surface.¹²⁹

To make matters more complicated, this mechanism does not consider the numerous products produced as part of the LNG reaction, including compounds such as NO_x , H_2O , and sulphur compounds.¹³¹ The variation in conclusions about the mechanism suggests how complicated the behaviour of the system is. Therefore, we can assume the catalyst activity depends on not only the catalyst but the reaction conditions. Thus, although methane is the simplest hydrocarbon, the exact mechanism of its oxidation over noble metal surfaces has not been clearly identified, even though there are numerous results regarding the activity of specific catalysts for the complete oxidation of methane.

2.1.2. Pd/Pt on Zeolite

The catalyst used in this study consisted of Pd and Pt loaded on a zeolite support material. Zeolite was chosen due to its large surface area compared to established metal oxides conventionally used as catalyst supports, such as Al_2O_3 , TiO_2 , CeO_2 and ZrO_2 .¹³² The first reported case of Pd on zeolite can be dated as far back as 1969, with the first direct comparison to Pd/ Al_2O_3 conducted by Li and Armor in 1994.^{133,134} Three zeolite framework structures (FER, MOR, MFI) were assessed under the complete oxidation of methane. All three exhibited a lower light-off temperature than the Pd/ Al_2O_3 reference by around 70-80 °C. Over time, several zeolite frameworks have been evaluated, exhibiting improved catalytic activity.^{135,136,137,138,139}

The nature of the specific zeolite framework doesn't seem to significantly affect activity. Any attempts to directly link the properties of the zeolite and methane oxidation activity have displayed no coherent results. Analysis based on the variation of the dimensionality and pore size showed no consistent relationship with mixed reports.^{140,141,142} The most influential zeolite property affecting activity is reported as being the Si/Al ratio. As the ratio gets closer to one, the number of acidic sites available increases.¹⁴³ Friburg et al. studied the effect of the zeolite Si/Al ratio during methane oxidation and concluded that more acidic sites resulted in increased dispersion of the PdO particles.¹³⁷ These H^+ acidic sites bond with the O atom in the PdO species meaning more acidic sites result in more stable PdO particles and less sintering.^{144,145, 146} Considering acidic sites are required for PdO anchorage and improved stability, this could explain why a low Si/Al ratio improves a catalysts performance.

The addition of Pt has been reported in numerous studies to have beneficial effects on the stability and activity of a Pd catalyst. Ratios ranging from 1:1, 2:1 and 1:2 of Pd:Pt have been investigated by G.Lapisardi et al. with the most effective reported as 2:1 Pd:Pt which displayed 50 % methane conversion approximately 30 °C lower than the Pd catalyst alone.¹⁴⁷

However, this research aims not to compare the activity and conditions of specific catalysts, but to synthesise a stable, active catalyst for the complete oxidation of methane. Two different zeolites were utilised as a support material for a Pd/Pt catalyst, and an approximate 2:1 ratio of Pd:Pt was selected. A sodalite zeolite was synthesised in-house using a geothermal waste fluid which followed a previous study by A.Doyle and L. Tosheva.¹⁴⁸ A commercial zeolite Y catalyst was also used as a support which underwent the same precious metal loading. Zeolites were selected for the catalyst due to a large surface area to mass ratio compared to many other materials. Both catalysts were tested for the complete oxidation of methane, with the results detailed below.

2.2. 3D printed monoliths

There have been several CAD designs produced in literature for 3D printed catalyst supports with varying complexity regarding internal structure. One of the stand-out studies was produced by Alketan et al who designed and printed multiple ceramic structures before reviewing their mechanical stability.¹⁴⁹ Fifteen designs were produced based on three categories: foams, strut-based lattices, and triply periodic minimal surfaces. Unit cells were constructed and repeated with a constant sheet/strut thickness of 0.6 mm resulting in designs varying in macroporosity (71 – 90 %) and specific surface area (420 – 1753 mm²/mm³), both important factors for catalytic substrate reactivity. Although no direct catalytic properties were investigated

experimentally, this does not detract from the high quality of the designs produced or the success achieved in manufacturing these designs into ceramic catalyst supports.

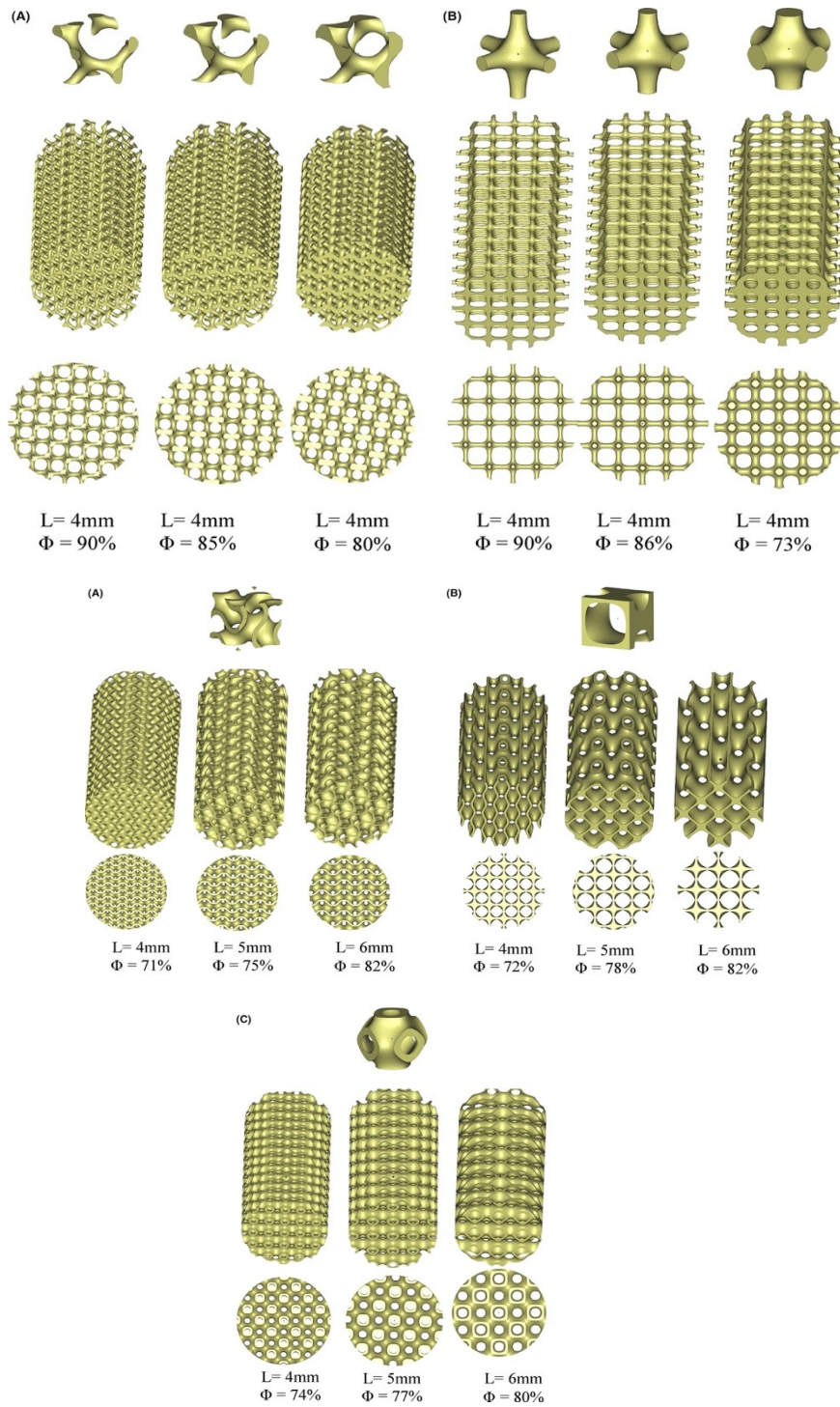


Figure 17: CAD designs produced by Alketan et al. ¹⁴⁹

Another interesting study based on TPMS designs was conducted by J. Manzano, H. Wang and I. Slowing, where seven TPMS structures were printed using an acrylate resin.¹⁵⁰ The 8x8x8 mm cubic structures were designed using 3DTool CAD software and printed using an SLA printer. Metal salts were dissolved into the acrylic acidbased resin creating metal-polymer composite structures. A benzyl alcohol oxidation reaction was then performed to analyse the architectures' reactivity. The result demonstrated the ability to employ 3D printing, whilst optimising surface topology, into an active three-dimensional catalyst which resulted in improved chemical conversion as the surface area increased.

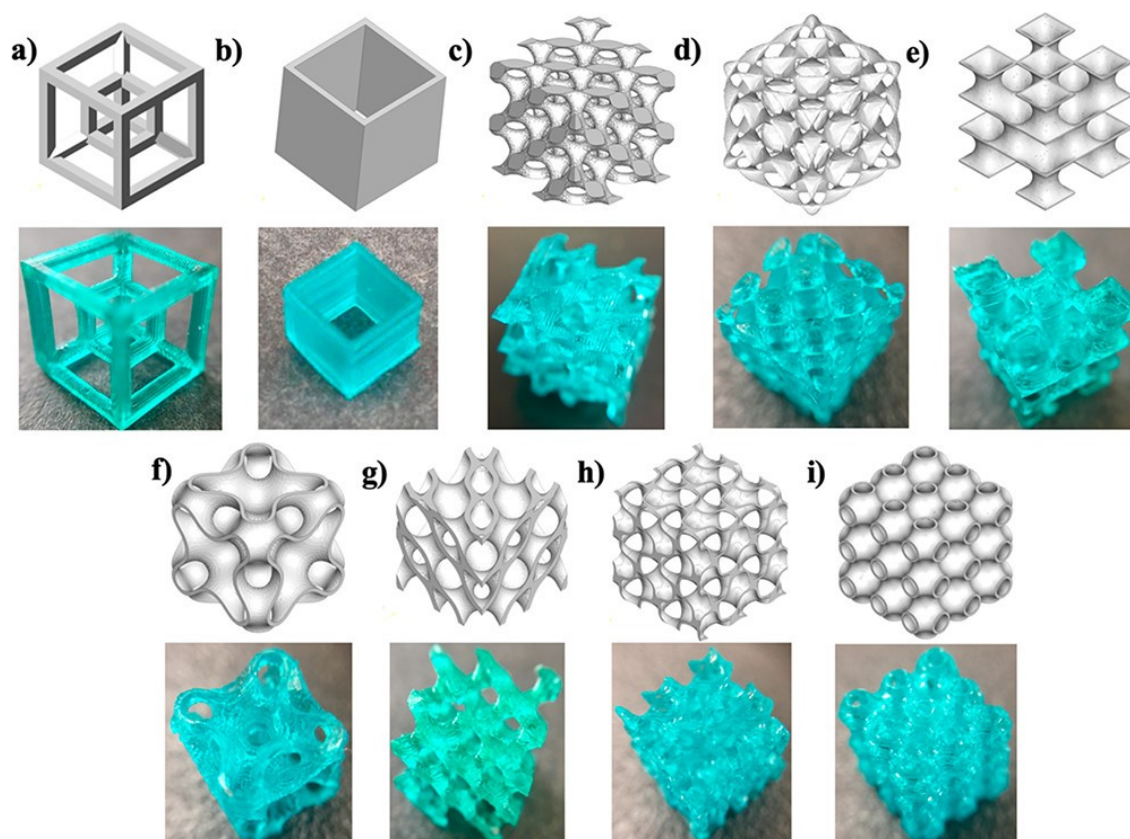
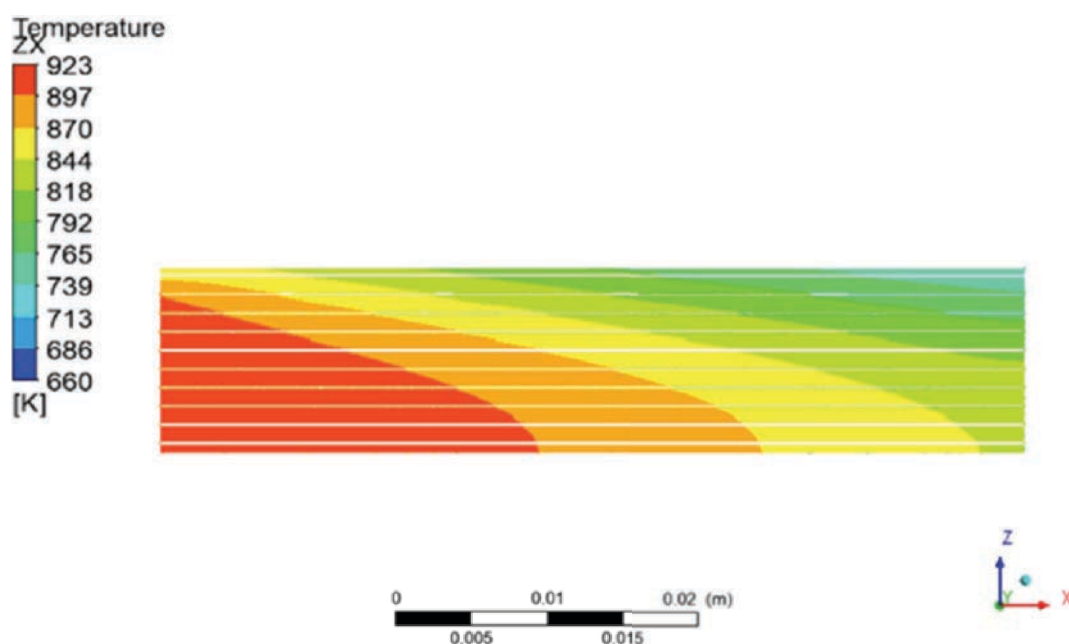


Figure 18: Resin substrates produced by J. Manzano et al. and their CAD designs.¹⁵⁰

Another prominent researcher in this field is Nikolina Kovacev. Kovacev has produced a handful of publications on the topic of 3D printed catalyst support structures since 2021. His first, in January 2021, investigated the effect of the

internal structure on thermal and hydraulic properties using numerical modelling and some experimental testing.¹⁵¹ A diamond lattice structure was printed inside a cylinder ($\text{\O}25.4 \text{ mm} \times \text{H}61.3 \text{ mm}$) with a strut diameter of 0.65mm, an open frontal area of 0.73 and a surface area of $1480 \text{ mm}^2/\text{mm}^3$. The substrate was subject to CFD analysis with the results displayed in Figure 19. Here, a simulation is run which theoretically measures the internal temperature achieved within the substrate. The input conditions are the same so a conclusion is made, that any variation in internal temperature is due to changes in the internal behaviour fo the gas flow.

Kovacev revealed that the diamond lattice structure displayed an improved core temperature distribution when compared to a conventional honeycomb monolith, indicating that the lattice structure could improve thermal performance in an exhaust system, most likely induced by turbulence. Not only did Kovacev prove DLP could be used to successfully print a self-supporting diamond lattice structure, but the benefits of DLP printing mean this structure could be tailored in the future to optimise the relationship between thermal management, back pressure, and catalytic performance.



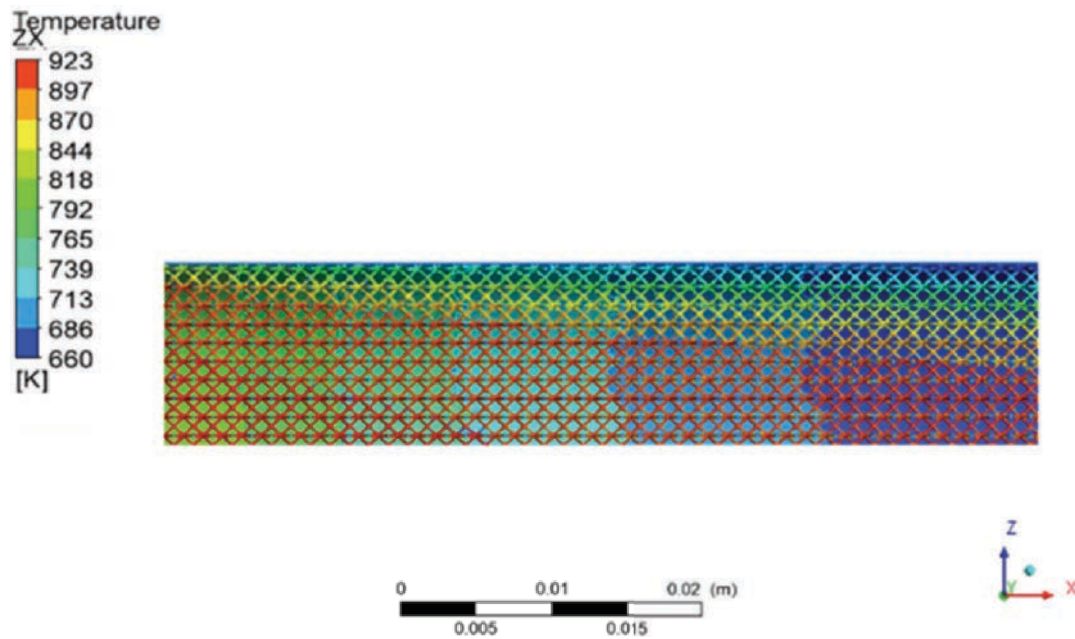


Figure 19: Temperature contour of a honeycomb 400 CPSI monolith (Top) and a 3D printed diamond lattice substrate (Bottom).¹⁵¹

A second paper published by Kovacev in May 2022 involved the design of three more complex dual substrate models using Ansys SpaceClaim CAD software.¹⁵² The internal structures were based on a diamond lattice previously researched, but the three new designs featured interlocking mechanisms involving an inner core and an outer shell. By introducing two parts, each could be subject to separate washcoats, which can be beneficial for catalytic systems requiring oxidative and reductive reactions or those needed in a restricted space where space saving is extremely beneficial, such as exhaust treatment systems.

2.3. Robocast Review

Van Noyen et al. manufactured titanium ceramic alloy cuboids (42 mm x 42 mm x 50 mm) with two different stacking techniques – a stacked woodstock pile design and a continuous offset woodstock pile design, as shown in Figure 20 below.¹⁵³ The fibres had a diameter of 650 μm with spatial distances ranging from 450 – 1100 μm . A mordenite zeolite was then grown onto the surface of the substrates. The substrates were tested for the oxidation of nitrous oxide (N_2O) using 10 vol.% N_2O made up with helium at a gas hourly space velocity of 10000 mL $\text{N}_2\text{O}/\text{mL}_{\text{catalyst}}/\text{h}$ in the temperature range of 200 $^{\circ}\text{C}$ to 800 $^{\circ}\text{C}$. Although there was no comparison to a powder catalyst or commercial monolith, the substrates showed effective conversion of N_2O , which is a major component of exhaust emissions, achieving 100 % at 800 $^{\circ}\text{C}$.

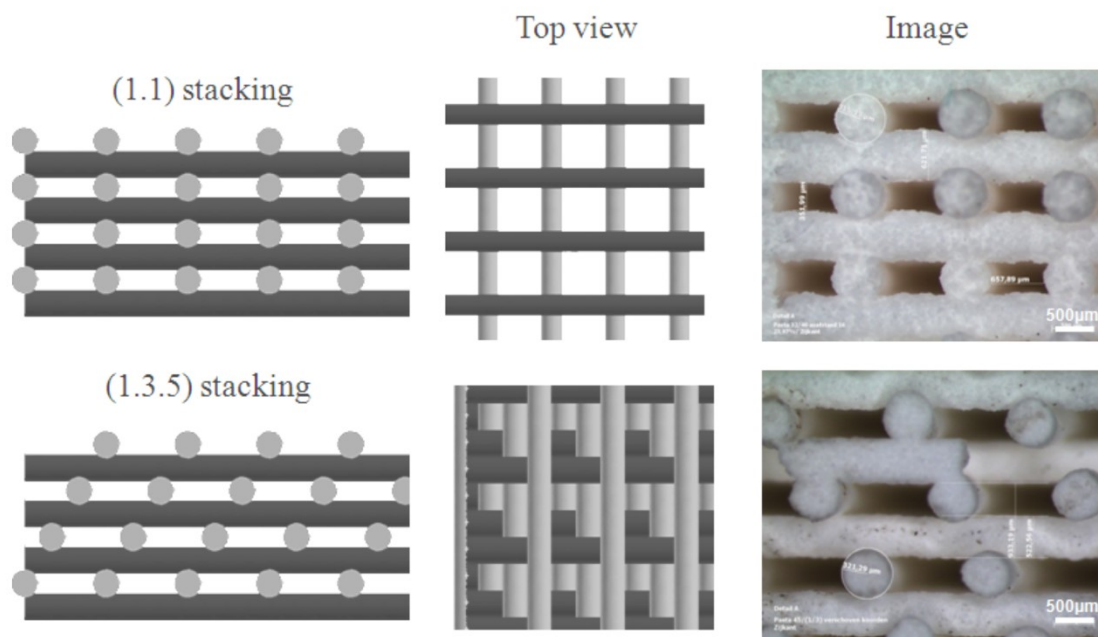


Figure 20: The two titanium ceramic alloy cube designs produced by Van Noyen et al.¹⁵³

Stuecker et al. at the Advanced Materials Laboratory in New Mexico, USA, manufactured a barium manganese hexaluminate ($\text{BaMn}_2\text{Al}_{10}\text{O}_{19}$) robocast monolith and a high-purity alumina robocast monolith (12.7 mm x 22.0 mm) using a

slightly different offset wood stockpile design compared to Figure 20, with the fibres offset in every other layer which also inhibited any direct line of sight through the monolith as shown in Figure 21.¹⁵⁴ The fibres had a diameter ranging from 725 μm to 1000 μm with a fibre spacing of 500 μm . A barium manganese hexaluminate catalyst was then applied via a washcoat using an aqueous slurry dip-coating technique. The monoliths were tested for the complete oxidation of methane in the temperature range of 400 $^{\circ}\text{C}$ to 800 $^{\circ}\text{C}$ under a gas flow consisting of 10 % oxygen, 2.5 % methane and 87.5 % nitrogen at a flow rate of 205 mL/min. With all the substrates wash coated with the same catalyst loading, the results exhibited improved conversion for the robocast substrates at all temperatures above 450 $^{\circ}\text{C}$ compared to the commercial 400 CPSI counterpart, including an approximate 6-fold improvement in conversion at around 600 $^{\circ}\text{C}$.

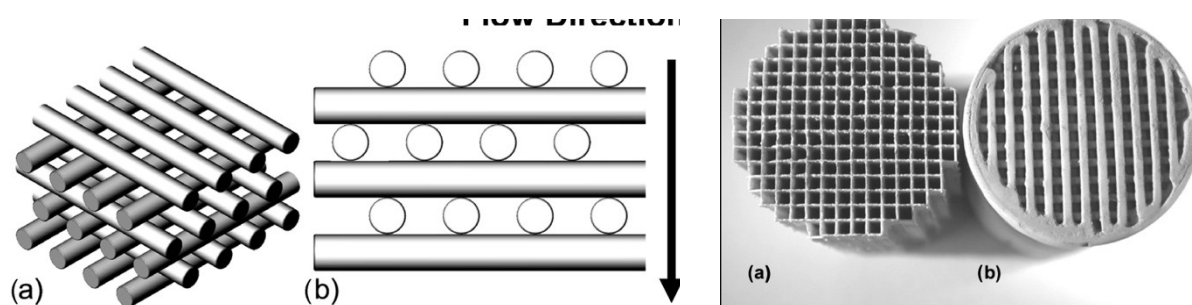


Figure 21: The design produced by Stuecker et al., including the final ceramic substrate and the commercial substrate used for comparison.¹⁵⁴

More recently, C. Leclerc and R. Gudgila achieved a 3D printed cylindrical monolith (170 mm x 100 mm) from ceria.¹⁵⁵ The monoliths were produced externally by Robocasting Enterprises LLC using the offset woodstock pile design from Figure 21. The fibres had a reported diameter of 1110 μm with a fibre spacing of 1790 μm , slightly larger than the design produced by Stuecker et al. Three substrates with

different compositions were produced, including pure ceria, pure alumina and a 50/50 ceria-alumina monolith. A rhodium catalyst was then washcoat onto the substrate by saturating the supports in a 14 % rhodium nitrate solution before calcining at 600 °C. The substrates were subject to methane and carbon monoxide oxidation catalytic testing. Although no comparison was made with a commercial monolith or powder catalyst, all the 3D printed substrates successfully oxidised both methane and carbon monoxide.



Figure 22: An image of the 3D printed cylindrical monolith taken from the publication by C. Leclerc and R. Gudgila referred to above.¹⁵⁵

Most relevant to the catalytic testing conducted later in this thesis, A. Doyle and S.Hajimirzaee produced substrates with a fibre variation in the X angle using the robocast printing techniques.⁷⁰ Four offset angles were produced (30°,45°,60°,90°), shown in Figure 23, using a cordierite precursor paste which were then washcoated with a Pd/Pt zeolite catalyst. Methane oxidation studies were conducted where the offset X-angle designs all showed enhanced catalytic performance when compared to a 400 CPSI commercial monolith washcoated in the same catalyst. CFD software was utilised to prove the theory of enhanced turbulence within the 3D printed channel systems. For specific designs, it was reported that there was nearly five times the amount of kinetic energy produced within the 3D channel structures

relative to the 1-dimensional 400 CPSI. It was concluded that the enhanced turbulence was at least partially responsible for the improved conversion of methane.

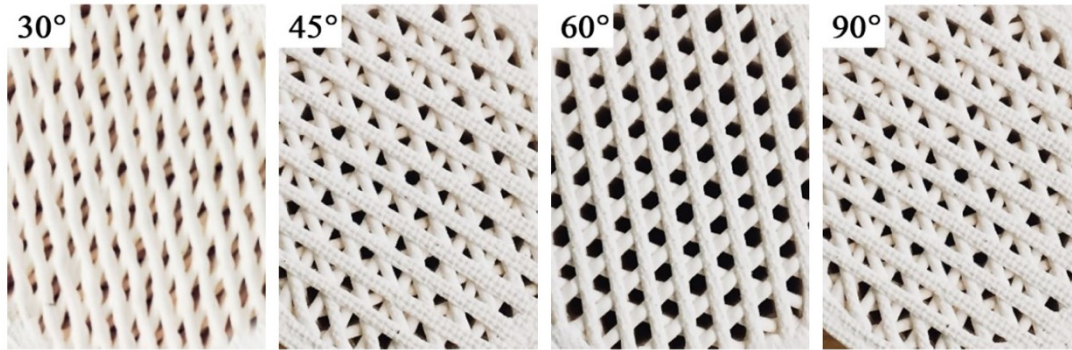


Figure 23: Images taken from a publication by A. Doyle and S. Hajimirzaee showing four designs printed using robocast technology.⁷⁰

The same authors then took this one step further in a second study by printing a full-sized ($\text{Ø}320 \text{ mm} \times \text{H}120 \text{ mm}$) 90° substrate and testing the catalytic activity in the after-treatment system of an industrial heavy-duty diesel engine.¹⁵⁶ The industrial conditions proved the induced turbulence increased conversion at moderate and high temperatures where the reaction rate was governed more greatly by internal and external mass transfer. It also proved that although the back pressure of the 3D printed substrate was larger than the commercial, 3D printing is still a viable method to prepare catalytic converter substrates.



Figure 24: A commercial size 3D printed catalytic converter, tested under industrial conditions, taken from a publication by A. Doyle et al.¹⁵⁶

2.4. Ceramic Resin Literature Review

For ceramic stereolithography (CSL), it is largely accepted that a general formulation is not consistently possible with different ceramic powders or monomers. Therefore, it is recommended that for each circumstance, a specific formulation should be investigated. There has been a selection of cases in the literature where photosensitive ceramic resins have successfully been produced.

The first published example was pioneered by Griffith and Halloran in 1994, who fashioned the field of ceramic stereolithography (CSL). This was the first proof of concept where a ceramic filler was added to a photosensitive resin to build a 3D ceramic greenbody.¹⁵⁷ Silica and alumina were each added to a UV-curable acrylamide solution with solid loading in the range of 45 – 55 vol.%. A mercury UV lamp was employed to prove the possibility of curing the resin, with conclusions made that the UV curing of highly loaded ceramic suspensions was achievable. They also concluded that the difference in the RI between the resin medium and the ceramic filler should be kept to a minimum for accurate curing. Two years later, the same authors managed to produce freeform ceramic bodies in the shape of a cylinder using these resins via stereolithography.¹⁵⁸ Since then, the field has progressed to include different resins with various ceramic powders, and more so in recent years as technology has developed.

Successful resins synthesised have included ceramic powders such as Al_2O_3 , ZrO_2 , SiO_2 , SiC and BaTiO_3 with particle sizes ranging from 0.05 microns to 12 microns and successful solid loadings in the range of 40-60 vol.%.^{105, 159-165} A solid loading below 40 vol.% seems to cause the greenbody to excessively shrink and delaminate during the burnout and sintering phase meaning very few successful cases have been published. Typically, 50 vol.% of ceramic powder has been accepted as

sufficient to ensure a dense final ceramic product, but anything above this is desired to enhance the mechanical properties of the final ceramic.¹⁶⁶ Nevertheless, increasing the solid loading and decreasing the particle size increases viscosity, so it is common for the upper limit of viscosity to dictate the final solid loading. Although particles in the nanometres has been achieved, the higher surface energy can cause agglomeration issues in addition to increasing viscosity.¹⁶⁷ Although a smaller particle size reduces the final sintering temperature required, they also hinder C_d as more scattering occurs. The largest scattering problem seems to occur when the particle size approaches the wavelength of the light.¹⁶⁸ Particle sizes up to 12 microns have been proven sufficient to produce a well-dispersed resin.^{169, 170}

Various acrylate monomers have been used such as 1,6-Hexanediol Diacrylate (HDDA), Trimethylolpropane triacrylate (TMPTA), Ethoxylated pentaerythritol tetraacrylate (PTTA), 2-hydroxyethyl acrylate (HEA), 2-hydroxyethyl methacrylate (HEMA), isobornyl acrylate (IBOA) and isodecyl methacrylate (IDA).^{162, 171-173} All have slightly different refractive indexes and viscosities in monomer form, meaning although they've all been utilised, each will produce a resin with different properties that can be more appropriate for specific ceramic powders. HDDA is arguably the most common monomer used in CSL owing to its relatively low viscosity and a refractive index close to some of the most common powders used for printing, namely alumina and silicon dioxide.

The aim of developing a ceramic resin was to achieve a resin loaded with cordierite powder that could achieve cure depths up to 250 microns with a viscosity below 5 Pa.s while having a solid loading above 50 wt.%. The remainder of this chapter explains the process conducted to achieve this using a stepwise process which could be adapted for any future development or optimisation of a ceramic resin. The

base resin consisted of two monomers, HDDA and TMPTA, which were selected based on information found during the literature review and the small difference in RI. (HDDA = 1.4560, TMPTA = 1.474) The amount of each component included thereafter was carefully selected to help achieve the ideal properties of the ceramic resin.

2.5. 3DP Substrate Testing

There is limited literature on ceramic substrates for the application of methane oxidation produced by digital light processing technology, particularly including a comparison with a commercial substrate, so a more general literature review was conducted around DLP printed substrates for general gaseous environmental catalytic reactions.

The first paper of interest was published by Santoliquido et al. named 'Structured Alumina Substrates for Environmental Catalysis Produced by Stereolithography'.¹⁰² Alumina lattices were manufactured using stereolithography technology and employed as ceramic substrates for the gaseous catalytic reduction of NO_x. A closed wall lattice was produced using rotated cubic cells with a cell size of approximately 2 mm and strut diameters of 0.55 mm, which is displayed in Figure 25. A V₂O₅-WO₃TiO₂ catalyst was selected as a washcoat, and a comparison was made with a 400

CPSI honeycomb monolith washcoated in the same catalyst. Two samples of the 400 CPSI monolith were produced: M1, with the same catalyst mass per unit volume as the 3D substrate and M2, with the same catalyst mass per unit specific surface. The surface area of the 3D printed lattice was approximately 0.5 times that of the 400 CPSI honeycomb monolith. Therefore, when using a fixed weight of catalyst per unit volume, the surface coverage for the honeycomb M1 monolith was half that of

the 3D substrate. When matching the surface coverage of the monolith and 3D substrate, the mass of the catalyst was double for the M2 monolith compared to the 3D substrate.

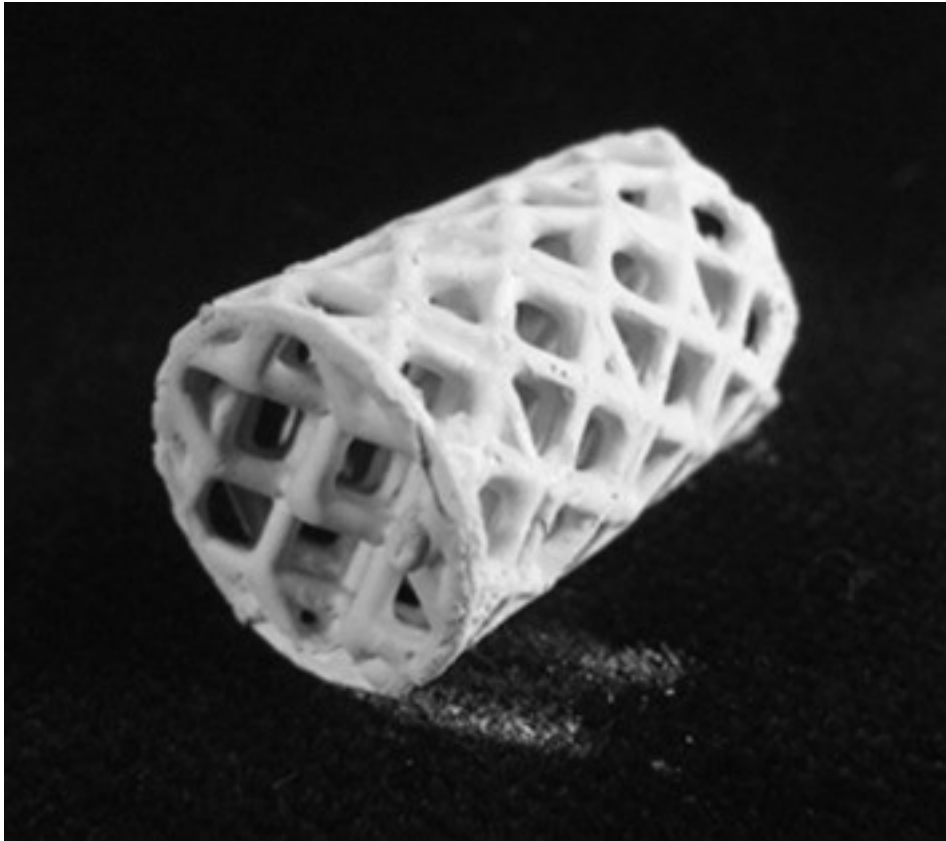


Figure 25: Image of the Al_2O_3 3D printed substrate used for testing by Santoliquido et al.¹⁰²

When tested under the same conditions with a matching flow rate, the 3D substrate performed slightly worse than the M1 and M2 monoliths, with the most significant difference being around 15 % at maximum conversion. So, to compare these substrates more fairly, the author tested the 3D substrate at a lower GHSV. This lowered the surface area load on the catalyst to match that of M1 and M2. When the 3D substrate and 400 CPSI monoliths, M1 and M2, were compared experimentally with a similar surface area load of reactant per unit of catalyst, the 3D substrate had

a very similar reactivity to the M2 monolith, if not slightly better, whilst M1 performed worse than the 3D substrate. This translates to the 3D substrate performing better than either honeycomb monolith when the mass of reactant per unit surface area of the catalyst substrate was equal. Therefore, if considering the surface area as proportional to the amount of precious metal required, less precious metal is needed to yield the same reactivity, reducing the cost. Conclusions were made that the turbulent flow of the 3D substrate contributed to this improved reactivity.

A second study investigating 3D printed structures for gaseous catalytic reactions includes that by Papetti et al., 'Additive manufactured open-cell polyhedral structures as substrates for automotive catalysts'.¹⁷⁴ A numerical model was first conducted around the mass transfer of different polyhedral lattices where the optimal cell was selected as the Cubic 45 with a strut size of 0.6 mm. A comparison was made with a 400 CPSI honeycomb monolith, and it was concluded that an open-cell polyhedral lattice has a higher mass transfer than honeycomb monoliths but with a surface area around 1/6 of the size.

Regarding substrate manufacturing, both the 3D printed substrate and the honeycomb monolith were manufactured to contain the same number of channels. The washcoat, an Al₂O₃-Pt catalyst consisting of around 1.5 wt.% Pt was applied to both substrates using a dipping method. The final mass of the catalyst applied was about 0.80 g or 36 % of the weight of the substrate. Due to the difference in the weight and surface area of the substrates, the final coating thickness was around double for the 3D substrates compared to the honeycomb monolith, making the inner parts of the 3D printed substrates coating inaccessible. The catalytic experimental set-up proceeded in a 13 mm quartz tube under a gas feed of 500 ppm C₃H₆, 8 % O₂

balanced with N₂. Experiments were conducted over a 50 – 600 °C temperature profile with a heating ramp of 10 °C/min.

The 3D substrate and the HC monolith achieved very similar conversions. Kinetic investigations showed that the mass transfer for the 3D printed substrate was around two times higher than the honeycomb monolith. This was accounted to the intricate, interconnected internal geometry increasing the contact probability of the species with the substrate walls. Thus, AM polyhedral structures required proportionally less wetted surface area and, therefore, less precious metal than the honeycomb monolith to achieve the targeted pollutant conversion.

A third paper of interest was authored by Nikolina Kovacev et al. titled ‘The synergy between substrate architecture of 3D printed catalytic converters and hydrogen for low-temperature aftertreatment systems’.¹⁷⁵ DLP technology was successfully utilised to manufacture two complex lattice substrates, D45 and ED, both displayed as CAD images in Figure 26 and printed substrates (A and B respectively) in Figure 27. Both substrates and a honeycomb monolith were washcoated in an Al₂O₃-Pt-Pd catalyst with a 2.5 wt.% PGM loading applied via dip coating.

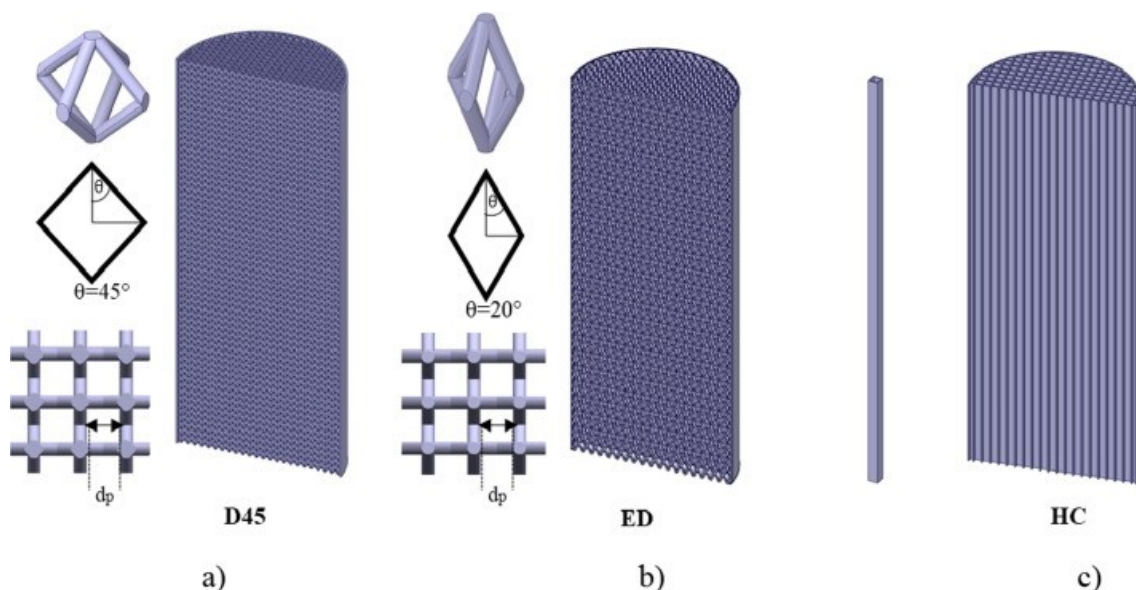


Figure 26: CAD designs of three substrates produced for gaseous catalytic studies by Kovacev et al.¹⁷⁵

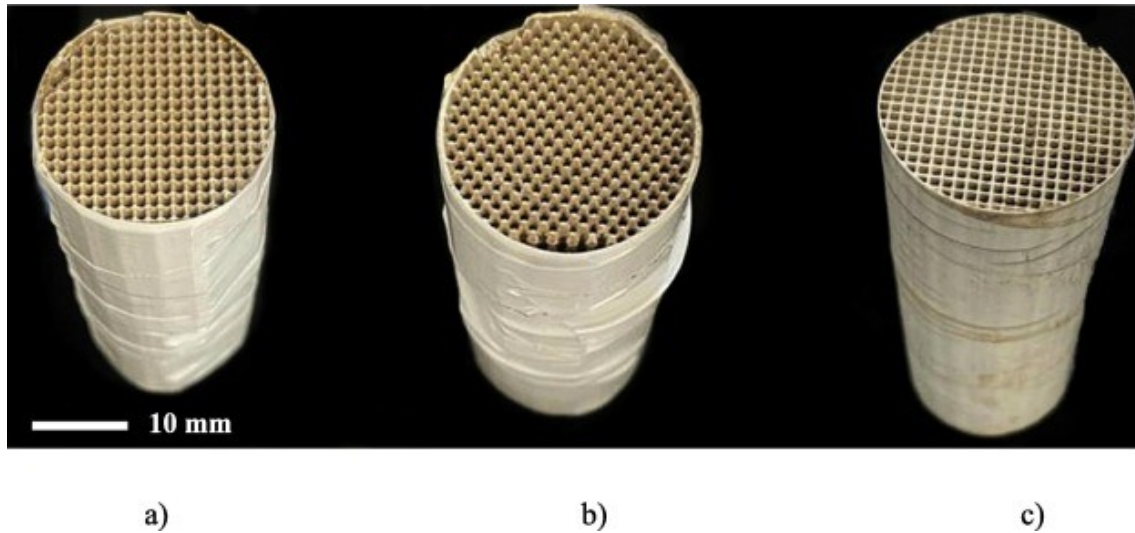


Figure 27: Images of the final washcoated substrates tested by Kovacev et al.¹⁷⁵

The test procedure was conducted in the exhaust flow of a single-cylinder diesel engine. Samples were placed in a tubular Carbolite Gero furnace where the temperature increased from 100 to 400 °C at a heating rate of 3 °C/min. The conversions were calculated for CO, THC and NO.

The 3D printed substrates outperformed the honeycomb monolith across the full temperature range. All the substrates' light-off curves followed the same pattern, including a low conversion at low temperatures and an increase in conversion as temperature increased. The D45 3D printed substrate displayed a 23 % lower lightoff temperature compared to the honeycomb monolith and was the best-performing substrate of the three. The second 3D printed substrate, ED, also outperformed the honeycomb monolith but performed slightly worse than the D45 substrate which was accounted for by the 13 % lower surface area. Both the 3D

printed lattices had approximately 20-30 % lower surface area compared to the honeycomb monolith but this did not seem to have a detrimental effect on their performance. This implies the flow regime within the substrates has a more significant effect on activity than the surface area. The 3D printed substrates utilise their surface area more efficiently resulting in greater conversion. The research proved the important effect 3D printing can have on producing more efficient substrates for gaseous catalytic conversion.

The literature review generally resulted in a consensus that the 3D printed substrates produced outperform the HC monoliths, especially at low temperatures. The reason for this was associated with the improved mass transfer results due to a higher probability of particle collisions between the reactants and the catalyst. All the papers reviewed also concluded that 3D printed monoliths can achieve targeted catalytic conversion with a lower amount of catalytic washcoat compared to the HC monoliths due to their lower surface area requiring less catalyst than a traditional HC monolith. This combination creates a great opportunity to exploit the cost efficiency of 3D printed monoliths compared to HC monoliths considering target conversion can be achieved with less catalyst, the main expense of exhaust after-treatment systems. The literature focuses very heavily on various repeated cubic cells constructing the internal geometry of the 3D printed substrates with a lack of variation outside of this.

This chapter includes the catalytic activity results of an investigation into DLP and robocast-produced substrates for the purpose of methane oxidation. The substrates manufactured in previous research, explained in chapters 2 and 3, were washcoat in the Zeolite Y-PdPt catalyst with a 10 wt.% PGM loading and tested under the conditions for the complete oxidation of methane.

3. Characterisation Techniques

Chapter 3 covers the characterisation techniques utilised throughout this thesis. This includes background information on any techniques, the science of how each technique works and any working conditions used for testing during these studies.

In these studies, a Rigaku NEX-CG XRF spectrometer was used for elemental analysis using the loose powder method under vacuum. BET measurements were conducted using a Micrometrics ASAP 2020 instrument at 77 K. Preparation of the samples for degassing was done at 300 °C under vacuum ($p < 10^{-3}$) for 3 hours prior to analysis under nitrogen flow. The surface area and isotherms were analysed using the standard BET procedure in a pressure range of 0.05-0.30. X-ray diffraction (XRD) was conducted in ambient conditions using a Panalytical X'Pert Powder diffractometer with Cu K α radiation ($\lambda = 1.5406 \text{ \AA}$). All powder diffraction patterns were recorded from 4 to 120° 2 θ with step size 0.013° and step time of 50 s, using an X-ray tube operated at 40 kV and 30 mA with a fixed ¼ ° anti-scatter slit.

Shrinkage was measured using a microcaliper with measurements of the height (z-axis) and circumference (x/y-axis) recorded, as it is understood that shrinkage can vary along either axis.¹⁷⁶ Measurements were recorded in mm and calculated as % of shrinkage compared to the design's original dimensions. Scanning electron microscopy images were taken using a ZEISS Supra 40VP microscope.

3.1. X-ray Diffraction

X-ray diffraction (XRD) is a non-destructive technique used to identify crystalline phases. Figure 28 shows an example of a Faujasite zeolite X-ray diffraction pattern from literature.

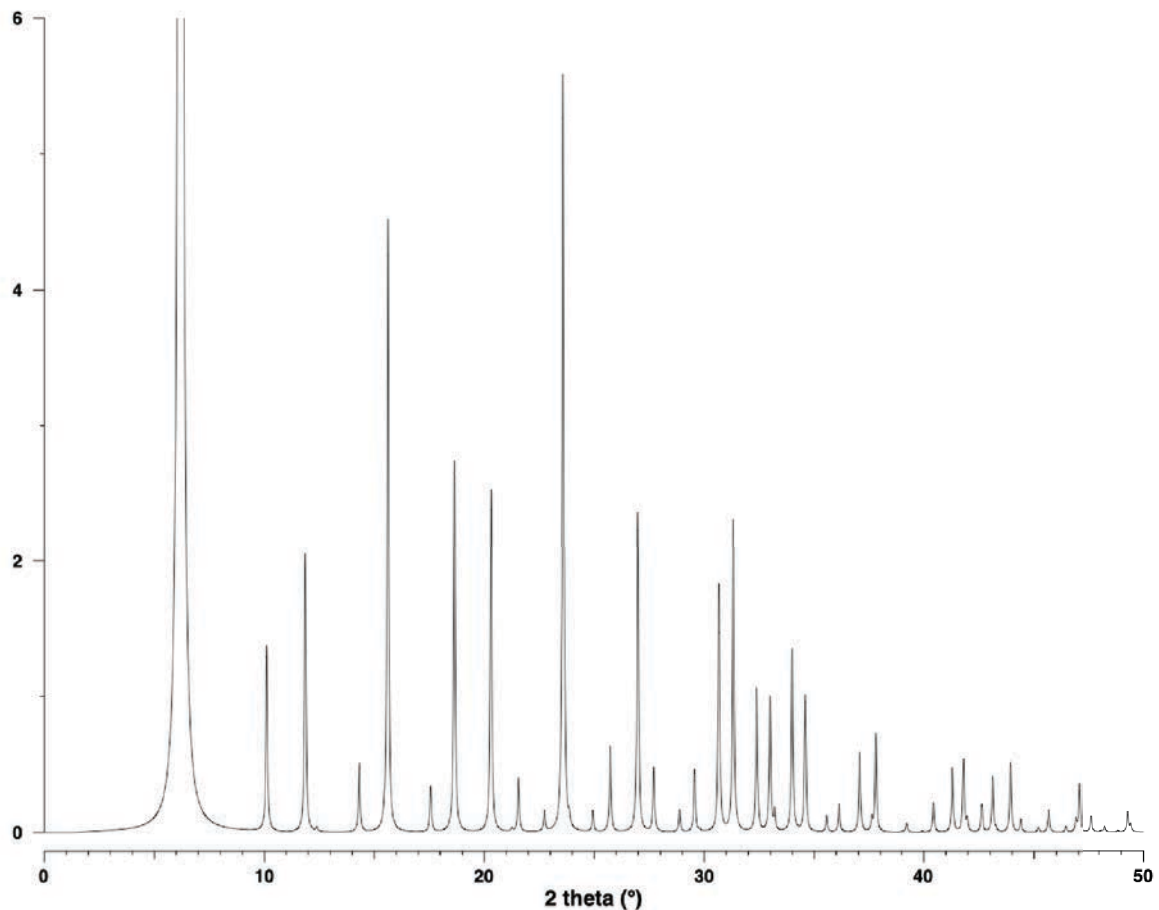


Figure 28: XRD pattern of a Faujasite zeolite.¹⁷⁷

3.1.1. Crystal Structure

Around 95% of solid materials can be described as crystalline - the arrangement of atoms, ions or molecules in a regular pattern or lattice. This crystal can be broken down into a series of smaller repeating 'boxes' called the unit cell. The unit cell can be described by its dimensions using three axes' lengths: a, b, and c, with the angles between them named alpha, beta, and gamma.¹⁷⁸ There are fourteen types of unit cells (called Bravais lattices) broken down into seven crystal categories resulting in

over 230 possible space groups of atoms; the three most common cells are called simple cubic, body-centred cubic and face-centred cubic, belonging to the cubic category.¹⁷⁹ To specify the spacing between the atoms in a unit cell, a theoretical lattice plane is drawn through the axis (x,y,z). Since all the atoms in a unit cell are located equally to those in the adjacent unit cell, these planes are used to describe repeat distances between atoms in a crystal. They are labelled with a shorthand notation called the Miller Index. The points where the plane intercepts the axis are recorded as fractions of the cell edge lengths. The reciprocal of these then gives the Miller indices of the plane and are labelled (h,k,l).¹⁸⁰ For example, a plane intersecting the unit cell halfway up the x-axis, a full length up the y-axis, and not intersecting the z-axis at all ($\frac{1}{2}x, 1y, 0z$) would be given the miller index (2,1,0) as shown in Figure 29.

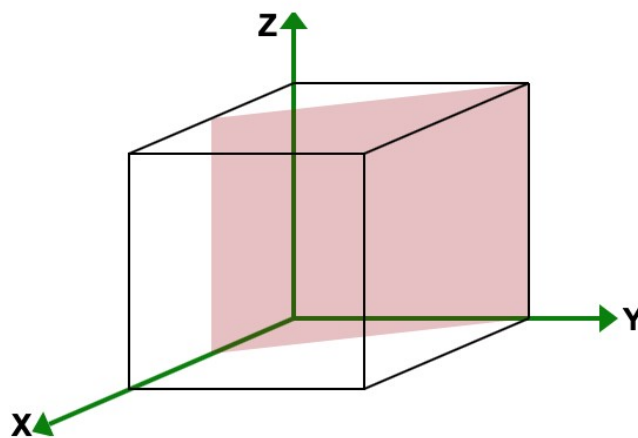


Figure 29: An example of a crystal plane with the miller index (2,1,0).

When X-rays interact with the atoms in a unit cell, a diffraction pattern is created, allowing the identification of these crystalline phases.

3.1.2. Diffraction

When electromagnetic radiation is directed towards a physical object, the sample causes it to diffract. A sample with a different arrangement of atoms will diffract the

radiation differently, thus creating a unique diffraction pattern for each varied arrangement of atoms – likened to a fingerprint. To produce significant diffraction, the wavelength of the radiation must be similar to the spacing between the atoms.¹⁸¹ For this reason, X-rays (with a wavelength of around 0.1-10 nanometres, an equal order of magnitude to the spacing between crystal lattice planes) are used to produce a diffraction pattern for atomic crystals. As the X-rays interact with the electrons of an atom, spherical waves are diffracted in all directions. Although most waves destructively interfere and cancel each other out, a small amount constructively adds in specific directions, as determined by Braggs Law.¹⁸²

$$n\lambda = 2d \cdot \sin\theta \quad (\text{Eqn 4})$$

n is an integer, λ is the wavelength of the X- rays, d is the spacing between the lattice planes and θ is the angle at which the X-rays hit the sample (incident angle).

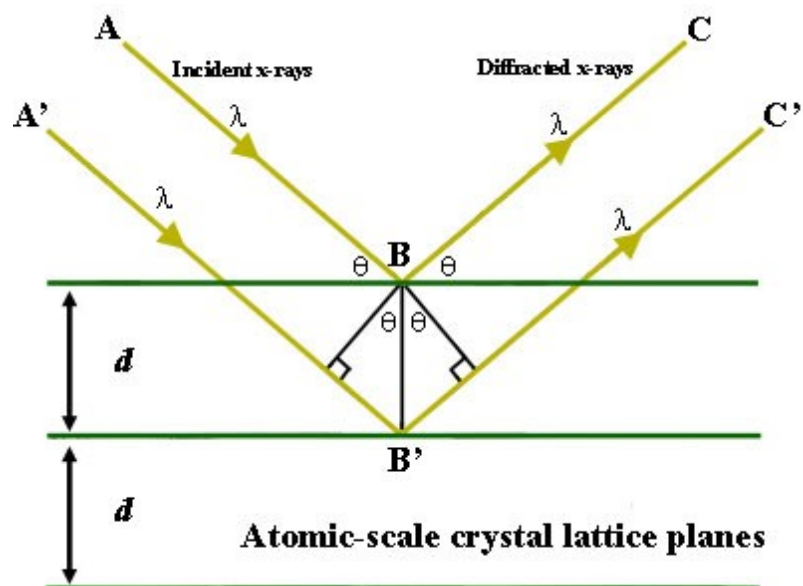


Figure 30: The interaction of X-rays with a crystal structure during X-ray diffraction.¹⁸³

Braggs law relates the wavelength and diffraction angle of the X-rays to the lattice spacing. Figure 30 helps explain this. If the reflecting X-rays hitting the ‘top’ and

'bottom' plane are an integer number of wavelengths difference, the incident and reflecting angle are equal. The waves are in phase and constructively interfere, resulting in detectable diffracted X-rays.¹⁸⁴ If θ and d at which the X-rays were constructively diffracted are known, Bragg's law can then be used to calculate the distance between the lattice planes (d), which can then be assigned to a crystal by comparing it to standard reference patterns. In this study, XRD was conducted using a Panalytical X'Pert Powder diffractometer with Cu K α radiation ($\lambda = 1.5406 \text{ \AA}$).

3.2. Brunauer-Emmet-Teller

Brunauer-Emmet-Teller (BET) is a technique used to measure the surface area of solid or porous materials. The measurements of surface area are simply based on the adsorption of gas.¹⁸⁵ There are five practical steps to BET analysis: Degassing the sample, applying a vacuum to the sample tube, dead volume measurement using He and an evacuation of the He, the adsorption of N₂ and finally, the desorption of N₂. The sample is first degassed to remove any water or contaminants from the sample before being transferred to the analysis port. An N₂ Dewar is then raised to cover the sample and maintain a constant temperature where a partial vacuum is created within the sample tube. The He is then injected to measure the dead volume - the equivalent of a blank run as He does not adsorb onto the sample. After these steps, measured amounts of N₂ are injected using a calibrated piston for N₂ adsorption to occur. After the saturation pressure is achieved, the N₂ is desorbed, measured, and displayed as a BET isotherm – the amount of gas adsorbed as a function of relative pressure - which can then be used to help calculate the monolayer capacity of the solid sample using the BET equation¹⁸⁶:

$$\frac{V_{rel} \cdot P_0}{V_{rel} \cdot P_0 - V_{rel} \cdot P_0} = \frac{C \cdot V_m}{V_m + C \cdot V_{rel} \cdot P_0} \quad (Eqn 5)$$

Where V is the volume of the gas adsorbed, (P/P_0) is the relative pressure, V_m is the volume of adsorbate as a monolayer, and C is the BET constant. This can be plotted as a straight line graph where the gradient and intercept can be taken as numerical values allowing a rearrangement to solve for V_m and C . Using the monolayer capacity and the size of the N_2 particle, the surface area of the sample can be calculated using the equation below¹⁸⁷:

$$SA_{BET} = \frac{V_m}{V} \times N_A \times A \quad (\text{Eqn 6})$$

SA_{BET} is the surface area, V_m is the volume of the monolayer (calculated using the rearranged BET equation), N is Avogadro's number (6.022×10^{23}), and A is the cross-sectional area of the adsorbing molecule, N_2 in this instance, and V is the molar volume of the adsorbed gas. Figure 31 below is an example of a BET isotherm from literature.

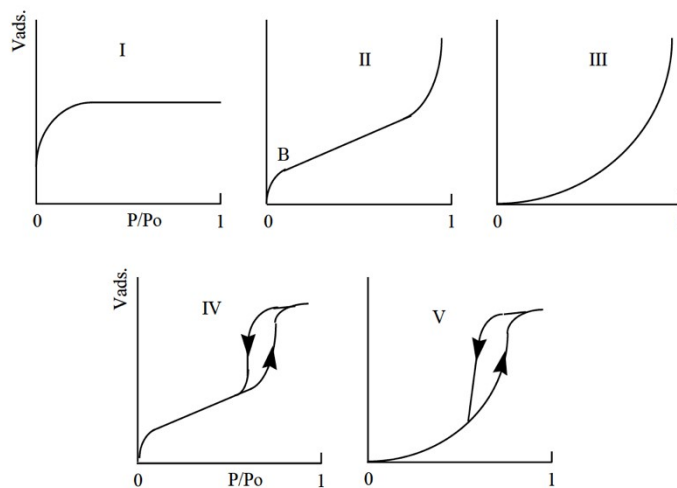


Figure 31: Nitrogen adsorption isotherms.¹⁸⁸

Numerous assumptions occur when using BET analysis¹⁸⁹:

- 1) All non-adsorbed gaseous molecules behave as an ideal gas.

- 2) Adsorbates adsorb infinitely onto a solid in layers.
- 3) All sites on the surface have equal adsorption energies (a site is defined as an area on the surface where one molecule can adsorb) and can only be occupied by one particle.
- 4) The adsorbed molecules are immobile.
- 5) There are no interactions between the adsorbed molecules and their layers, meaning the adsorption of the gas at one site occurs independently of any adsorption at neighbouring sites.

In this study, BET measurements were conducted using a Micrometrics ASAP 2020 instrument, shown in Figure 32.



Figure 32: A Micrometrics ASAP 2020 instrument.¹⁹⁰

3.3. Scanning Electron Microscope

Scanning electron microscopes (SEM) allow us to achieve a high-resolution image of a surface in the magnitude of nanometres. Simply, a thin beam of electrons is scanned over the sample's surface, and the electrons emitted by the sample are detected with the signal being used to produce an image.¹⁹¹ Figure 33 displays a typical scanning electron microscope setup. The electron beam is accelerated by up to 30kV - inside a vacuum as electrons do not pass through the air – past a series of magnetic lenses, through an aperture, into a scanning/deflection coil and finally, through a second aperture to form a focused beam before hitting the sample. The lens is responsible for demagnifying the electron beam (to around 2-10 nm), whilst the scanning coil allows the user to focus the direction of the electron beam over the surface of the sample. The emitted electrons are then picked up by various detectors and interpreted to produce an image.¹⁹²

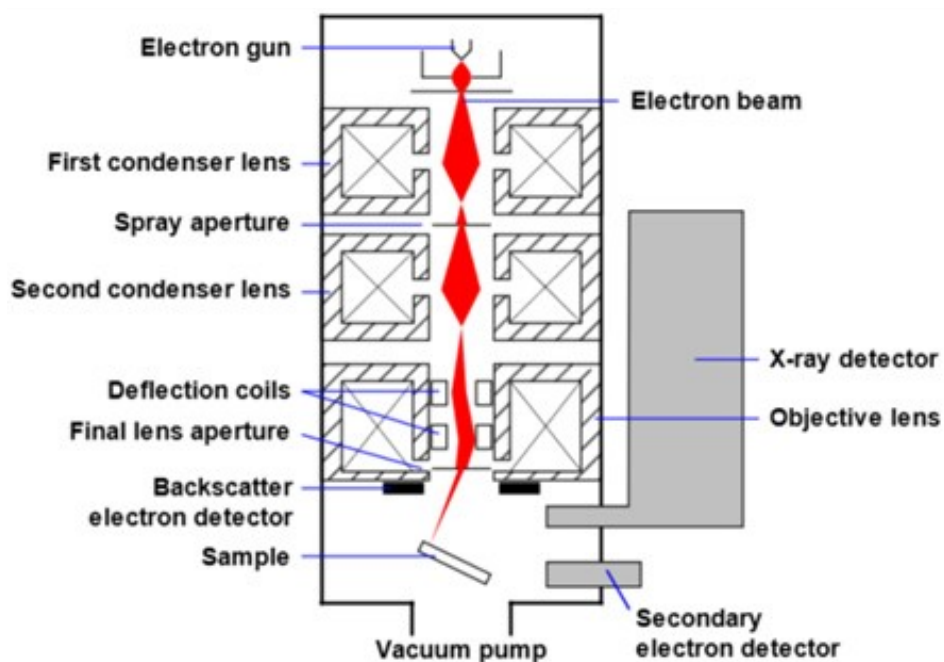


Figure 33: A typical SEM instrument set-up.¹⁹³

3.3.1. Interaction of electrons with the specimen

When high-energy electrons strike a sample, several signals are generated by backscattered and secondary electrons, as well as characteristic X-rays.

Backscattered electrons are the reflected electrons from the incident beam once scattered within the sample. The detector is usually placed around the final lens because, as the name suggests, the electrons are typically scattered back in the direction of the incident beam. They have much more energy (between 50 eV and the energy of the incident beam) than the secondary electrons and tell the user more about the deeper regions of the sample and its crystallographic arrangement.

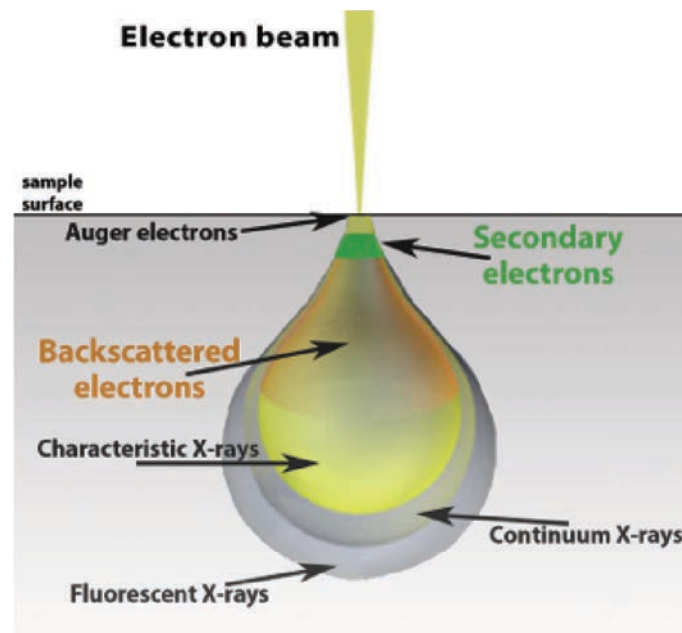


Figure 34: The behaviour of an SEM electron beam with the sample surface.¹⁹⁴

The secondary electrons are the emission of the valence electrons from the sample's atoms and have much lower energy (>50 eV). Since they have much lower energy, any produced deep in the sample are usually absorbed. The result is that the sample's surface has usually produced any secondary electrons detected. The secondary electrons are the most widely used signal for surface analysis and are detected using an Everhart-Thornley scintillator detector.¹⁹⁵ A scintillator detector emits photons when struck by electrons, which are collected by a light guide and

transported to a photomultiplier for detection. It is also surrounded by a Faraday cage with a slightly positive charge to attract the negatively charged secondary electrons. By reducing the voltage of the electron beam, there is a higher number of lower energy electrons, increasing the resolution of the surface image.¹⁹⁶ Figure 35 below is a published SEM image of a catalyst from literature.

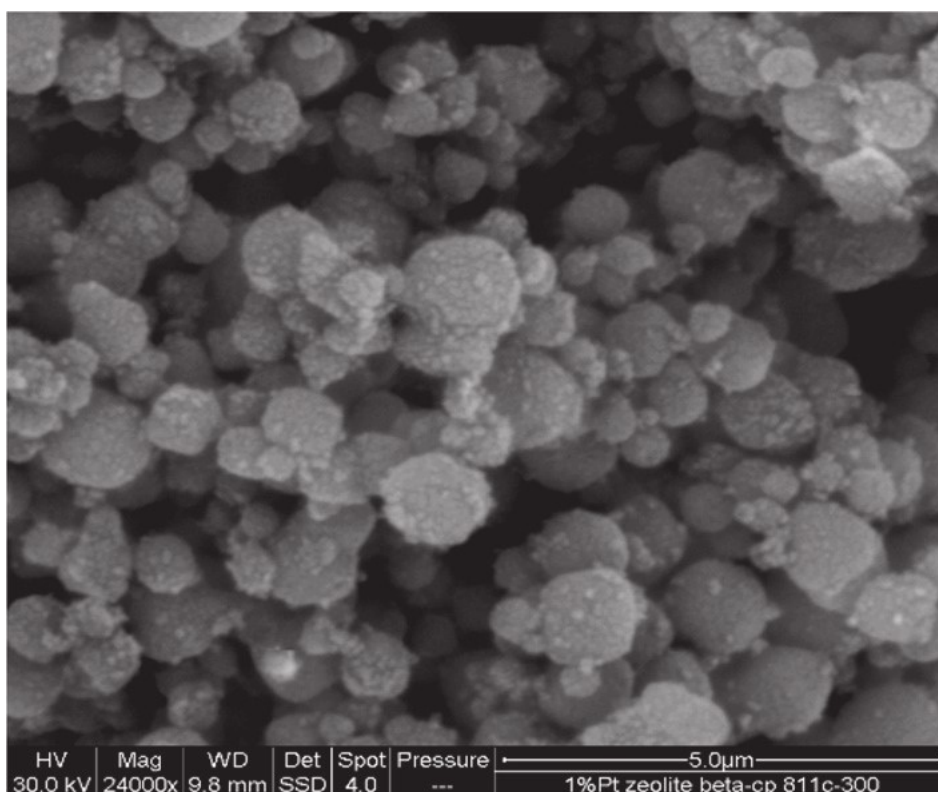


Figure 35: SEM image of a 1.0 wt.% Pt/zeolite beta catalyst.¹⁹⁷

3.4. X-Ray Fluorescence

X-ray fluorescence (XRF) is a common non-destructive analysis technique used for determining the elemental composition of liquids and powders. XRF analysers ultimately measure the energy emitted by a sample when targeted by a high-energy X-ray source.¹⁹⁸ Incoming primary X-rays are targeted towards the sample by a controlled X-ray tube. When the atom is struck by X-rays of sufficient energy - larger than the K or L shells binding energy - an electron from the atom's internal orbital

shells is dislodged. The atom then regains stability as an electron from the outer shell drops down to fill the void in the lower shell. This is accompanied by a release of electromagnetic energy within the wavelength of X-rays. The energy of this X-ray is equivalent to the difference between the two states of the electron, which is measured by a detector in the XRF instrument. Thus, creating distinctive lines within the spectra as each type of orbital transition emits unique X-rays. The energy of the lines can be associated with the type of elemental, while the height of the peak can usually be associated with the element's abundance. This spectrum can then be compared to standard reference patterns to identify unknown elements.^{199,200, 201}

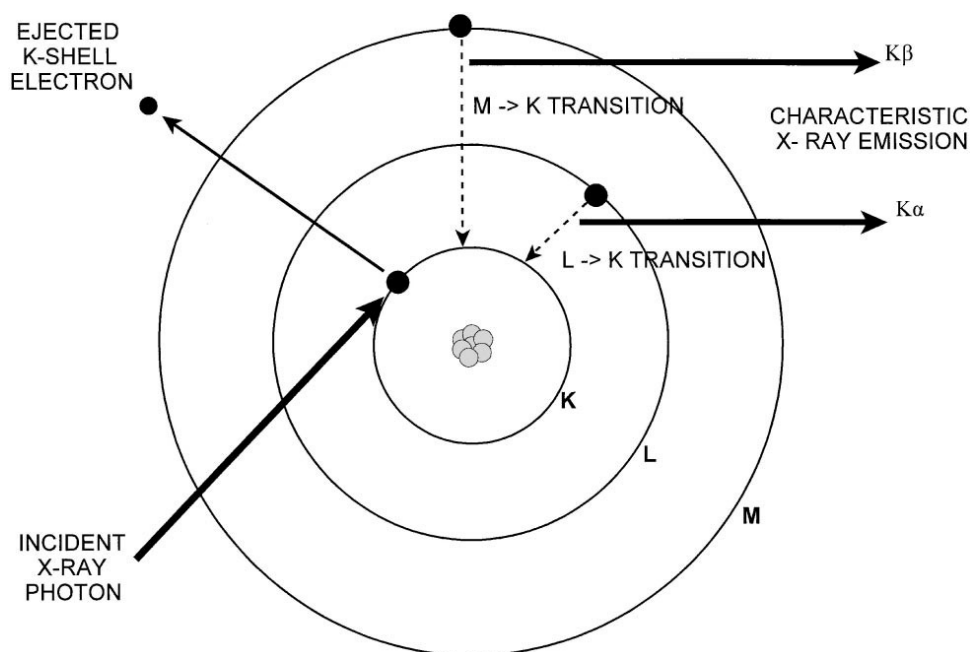


Figure 36: The behaviour of electrons within an atom during X-ray fluorescence analysis.²⁰²

3.5. Thermal Gravimetric Analysis

Thermal gravimetric analysis (TGA) measures a change in the mass of a sample as a function of temperature or time. Measurements are primarily conducted to determine the change in a sample's composition and the thermal stability of a

sample. This data can also be used to calculate the moisture/volatile content of the material.²⁰³

The components of a TGA include a balance, a furnace, and a temperature controller – all connected to a computer interface which collects, stores, and processes the data to produce a graph. The balance operates on a null-balance principle. When at the null position, an equal amount of light shines on two photodiodes. If the balance moves, an uneven amount of light will shine on each photodiode. A current is then applied to the meter movement to return the balance to the null position. The amount of current applied is proportional to the weight loss of the sample. The graph produced usually consists of mass or mass % change on the y-axis and time or temperature on the x-axis.²⁰⁴ A Perkin 4000 TGA was used in this study.

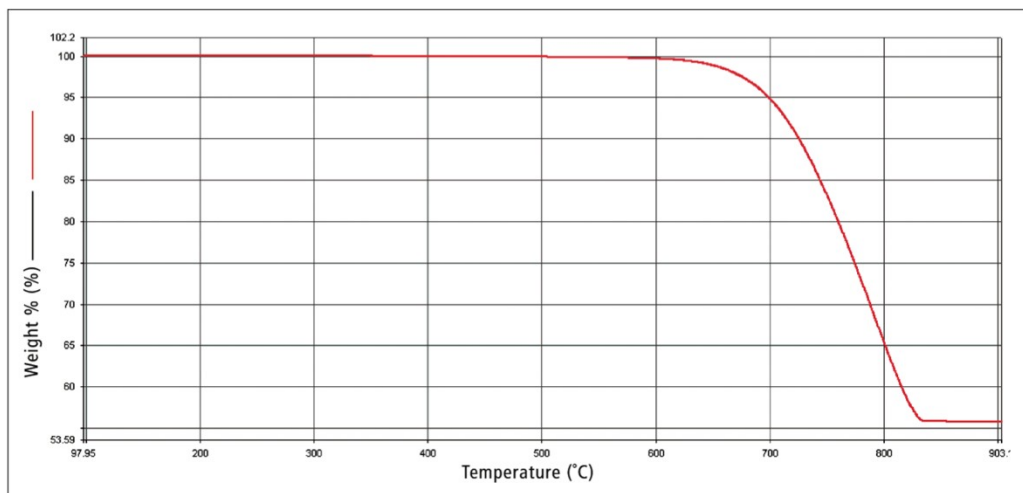


Figure 37: An example of a result graph produced by a Perkin 400 TGA instrument.^{205, 206}

3.6. Shrinkage

Shrinkage is a common side effect of the mandatory debinding and sintering steps required for ceramic manufacturing. Knowing the amount of shrinkage a sample undergoes when sintered allows the printing design to be scaled up, meaning the

dimensions of the final part can be more accurate to those required.²⁰⁷ To understand this effect, test parts were measured after printing and remeasured after sintering so the amount of shrinkage could be calculated allowing the designs to be scaled up for future prints.

4. Methodology

Chapter 4 begins by covering the methodology of designing and printing 3D monoliths using both robocasting and digital light processing techniques as in line with one of the aims of this thesis. This includes the step-by-step process of refining and improving a ceramic DLP resin for its intended purpose which was a very timeconsuming process. The synthesis of any catalysts used throughout this study is also explained with conclusions made about why any decisions were made for the final manufactured prototype.

4.1. 3D Printing Methodology

4.1.1. Design Method

When creating the new substrate designs, several steps were needed to develop a software file that different 3D printers could use. The first step was to produce the digital CAD drawing. The second was to slice this CAD design into layers which could be printed individually by the printer. Simplistically, this is a file consisting of each layer's image. The third entailed translating these sliced CAD files into a new file type, which could be understood by the printer being used.

4.1.2. Autodesk Fusion 360

Autodesk's Fusion 360 was selected as the 3D modelling CAD software to design the various substrates. The different wall thicknesses produced in the CAD designs were a limitation of the 3D printing technique used. The initial designs all had dimensions of Ø2.0 cm x H2.0 cm. Fusion 360 was then applied to scale up the design to account for any shrinkage which occurred later in the printing process.

4.1.3. Ultimaker Cura

Cura was chosen as the slicing software for the CAD designs. Cura is an open-source application supplied by Ultimaker and can be applied to slice any 3D CAD model. The CAD file is imported into the program, where the software allows the user to vary the thickness of each slice, whilst informing the user whether the printer will have any issues - originating from the design - when attempting to print. Once confirmed, Cura can export the sliced designs using various file types suitable for the selected printing method.

4.2. Robocast Substrate Manufacturing

4.2.1. Materials

Kaolin powder ($\text{Al}_2\text{H}_4\text{O}_9\text{Si}_2$), polyethylene glycol (PEG)(Mn=400) (Sigma-Aldrich), methyl cellulose (Sigma-Aldrich), bentonite ($\text{Al}_2\text{H}_2\text{Na}_2\text{O}_{13}\text{Si}_4$), (Nanocor), distilled water (d.H₂O).

4.2.2. Methodology

A ceramic paste was prepared by mixing the kaolin powder ($\text{Al}_2\text{H}_4\text{O}_9\text{Si}_2$), bentonite ($\text{Al}_2\text{H}_2\text{Na}_2\text{O}_{13}\text{Si}_4$), (Nanocor) and methyl cellulose (Sigma-Aldrich) using a rotary ball mill (Retsch planetary ball mill PM 100) at 200 rpm for 30 minutes. Methyl cellulose acted as a printing binder, while bentonite acted as a ceramic filler to improve the density of the final sintered ceramic product. The distilled water and polyethylene

glycol (PEG)(Mn=400) (Sigma-Aldrich) were vigorously mixed at a 1:3 ratio before gradual addition to the solid mix. Both act as a solvent for the paste, while polyethylene glycol also improves the elasticity. The material was then kneaded and well mixed before being loaded into the 3L pressured clay tank to be extruded via the Delta WASP 4070 LDM printer. The 2x2 cm models took approximately 25 minutes to print using a print speed of 10 mm/s, resulting in a final clay model to be posttreated. Figure 38 below shows the Delta 4070 printer during printing. Figure 39 is an image of the five X-angle rotated substrates printed before the post-processing procedure.

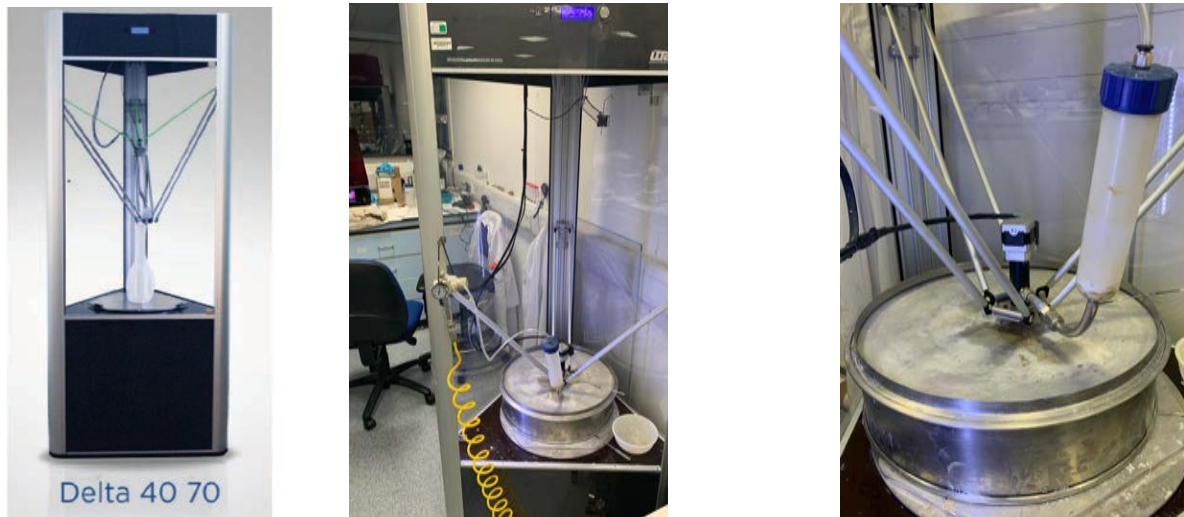


Figure 38: Images of the WASP Delta 4070 robocast printer used in this study.



Figure 39: Image of the robocast substrates printed, with a variation in the X-angle, before post-processing.

4.2.3. Robocast Post Processing

Post-treatment started by drying the sample at 80 °C for 24 hours. This removed much of the water from the sample and helped maintain the structure's shape while helping to reduce cracking later in the process. After 24 hours, the sample was cured and sintered. The initial temperature step was to 350 °C at 1 °C/min and held for 3 hours. The subsequent step was to 1100 °C at 5 °C/min and held for 2 hours. The initial temperature burns away the organic polyethylene glycol and methylcellulose, and then the final temperature sinters the elemental composition to form a new crystal network between the atoms and improve the mechanical stability.

4.3. Digital Light Processing Resin Development

4.3.1. Materials

Trimethylolpropane triacrylate (TMPTA), (Alfa Aesar, Stabilised). 1,6-hexanediol diacrylate (HDDA), (Sigma-Aldrich, Technical grade, 80%), cordierite powder

(2MgO-2Al₂O₃-5SiO₂)(Stanford Advanced Material)(Particle size >1.6µm), IGEPAL CO-720 (Sigma-Aldrich, Mn~720), phenylbis(2,4,6-trimethylbenzoyl) phosphine oxide (Sigma-Aldrich).

4.3.2. Resin Preparation

This resin consisted of TMPTA and HDDA at a 50:50 ratio and was consistently used throughout testing. The dispersant was first dissolved in distilled water before the gradual addition of the cordierite powder. This cordierite slurry was dried and crushed and given the name IGECORD to be used for the later resin synthesis. The TMPTA and HDDA were mixed and stirred overnight before the gradual addition of the required amount of IGECORD. This slurry was further mixed for 24 hours before the addition of the photoinitiator. After further mixing for 4 hours to ensure uniform consistency, this mixture was used as the resin for printing.

4.3.3. Resin Optimisation

4.3.3.1. Dispersant

The role of a dispersant is to improve the dispersion and stability of the solid particles in the resin.²⁰⁸ An adsorption mechanism occurs where the dispersant forms a sequence of hydrophobic chains around the solid particles, which repel each other, avoiding agglomeration.²⁰⁹ There is no ideal dispersant concentration for all ceramic resins.²¹⁰ At a concentration too low, the particles still agglomerate as there is not enough dispersant for sufficient solid surface coverage. If the concentration is too high, the free dispersants are proven to promote flocculation in line with the DLVO theory, and sedimentation can increase.¹⁷⁰ Therefore, an optimum amount of dispersant is required to improve the dispersion stability through steric hindrance and electrostatic repulsion. One way to investigate this is to conduct a sedimentation

test. Sedimentation volume as a function of time is a good indicator to the extent of ceramic particle stability within a resin. The smaller the sedimentation ratio, the larger the degree of sedimentation and the less stable the resin. This indicates if too much or too little dispersant has been included.²¹¹

Sedimentation studies were carried out using a fixed solid loading (40 wt.% of resin) in 8 mL of resin using 15 mL centrifuge tubes before measuring the height of the sediment residue as a function of time. The dispersant concentration is recorded as % of solid weight. Figure 40 shows the results of sediment height v time over four hours. Four hours were selected as this was more than enough time to complete the full printing program.

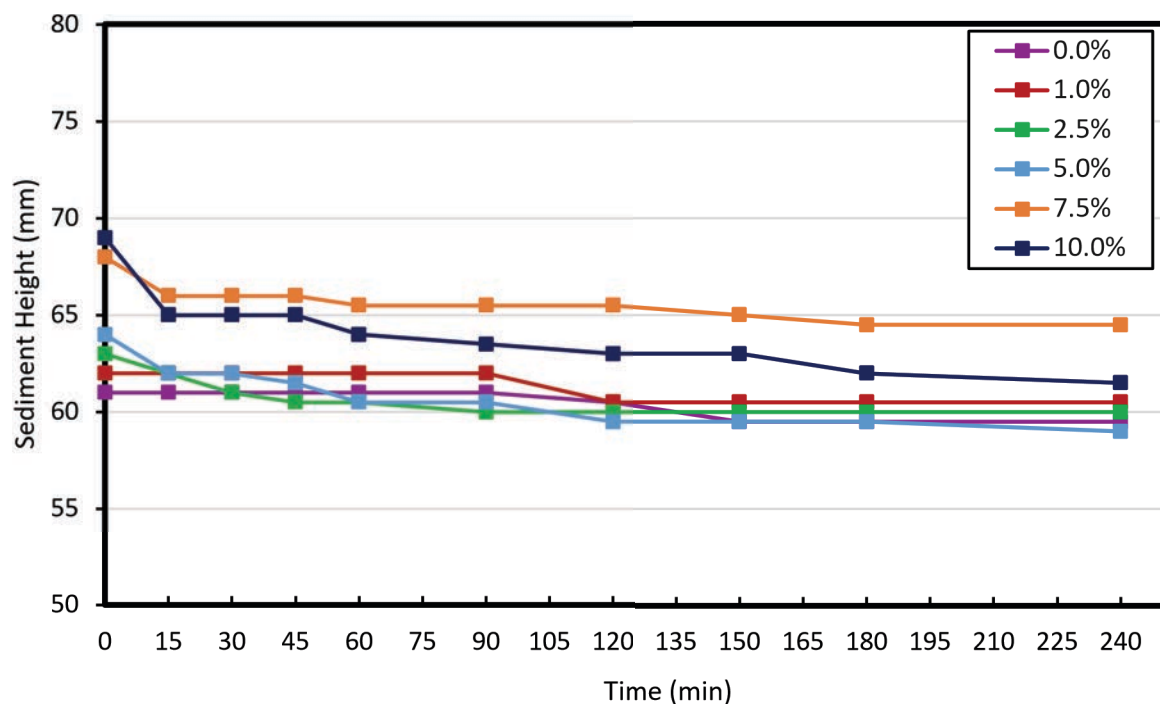


Figure 40: Sedimentation height v time of 6 samples with a varying dispersant concentration, percentage recorded as a wt.% of the solid content, and a fixed solid loading (40 wt.%).

0 % dispersant was included as a controlled study. When $t = 0$, the more dispersant added, the greater the sediment height meaning the dispersant is doing its job when initially added to the solid. The largest sediment height, at $t = 0$, occurred with 7.5 % dispersant. There was a small 2 mm increase between the concentration range of

1.0-5.0 %. However, when the dispersant was increased from 5.0 % to 7.5 %, the dispersion height increased by the largest difference of 4.0 mm to 68.0 mm. This indicates that the most effective increase of dispersant was from 5.0 % to 7.5 %. At 10.0 % dispersant, the sediment height was increased by another 1.0 mm to 69.0 mm showing further dispersion compared to the previous concentration. However, this was a less effective increase for the additional dispersant added, implying a maximum may be close.

As time increased, the sediment height decreased for all samples as the particles begin to settle due to gravitational forces. At $t = 240$ min, the largest decrease in sediment height was recorded for the 10.0 % dispersant, where a decrease of 7.5 mm over 4 hours was recorded. This indicates that the dispersant concentration may have surpassed the optimum, and flocculation may have begun to occur. The trend of these results are in line with a study by G. Ding et al., who trialed five different dispersants at four different concentrations. The study showed how each of the dispersants had an increase in sedimentation height after the optimum concentration had been surpassed.²¹² At dispersant concentrations up to 5.0 %, the sediment height settled between 59.0 – 60.5 mm. Although the change in starting sediment height increased with dispersant concentration, meaning the dispersion improved, the final sediment settling height did not, indicating the surface was not fully covered as the particles agglomerated and fell quicker, hindering the resin stability. A concentration of 7.5 % displayed the largest sediment height after 240 mins at 64.5 mm, suggesting the best dispersion of the solid particles in the resin.

4.3.3.2. Solid Loading

During resin preparation, typically, 50 wt.% of ceramic powder is sufficient in a ceramic resin to produce a product with desirable structural properties. Generally,

higher loadings are desired to improve the structural integrity of the final product whilst simultaneously reducing the shrinkage, deformation, and crack formation during sintering. However, increasing solid loading can increase the viscosity of a resin whilst simultaneously decreasing the cure depth. Therefore, a middle ground is required.¹⁶⁶ The most sensitive factor affected by an increase in solid loading is viscosity. Consequently, maximum viscosity is commonly used to regulate the final solid loading of a ceramic resin.⁸⁹ Printing is not possible if the viscosity is too high, as the resin would not be able to self-level in the vat or recoat the previous layer. Therefore, it is crucial that the resin viscosity is within the working capabilities of a ceramic resin, generally accepted throughout literature as below 5000 mPa.S.^{86, 213}

Viscosity was recorded as the solid loading of the resin was incrementally increased until the maximum viscosity of around 5000 mPa.S had been achieved. Viscosity measurements were conducted using an NDJ-1 rotational viscometer (Baoshishan, China), using 200 mL of resin and a dispersant concentration of 7.5 solid wt.% with the result displayed in Figure 41.

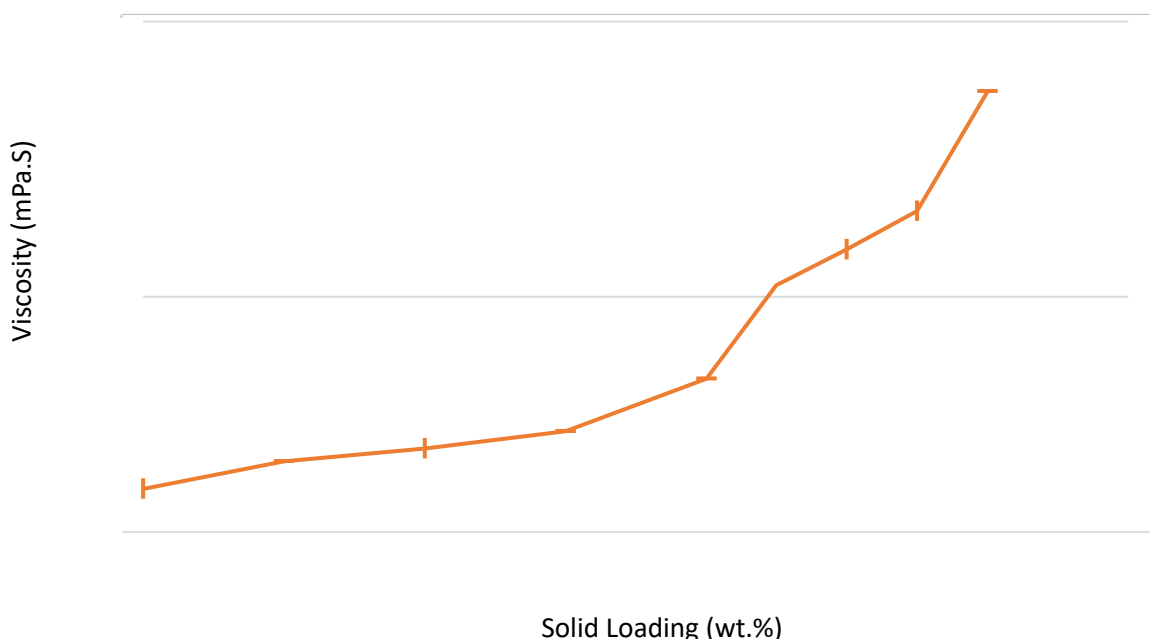


Figure 41: Viscosity v solid loading with solid loading recorded as wt. % of the total resin.

The viscosity of the neat resin (HDDA and TMPTA) used in this study was around 50 mPa.S at 20 °C. This increased towards a maximum of 7500 mPa.s as the solid loading reached 60 wt.%. The target viscosity of around 5000 mPa.S was achieved at a solid loading just below 52 wt.%. When attempting to print at a solid loading over 52 wt.%, the open channels of the monolith became slightly blocked due to an inability for excess resin to drain from the channels in-between printing layers. For this reason, a solid loading of 52 wt.%, with a viscosity of around 4950 mPa.s, was selected for the final resin.

4.3.3.3. Photoinitiator

The concentration of the photoinitiator directly impacts the cure depth. The aim is to find the optimum concentration for curing to occur in the quickest time at the depth required. The cure depth of a resin must be equal to a minimum of 1.5x the sliced layer height. This is to allow the curing layer to sufficiently bond to the previous. This equates to 0.15 mm for the purpose of this study. A lower range of 10-35 % of the sliced layer thickness has been suggested by Zakeri et al but, when tested experimentally, resulted in a distorted greenbody as described in a study by Jakubiak et al.^{214, 215} To optimise the photoinitiator concentration of the resin in this study, seven samples were prepared each varying in photoinitiator concentration ranging from 1.0 – 4.0 wt.%. The cure depth was then measured after being exposed to the UV light for four different lengths of time. The results from the study are shown below in Figure 42.

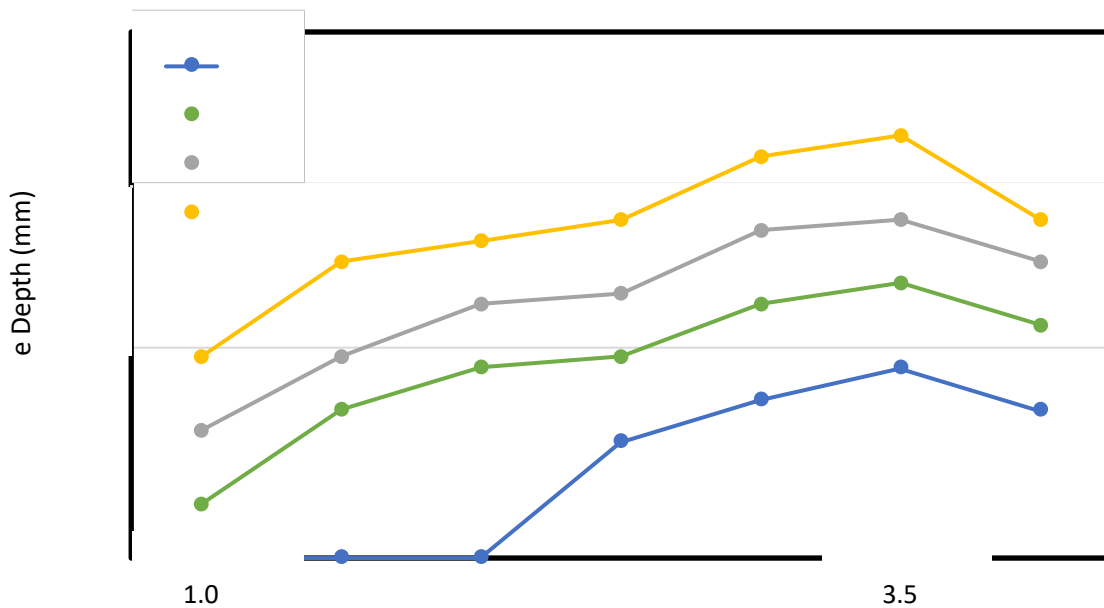


Figure 42: Seve. varying photoinitiator concentration (recorded as wt.%)) v cure depth after being exposed to UV light for four separate time intervals.

At 10 s, up to 2.0 wt.% of the photoinitiator is not enough to activate the polymerisation reaction in the resin. Thereafter, a gradual increase in cure depth can be seen as the concentration of the photoinitiator increases up to 3.5 wt.% for all cure times and photoinitiator concentrations. The maximum cure depth at each time interval occurs at 3.5 % photoinitiator, implying this is the optimum concentration to maximise cure depth. At 4.0 % photoinitiator, the cure depth starts to decrease. It could be argued that this is due to the point of polymerisation reacting so quickly that it hinders the light from penetrating deeper into the resin, ultimately reducing the final cure depth.

The target cure depth of 150 microns is marked with a red line. If the aim is to reduce the cost of the resin, it would be possible to use 1.0 % of photoinitiator for a cure time between 20-25 s. However, for this purpose, the aim is to reduce the

printing time, meaning a concentration of 3.0 % was selected, achieving a cure depth of 150 microns in around 9.8 s. The final resin composition is listed in table 6 below:

Table 5: Final % composition of the photosensitive ceramic resin produced.

Component	% Composition
HDDA	20.55
TMPTA	20.55
Cordierite	52.00
IGEPAL-720	3.90
BAPO	3.00

4.4. Digital Light Processing Manufacturing

4.4.1. Printing Methodology

A Photocentric Liquid Crystal 1.5 digital light processing printer was used throughout this study (Photocentric, Cambridge, UK). The light source had a wavelength of 405 nm and a bulb power of 40 W. The energy at the point of polymerisation was measured as 21.5 mJ/cm². Using the information from the resin optimisation, the layer thickness was set to 100 microns, and the cure time for each layer was set to 9.8 s. The bed height was set to rise by 5 mm and had a hold time of 4 s to allow the resin to self-level effectively. This resulted in around 200 layers and a total print time of approximately 60 minutes.

4.4.2. Digital Light Processing Post-Processing

Post-treatment of the printed part (greenbody) is required before any heat treatment can occur to produce the final ceramic part. This started by cleaning the greenbody of excess resin using Isopropanol Alcohol (IPA) and compressed air. The green body was first submerged in an ultrasonic bath containing IPA for 15 minutes. The sample

was then removed and rinsed further using IPA. Compressed air was then applied to remove any remnants of IPA and dry the sample. The heat treatment of the sample could then begin.

4.4.3. Debinding

There are two significant stages to the heat treatment of a ceramic green body. The first is the burnout of the polymer, and the second is the sintering of the remaining ceramic particles. TGA was used to first determine the optimum temperature at which the polymer decomposed. The results in Figure 43 show the weight of the sample as temperature increased. A drop in weight relates to the pyrolysis of any organic volatile compounds, such as water or polymer, evaporating from the sample. The quicker the burnout of either of these compounds, the more likely the surface of the ceramic is to crack, possibly creating mechanical instabilities. The aim is to reduce the gradient of the line meaning the burnout is more gradual, resulting in surface cracks becoming less likely.

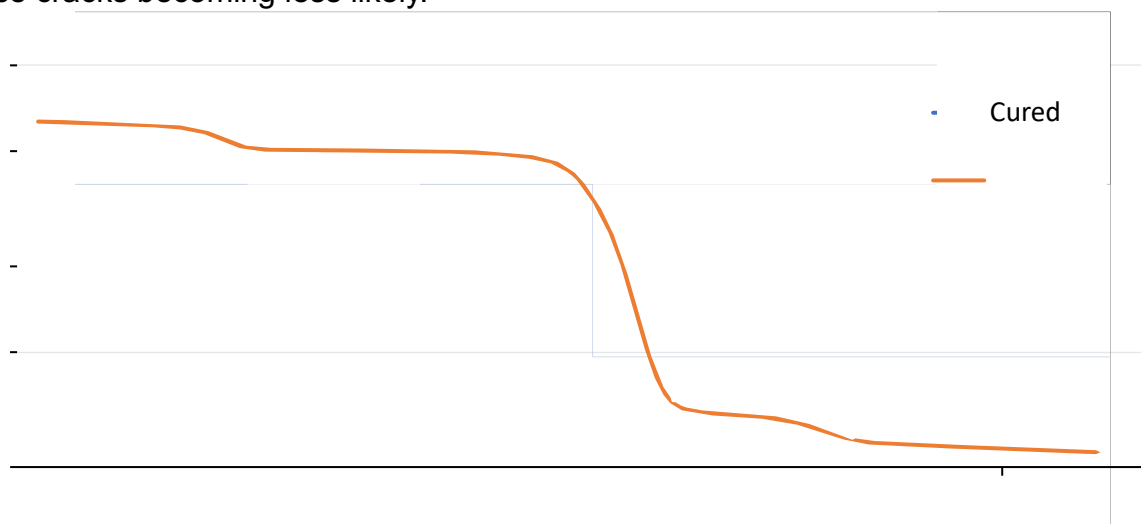


Figure 43: TGA results displaying the weight loss of two samples as temperature increases.

The orange line in Figure 43 relates to a sample subject to TGA straight after the cleaning step. A small 1.5 % drop in sample weight can be seen between 120 - 170

°C, most likely water during the early stages of methyl cellulose thermal decomposition. A small and gradual 2 % change is then seen between 170 and 360 °C. A sudden weight drop of around 40 % is recorded between 360 – 500 °C where most of the polymer is decomposed in a relatively short space of time. The final 6 % of weight loss occurs between 500 – 800 °C.

One way to reduce the rate of decomposition is to further treat the green body using UV light. Exposure to the UV improves the monomer conversion % of the sample creating a stronger cross-linked polymer network which burns out of the sample at a slower rate.²¹⁶ The blue line in Figure 43 represents a sample which has been exposed to UV for 30 minutes in five minute intervals. Compared to the non-UV treated sample, the first 5 % weight drop is recorded more gradually between 0 – 200 °C. After this point, a further weight decrease of approximately 19 % is recorded up to 360 °C, whereas only around 2 % weight drop is recorded for the uncured sample. This could be due to the increase in cross-linking density of the polymer, which is known to influence outgassing and diffusion during debinding.²¹⁷ After 360 °C, there is then a slight decrease in the gradient which stays relatively consistent up to 800 °C with an additional 20 % weight loss recorded. Compared to the uncured sample, the rate of weight loss is much slower, especially at the higher temperature range over 360 °C. Going forward, all samples were subject to UV treatment after the cleaning stage.

4.4.4. Sintering

The second heat treatment stage entailed the sintering of the remaining ceramic particles. The green body was transferred to a Carbolite Gero CWF furnace with a multi-step heating process. Sintering occurred at 1100 °C due to the limitations of the furnace and was held for two hours. Studies have shown that higher temperatures

up to 1375 °C are ideal for the formation of cordierite, but 1100 °C was a high enough temperature to create a solid final product capable of withstanding a washcoat and the testing process.²¹⁸ Figure 44 shows the full temperature profile of the burnout and sintering stage. The full burnout and sintering took around 45 hours resulting in the final ceramic substrate requiring an active catalyst washcoat before testing can commence.

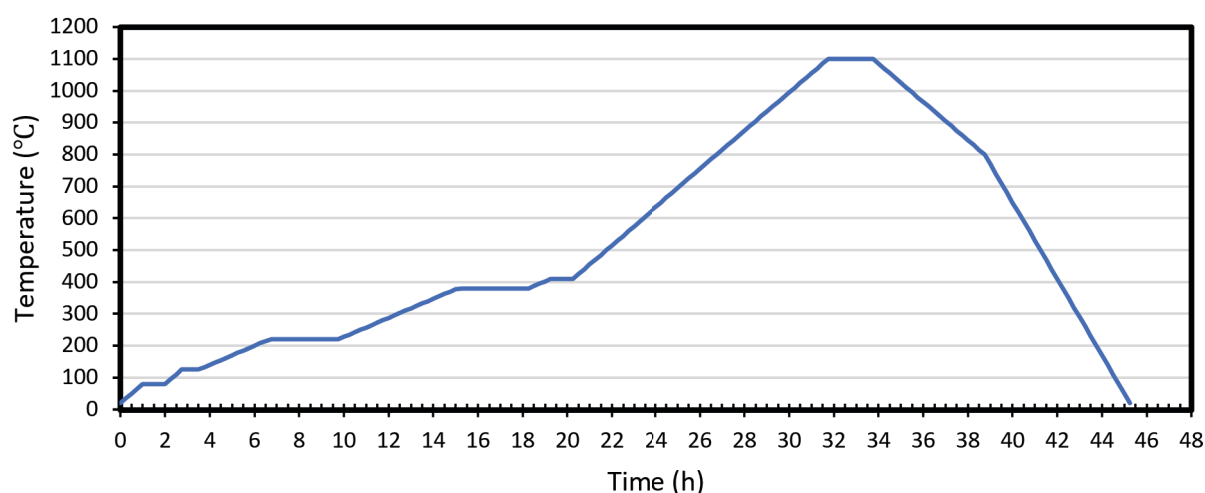


Figure 44: The temperature profile applied to the green body sample.

4.5. Catalyst Preparation

4.5.1. Materials

Ludox SM colloidal silica (30 wt.% water suspension containing sodium stabilising counterion, Sigma-Aldrich) sodium hydroxide (NaOH) pellets (anhydrous, SigmaAldrich). GEO40™ SOL-1030Na colloidal amorphous silica with a 12 nm mean particle size (Geo-12) (30 wt.% water suspension stabilised by sodium hydroxide, Geo 40 Limited) extracted from a geothermal waste fluid. Zeolite Y (Zeolyst International, CBV 720), H form, Si/AL = 30/1. SA=720 m²/g. Palladium (II) chloride (PdCl₂)(Sigma-Aldrich); Sodium (II) tetrachloroplatinate hydrate (Na₂PdCl₄•xH₂O)(Sigma-Aldrich).

4.5.2. Sodalite Synthesis

Sodalite was synthesised starting with an aluminate solution which consisted of 5.00 g sodium hydroxide (NaOH) dissolved in 10.00 g of distilled water (dH₂O), with the gradual addition of 0.54 g of aluminium powder. The mixture was stirred until a clear solution was acquired named Al_{sol}. A silica solution (Si_{sol}) was made by dissolving 9.40 g of NaOH in 16.00 g of dH₂O with the gradual addition of the geothermal silica source (GEO40™) or Ludox which resulted in a thick, white solution which was further mixed with vigorous stirring at 60 °C for 1 hour to obtain a clear silica suspension. A further 10.20 g of dH₂O was added at the same temperature and stirred for 30 minutes. Al_{sol} was then added dropwise to Si_{sol} over ice with vigorous stirring. The crystallisation process was performed in a polypropylene bottle at 60 °C for 47 hours under static conditions. The crystalline product was recovered via centrifuge and washed (until pH~9) before drying at 50 °C overnight and calcining for 4 hours at 550 °C at a 5 °C/min ramp rate to produce the final sodalite zeolite (GeoSOD or Lud-SOD).

4.5.3. Zeolite Precious Metal Loading

Sodalite: 100 mg of palladium (II) chloride (Sigma-Aldrich) and 60 mg of sodium tetrachloroplatinate (II) hydrate (Sigma-Aldrich) were each dissolved in 25 ml of dH₂O before being added dropwise to 3.0 g of the sodalite zeolite under stirring. The catalyst was then left for 2 hours under stirring at 40 °C. Copious amounts of dH₂O were used to wash the sample whilst under vacuum filtration before being left to dry overnight at room temperature. The catalyst was then calcined at 550 °C for 3 hours at a ramp rate of 5 °C/min to give the final catalyst Geo-SOD-PdPt and Lud-SODPdPt.

IW-Zeolite Y: 100 mg of palladium (II) chloride (Sigma-Aldrich) and 60 mg of sodium tetrachloroplatinate (II) hydrate (Sigma-Aldrich) were each dissolved in 25 ml of dH₂O before being added dropwise to 3.0 g of the zeolite Y under stirring. The catalyst was then left for 2 hours under stirring at 40 °C. Copious amounts of dH₂O were used to wash the sample whilst under vacuum filtration before being left to dry overnight at room temperature. The sample was then calcined at 550 °C for 3 hours at a ramp rate of 5 °C/min to give the final catalyst, HY-PdPt-IW.

Vortex-Zeolite Y: A 3.5ml solution of dH₂O, 100 mg of palladium (II) chloride (SigmaAldrich) and 60 mg of sodium tetrachloroplatinate (II) hydrate (Sigma-Aldrich) was added in 50 µL additions to 3.0g of zeolite Y. Between each 50 µL addition, the sample was vortex mixed for 20 minutes at 900 rpm. After the final 50 µL of the solution was added, the sample was vortex mixed for 60 minutes at 900 rpm forming a dough-like ball. The catalyst ball was oven-dried overnight at 80 °C and then crushed using a pestle and mortar. Copious amounts of dH₂O were used to wash the sample whilst under vacuum filtration before being left to dry overnight at room temperature. The powdered sample was then calcined at 550 °C for 3 hours at a ramp rate of 5 °C/min to give the final catalyst, HY-PdPt-VM.

Zeolite Y: 7.2 g of palladium (II) chloride (Sigma-Aldrich) and 4.0 g of sodium tetrachloroplatinate (II) hydrate (Sigma-Aldrich) were each dissolved in 50 ml of dH₂O before being added dropwise to 60.0 g of the zeolite Y under stirring. The catalyst was then left for 2 hours under stirring at 40 °C. Copious amounts of dH₂O were used to wash the sample whilst under vacuum filtration before being left to dry

overnight at room temperature. The sample was then calcined at 550 °C for 3 hours at a ramp rate of 5 °C/min to give the final catalyst, HY-PdPt.

4.6. Catalyst Washcoat

To create the washcoat, 0.05 g of methyl cellulose was added to 10 ml of deionised water. 3.0 g of catalyst was added to this mixture and vortex mixed for 5 minutes to suspend the catalyst within the mixture. The monolith's initial weight was recorded before slowly dipping and withdrawing the monolith into the solution up to three times. Once oven-dried overnight at 70 °C and calcined to remove any organic material at 550 °C for 3 hours at a ramp rate of 5 °C/min, the final weight was recorded. The initial weight was then subtracted to give the catalyst loading weight on the substrate. This was repeated until an approximate 0.2 g washcoat had been achieved.

4.7. Conclusions

To conclude this chapter, a WASP Delta 4070 robocast printer was utilised to manufacture a basic ceramic structure with a simple 90° woodstock pile design using kaolin ceramic powder as a starting material. Further to this, a tailored ceramic resin was produced using a stepwise manufacturing process for the purpose of producing a 3D printed ceramic substrate with a highly complex internal structure. Optimisation of the resin's key components, such as the amount of dispersant, photoinitiator and solid content, was investigated. Although alternative resins have been produced in literature, no resin with a composition like the one produced in this study was found elsewhere specifically utilising cordierite as the ceramic filler. This was an extremely time consuming and difficult part of the research which prevented anything else from progressing until achieved making a key milestone and

achievement of the project. The methodology for printing a green body was then described, along with the full post-treatment required to successfully produce a ceramic body using the resin. This is also believed to be the first time in literature that these unique designs have been constructed into ceramic substrates using DLP technology.

5. Substrate Manufacturing Results

Chapter 5 covers the results of the 3D printed monoliths and catalysts. This begins with the designs produced using CAD technology and a discussion around how the properties vary per design. The characterisation results for each catalyst and both 3D printed prototype substrates are then discussed. Below are the CAD images of the designs constructed, an explanation of how they were produced, and a table listing each design's physical properties.

The designs have been manufactured with the fibres of a standard wood stockpile design modified in the X, Y and Z planes. This results in variations regarding the OFA, CPSI, surface area and the number of exposed faces. Designs can then be tailored to match or improve the properties of a 400 CPSI monolith before comparing the substrates for catalytic performance.

5.1. Designs

The initial design was based on a common woodstock pile structure which was simple to print using the first 3D printer acquired, robocasting. This first design was used as an initial proof of concept for 3D-designed monoliths. Due to how the robocast printer works, the design had to be producible using individual strands or

fibres. The design consisted of stacked fibres with a width of 0.7 mm due to the printing nozzle limitation. It was concluded that this design was the most effective at maximising the substrate surface area within the printer's capabilities. The design is shown in Figure 45.

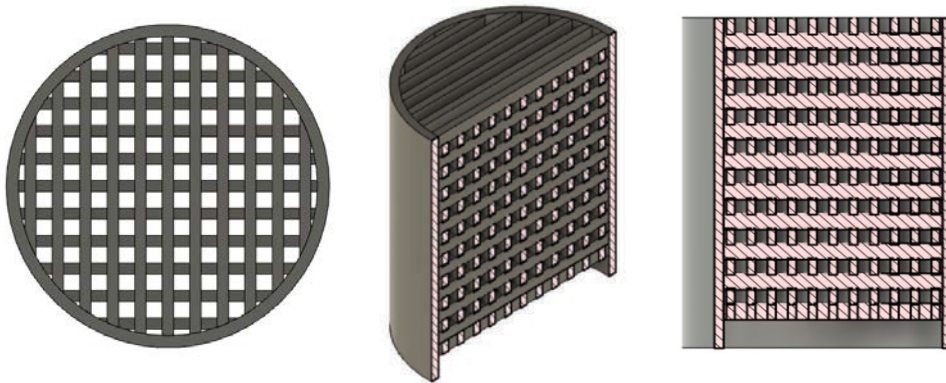


Figure 45: CAD design of a 0.7 mm, 90° woodstock pile monolith.

5.1.1. Digital Light Processing Designs

The DLP printing technique allows a much higher printing resolution concerning wall thickness. A substrate was designed that reduced the fibre width down to the minimum the material was capable of printing. This was concluded at 0.4mm before printing issues arose. The above design in Figure 45 was edited accordingly, producing a woodstock pile design for comparison with the robocast substrate but using a wall thickness of 0.4 mm, reduced from 0.7 mm. This led to an increase in the CPSI from 223 to 330. The number of exposed faces, the OFA and the surface area also improved. Figure 46 below shows the CAD design of the 0.4mm, 90° woodstock pile monolith.

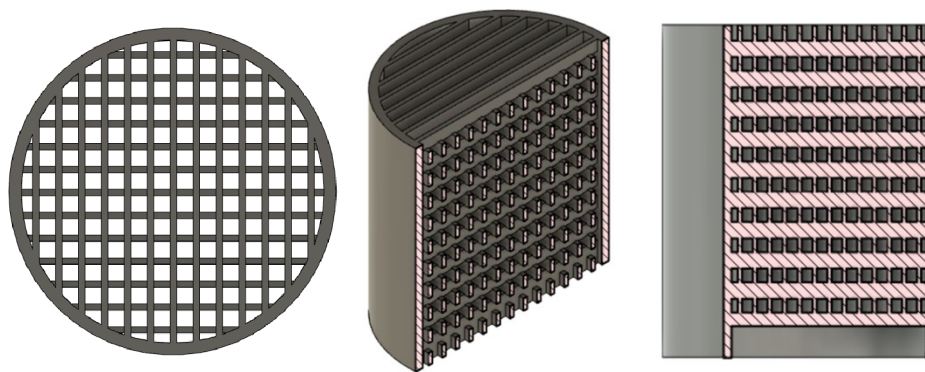


Figure 46: CAD design of a 0.4 mm, 90° woodstock pile monolith.

Other designs were then produced utilising the capabilities of the DLP printing technique. This included introducing features such as overhangs. The use of individual fibres was kept consistent, but the layers of fibres were rotated along different planes – including the X, Y, and Z. This was not possible with the robocast printer as the material used is not self-supporting, meaning overhangs were not possible. A table consisting of the properties of all the designs produced using the DLP printer is listed below. The key properties affecting the catalytic activity of a monolith are included with a more in-depth review of each design category explored below.

Table 6: The physical properties of each DLP monolith design tested.

Design Category	Variation	Surface Area (mm ²)	Number of exposed faces	Open frontal Area (OFA)	CPSI
Fibre Width	0.4 mm	10755	6684	0.58	330
	0.5 mm	10538	5698	0.52	287
	0.6 mm	10133	5313	0.48	252
	0.7 mm	9758	4694	0.44	223
X-Plane Rotation	30°	10505	3868	0.40	331
	45°	10523	4710	0.39	427
	60°	10516	5110	0.36	480
	75°	10587	5102	0.39	413

Y-Plane Rotation	5°	8638	2612	0.39	292
	10°	8858	4224	0.33	292
	15°	7962	4162	0.22	292
	30°	7746	3674	0.00	0
Z-Plane Rotation	7.5°	10458	5942	0.52	287
	10°	10498	5818	0.52	287
	15°	10585	6358	0.52	287
	30°	8827	4486	0.52	287
Commercial	0.4 mm	11712	636	0.58	330
	0.18 mm	15740	870	0.76	400

5.1.1.1. Fibre Width Reduction

The first category of designs to be produced using the DLP printer entailed reducing the width of the individual fibres. This allowed a comparison of the robocast substrate with the DLP substrate using the same fibre width. By decreasing the fibre width, the surface area, the number of exposed faces, the open frontal area (OFA) and CPSI are simultaneously increased. Starting with the 0.7 mm design in Figure 45 and finishing with the 0.4 mm design in Figure 46, the intermediate 0.6 and 0.5 mm structures tested are displayed below in Figures 47 and 48.

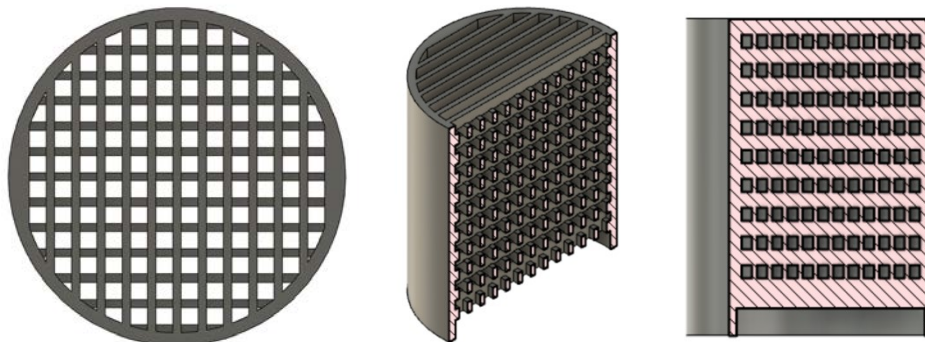


Figure 47: CAD design of a 0.5 mm, 90° woodstock pile monolith.

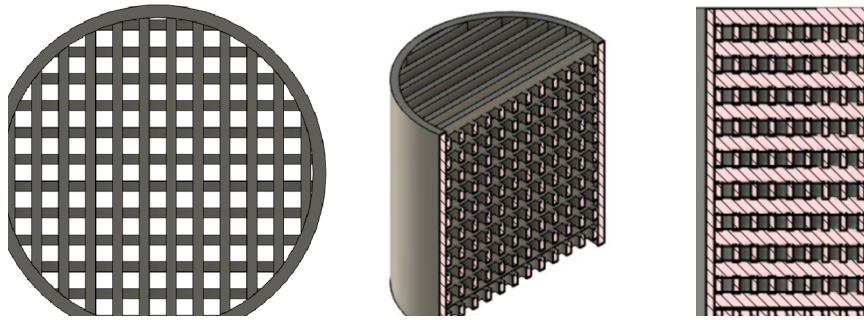
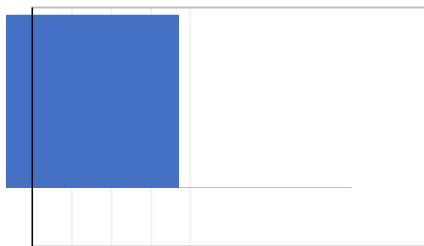
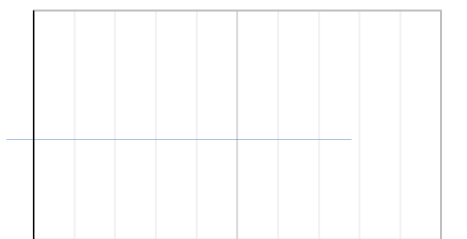


Figure 48: The CAD design of a 0.6 mm, 90° woodstock pile monolith.



9500 10000 10500 11000 0.00 0.20 0.40 0.60

0.80 Surface Area (mm²) Open Frontal Area (OFA)



0 2000 4000 6000 8000

0 100 200 300 400

Number of Exposed Faces

CPSI

Figure 49: A series of graphs comparing the surface area, open frontal area, number of exposed faces and CPSI of 90° woodstock pile designs with a fibre width of 0.4, 0.5, 0.6 and 0.7 mm.

5.1.1.2. X-Plane Variation

The X-plane variation consisted of alternatively rotating each layer of stacked fibres by a set degree in the X-plane. For example, the 60° X-plane substrate started with a layer at 0°, with the second layer being rotated at +60° and the third layer being rotated at -60° to the first layer before the 4th layer was a repeat of the first layer at 0°. For this design set, the CPSI ranges from 331 – 480, albeit with different-sized and shaped channels across each individual design, as seen in Figures 50 - 53. Because of the channel shape variation, a specific comparison for changing the CPSI and catalytic performance in this category is difficult. As for the surface area and OFA, they only differ by 0.77 % and 0.04 respectively, making the changes small compared to the number of exposed faces, which has the greatest variation across the four design categories of 24 %. The small change in the surface area and OFA allow a valuable view into how changing the channel shape and size whilst increasing the number of exposed faces may affect catalytic activity within this design category.

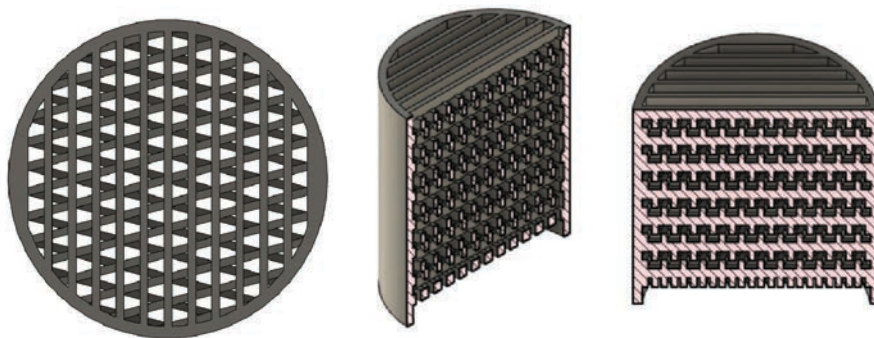


Figure 50: CAD design of a 0.5 mm, 30° fibre rotation in the X-plane monolith.

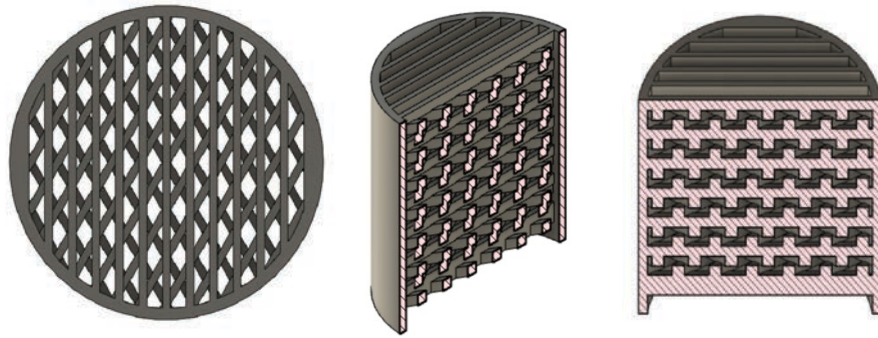


Figure 51: CAD design of a 0.5 mm, 45° fibre rotation in the X-plane monolith.

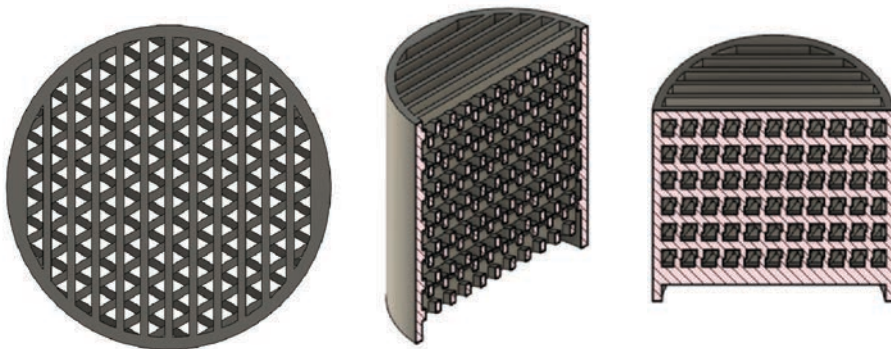


Figure 52: CAD design of a 0.5 mm, 60° fibre rotation in the X-plane monolith.

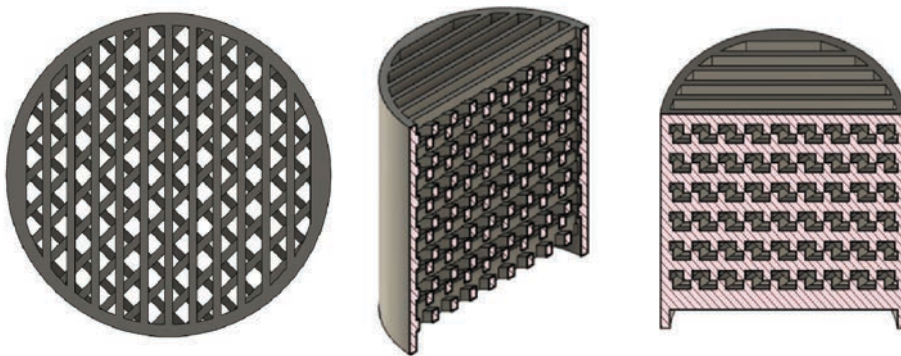


Figure 53: CAD design of a 0.5 mm, 75° fibre rotation in the X-plane monolith.

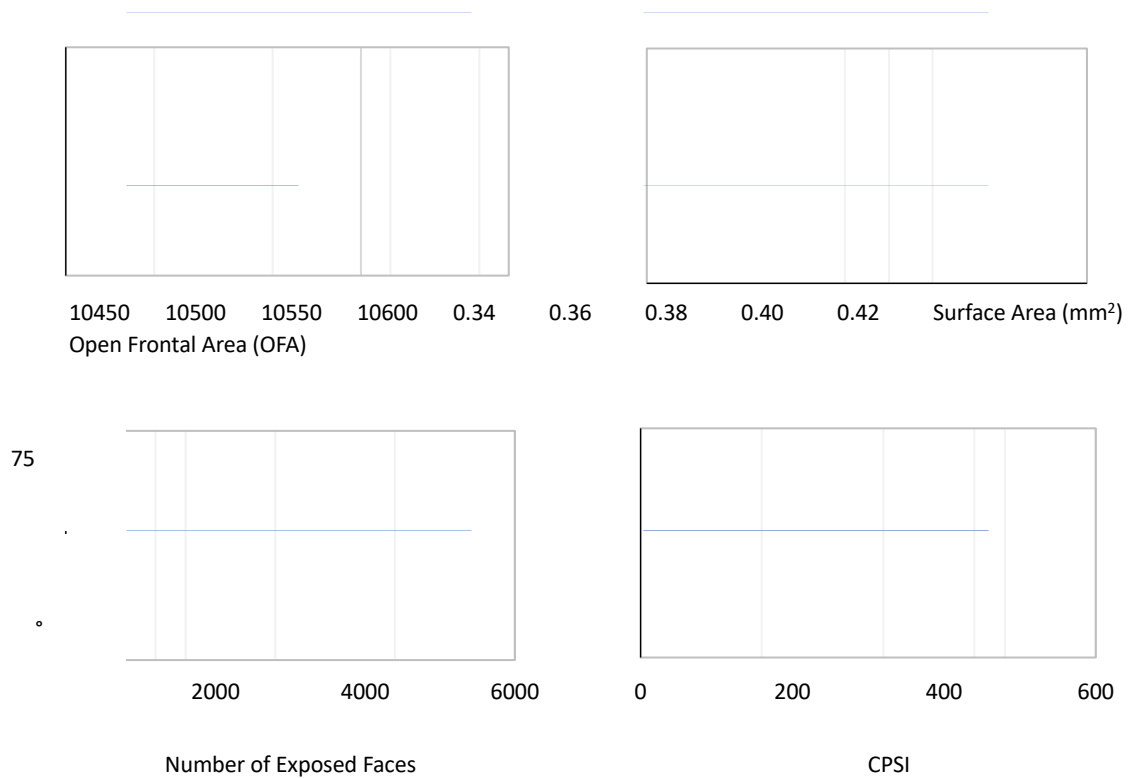


Figure 54: A series of graphs comparing the surface area, open frontal area, number of exposed faces and CPSI of designs with a fibre width of 0.5 mm rotated in the x-plane by 30°, 45°, 60° and 75°.

5.1.2. Y-Plane Variation

The Y-plane variation consisted of rotating the individual fibre layers by a set degree in the Y-plane. Using the 5° Y-plane rotation as an example, the first layer was produced flat to the Y-axis at 0°. The second and third layers were then added at + and – 5° rotation in the Y-plane and stacked on top of the initial layer. This unit was then repeated to build up the monolith, as seen in Figure 55. The result is a set of designs where the open channel width is reduced but with a fixed number of fibres still in the top layer, as seen in the side-on CAD image in Figure 55.

For most of the designs in the Y-plane, CPSI was constant, whilst OFA was reduced by up to 0.39 as the angle increased, more so than any other design category. This means that as the Y-angle increases, more of the frontal area is covered by a catalyst wash-coated surface. The exception is the 30° design which effectively had

no clear channels through the monolith and the lowest surface area of any design tested. Compared to the traditional 90° woodstock pile design, the Y-plane variations had reduced surface areas by 18-28 %. Some of the lowest numbers of exposed faces also belong to Y-plane designs. Especially the 5° variation, which contained the lowest number of exposed faces of any 3D design tested at 2612. Figures 55 – 58 display the CAD designs of all four models tested in the Y-plane rotation design category.

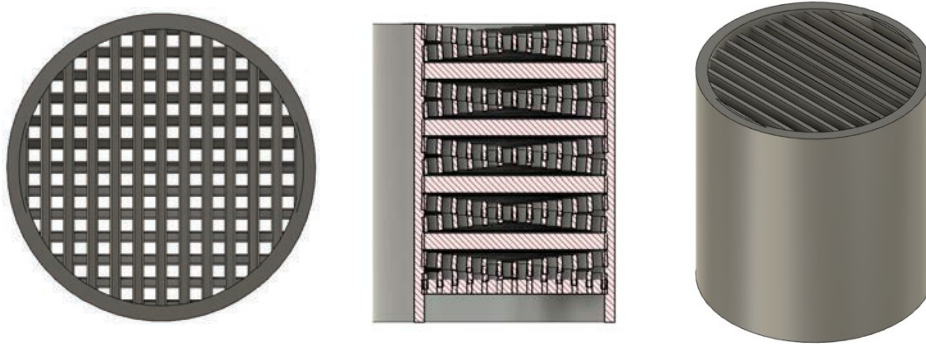


Figure 55: CAD design of a 0.5 mm, 5° fibre rotation in the Y-plane monolith.

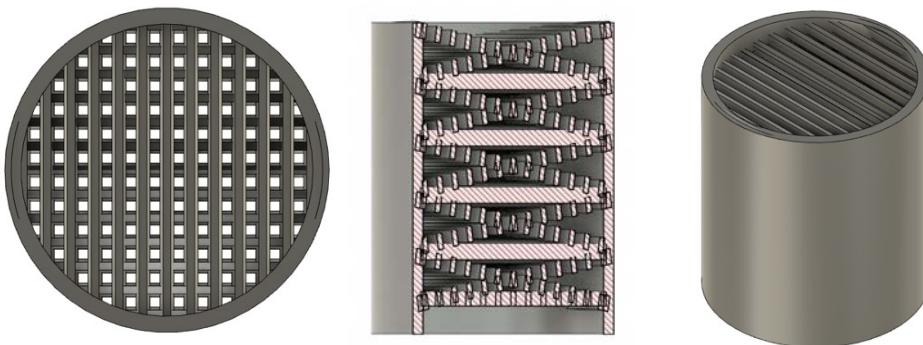


Figure 56: CAD design of a 0.5 mm, 10° fibre rotation in the Y-plane monolith.

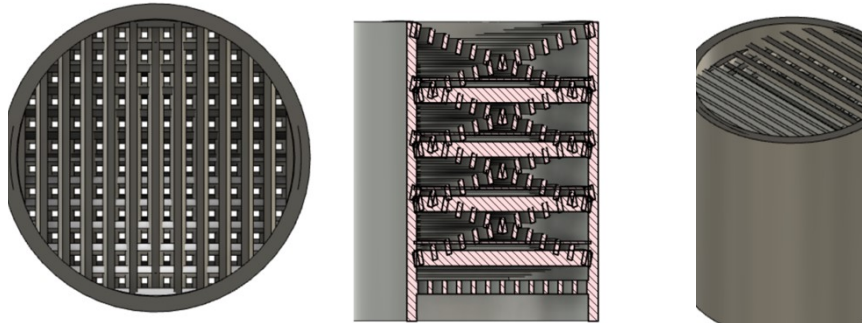


Figure 57: CAD design of a 0.5 mm, 15° fibre rotation in the Y-plane monolith.

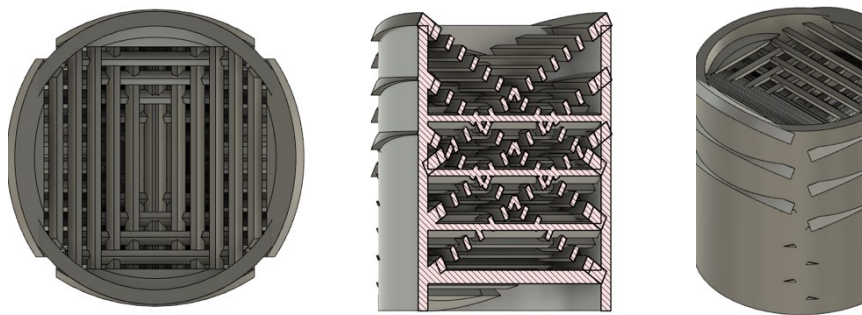
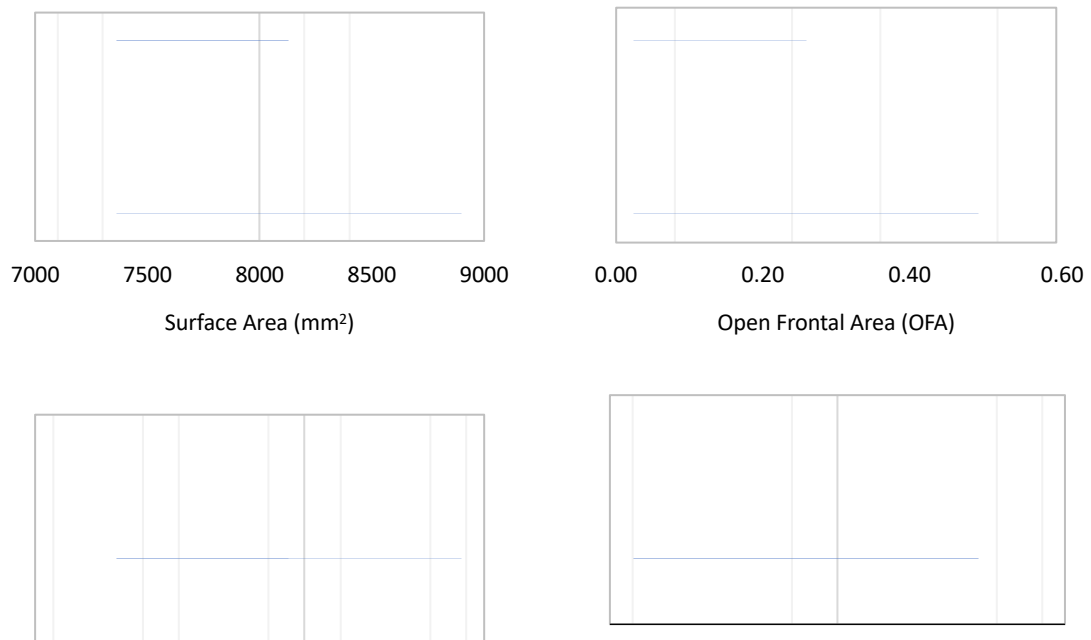


Figure 58: CAD design of a 0.5 mm, 30° fibre rotation in the Y-plane monolith.



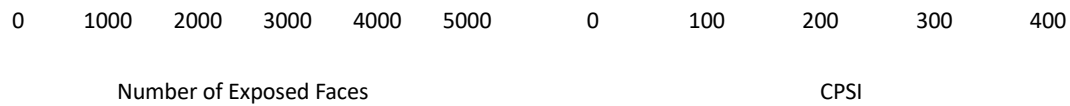


Figure 59: A series of graphs comparing the surface area, open frontal area, number of exposed faces and CPSI of designs with a fibre width of 0.5 mm rotated in the Y-plane by 5°, 10°, 15° and 30°.

5.1.3. Z-Plane Variation

The Z-plane variation consisted of rotating each layer of fibres by a set degree in the Z-plane. Using the Z-axis 10° as an example, the first layer was placed flat on the Z-axis at 0°. The second and third layers were added at + and - 10° and stacked on top of the original first layer. This unit was then repeated, building up the monolith.

As a result, the designs created have a consistent CPSI and OFA, matching that of the traditional 90° wood stockpile structure. This translates to all the Z-axis variations and the 90° wood stockpile having the same cross-sectional pattern in the direction of gas flow, as seen in Figures 60 – 63 and Figure 45. However, the Z-plane variation creates an almost funnel shape directed towards the substrate's centre with small pockets inside the monolith. As the rotation angle increased from 7.5° to 10°, the size of the pockets increase. From 10° to 15°, the size decreases, but the number of pockets increases. At 30°, the surface area and the number of exposed faces decrease by around 16.6 % and 29.4 % respectively but with OFA and CPSI staying constant. This category allows a good insight into the effect of the internal structure when both CPSI and OFA are equal to the straight-channelled commercial monolith. It can be assumed that some improvement in the catalytic performance could be due to the complexity of the internal structure potentially inducing turbulence.



Figure 60: CAD design of a 0.5 mm, 7.5° fibre rotation in the Z-plane monolith.

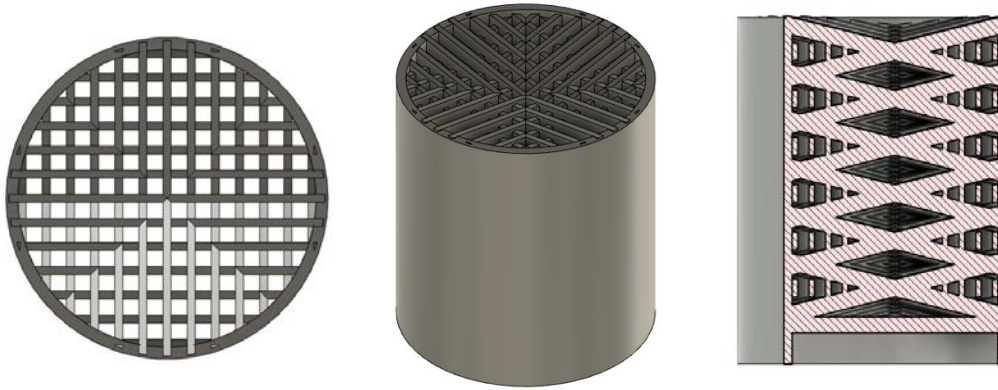


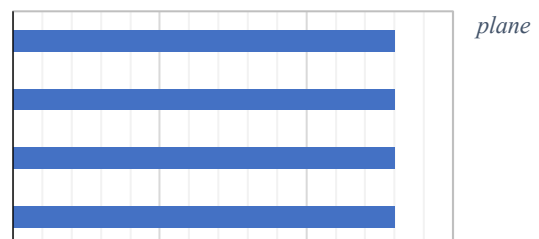
Figure 61: CAD design of a 0.5 mm, 10° fibre rotation in the Z-plane monolith.



Figure 62: CAD design of a 0.5 mm, 15° fibre rotation in the Z-plane monolith.



Figure 63: CAD design of a 0.5 mm, 30° fibre rotation in the Z-plane monolith.



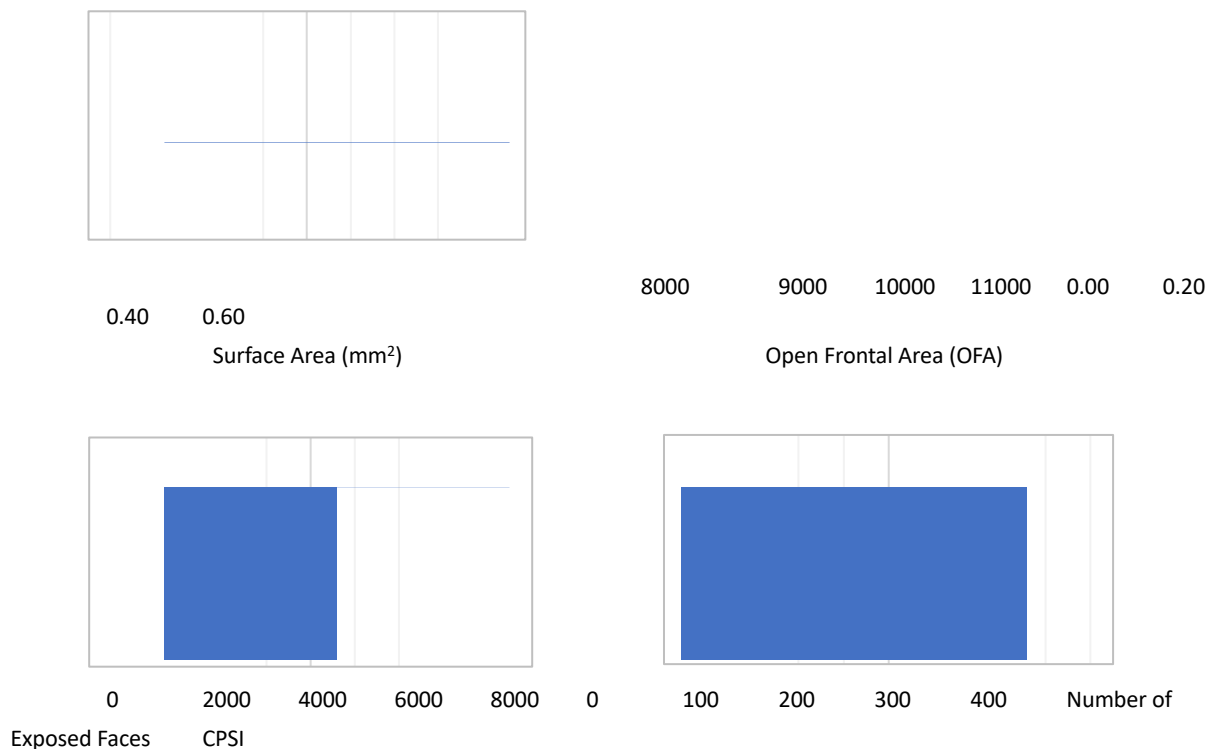


Figure 64: A series of graphs comparing the surface area, open frontal area, number of exposed faces and CPSI of designs with a fibre width of 0.5 mm rotated in the Z-plane by 7.5°, 10°, 15° and 30°.

5.2. Catalyst Results

Table 7 displays the XRF and BET results of the catalysts synthesised. There are some holes in the data where time restrictions and instrument demand limited the ability of what was collected. The loading of each precious metal can be observed after impregnation. The comparison between the GEO (geothermal synthesised sodalite) and LUD (Ludox synthesised zeolite) shows a slight difference in Si/Al ratio. The Geo sodalite zeolite had a Si/Al ratio of 1.29 before impregnation and 1.23 after impregnation. The Lud sodalite zeolite had a Si/Al of 1.26 both before and after impregnation. The difference in the ratio is considered very small, with both sodalite structures being regarded as having a low Si/Al ratio.

Table 7: XRF and BET data from the catalysts tested. (*=company data)

	Al ₂ O ₃ (mass%)	SiO ₂ (mass%)	PdO (mass%)	PtO ₂ (mass%)	Na ₂ O (mass%)	S _{ABET} (m ² /g)	Si/Al
Geo-SOD	32.8	42.2	-	-	24.0	65.7	1.29
Geo-SODPdPt	28.7	35.4	0.98	0.30	24.0	63.9	1.23
Lud-SOD	33.2	41.9	-	-	26.0	175.1	1.26
Lud-SODPdPt	31.8	40.2	0.95	0.28	24.3	51	1.26
ZeoliteY	4.36	94.2	-	-	0.0	720*	21.6
ZeoliteYPdPt-IW	4.68	77.3	1.18	0.48	0.63	-	16.5
ZeoliteY-PdPt-VM	4.71	72.1	1.25	0.79	0.16	-	15.3
ZeoliteYPdPt	2.63	84.8	6.87	2.97	-	-	32.2

The total loading of precious metal for the sodalite was consistent at around 1.2 % of the catalyst total weight. A reduction in the surface area of approximately 124 m²/g to 51 m²/g can be seen in the Ludox sodalite after metal impregnation, implying that the impregnation process negatively impacted the surface area and potential morphology of the zeolite. However, XRD data in Figure 61 shows that the sodalite structure is maintained after precious metal impregnation. There could also have been an error when measuring the initial sample surface area. However, time restraints and limited instrument access prevented a second measurement from being conducted so this surface area reading is reviewed tentatively.

As for the Zeolite Y, a slightly higher Si/Al ratio is reported at 21.6. After the various precious metal loading methods, the ratio changes between the range of 15.3 – 32.2. This shows that each preparation method has a slightly different effect on the zeolite morphology. This includes the precious metal loading, where each loading method resulted in a somewhat different final precious metal loading in the catalyst with the vortex mixed zeolite maintaining a higher final precious metal content.

Platinum tetrammine chloride was selected as the precious metal salt due to its availability in the lab therefore reducing the costs of manufacturing as a limited budget prevented any other alternatives being purchased.

The XRD patterns in Figure 65 confirm the structures of the zeolites. The diffractogram patterns for both the Geo and Lud zeolites are typical of a SOD pattern.²¹⁹ The Ludox synthesised sodalite has a slightly higher intensity than the geothermal sodalite. Ludox is an established material for zeolite preparation implying the geothermal waste material could be a viable alternative as a silica source for zeolite synthesis.



Figure 65: XRD pattern for each zeolite synthesised and tested.

5.3. 3D Printed Substrate Characterisation

5.3.1. Robocast Substrate Characterisation

Figure 66 shows the measurement of the sintered ceramic substrates. The original designs were scaled up to account for the shrinkage during sintering. Shrinkage was measured at around 8 % for the circumference and around 11 % on the Z-axis, which explains the greater height change compared to the circumference. This is common for products produced using robocast printing and has been accounted for

due to a lower concentration of ceramic particles between the individual layers and gravitational effects when sintering occurs.



Figure 66: Images of the printed robocast substrates being measured using a microcaliper .

Figure 67 displays the SEM images of the substrates produced by robocast after thermal post treatment. Image A displays the width of the fibres which after shrinkage is around 680 microns, limited by the printer's nozzle size. Image B shows the channel width which for this print was around 357 microns. Image C illustrates the internal cross-section of the robocast 90° substrates. The individual layers which are stacked to produce the substrate can also be seen. The activity results for the substrates produced are discussed later in the thesis in section 9.5.2.

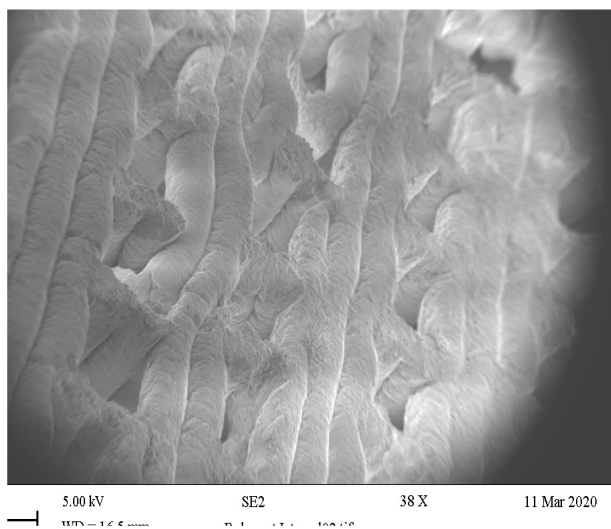
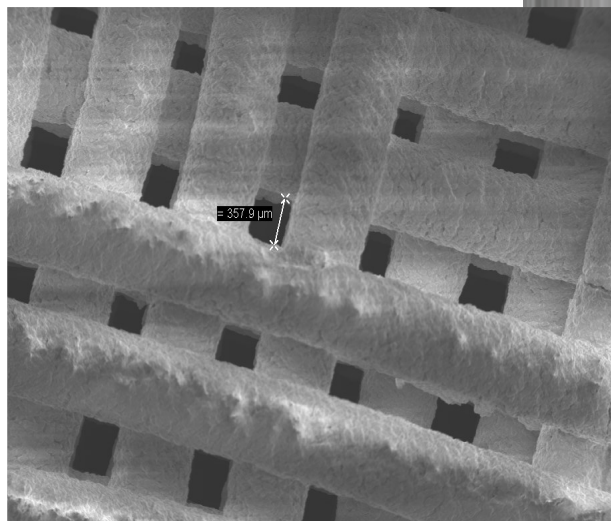
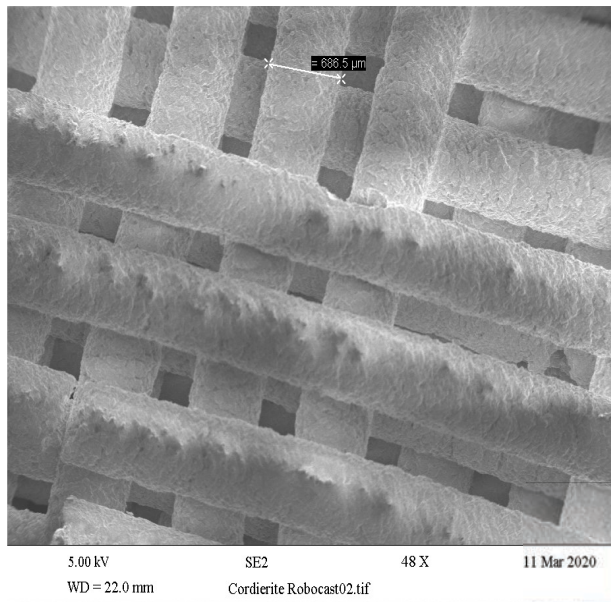


Figure 67: SEM images of the 90° robocast substrate after sintering but before wash coating. A & B=Cross sectional image of the substrate face in the direction of gas flow. C= Internal image of the substrate showing the build of the individual

5.3.2. DLP Substrate Characterisation

Images of the green body and final ceramic substrate produced using DLP technology are shown in Figure 68 below. The height and circumference of the greenbody designs were scaled up to account for shrinkage during the burnout and sintering. The dimensions of the green body and final ceramic substrate were measured using a microcaliper and are shown in Figure 68. The initial dimensions of the greenbody were a height of 23.76 mm and a circumference of 23.36 mm. The height was increased slightly more than the circumference due to the Z axis usually undergoing larger shrinkage during sintering. The final circumference of the DLP ceramic substrate was measured at 19.72 mm, a decrease of around 16 %. The final height was measured at 19.23 mm, an approximate 19 % shrinkage. These shrinkage values are in accordance with those reported in the literature of approximately 15-30 %.^{220, 221} After heat treatment, shrinkage was larger for the DLP substrate compared to the robocast substrate. This is due to being comprised of a larger percentage of organic material when compared to the robocast substrate, meaning there is a larger void to fill during sintering of the model.

Table 8: Dimensions of the 3D substrate printed using the digital light processing technique.

	Pre-Sintering (mm)	Post-Sintering (mm)	Shrinkage (%)
Circumference	23.36	19.72	15.6
Height	23.76	19.23	19.1

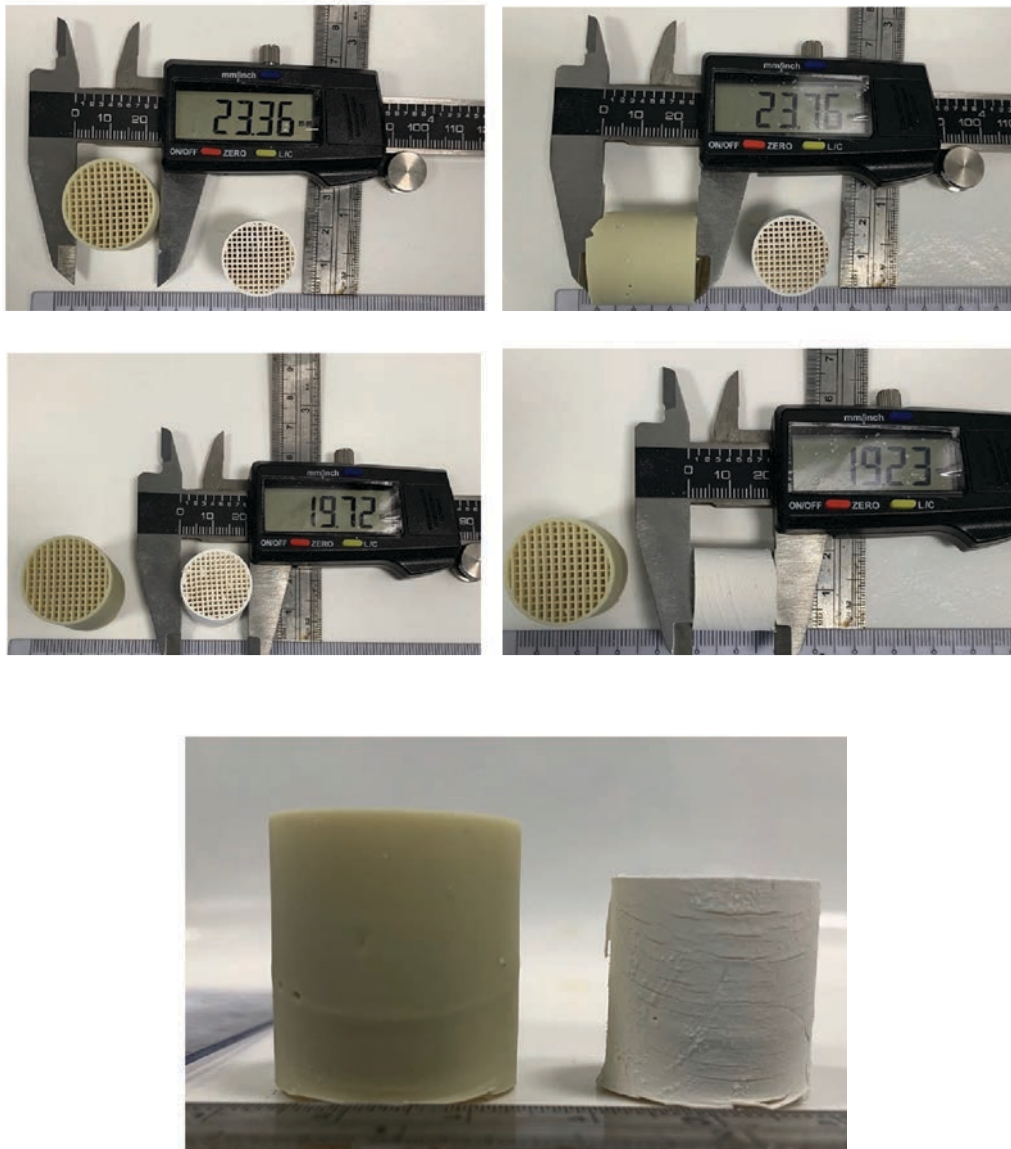


Figure 68: A-D: Images of the green body and ceramic substrate produced using DLP technology being measured using a microcaliper. E: A side image of both the green body before and after heat treatment.

Figure 69 below displays SEM images of the 90° woodstock pile DLP greenbody.

Image A shows an individual fibre which has been measured at 501 μm . The individual fibres were not scaled up, unlike the circumference and height, as shrinkage was an opportunity to increase the CPSI. Image B displays a cross-sectional image of the greenbody showing the various channels of the substrate. Image C displays the internal cross section of the monolith which displays the individual layers used to build up the design. The layer thickness was measured as 1.096 mm.

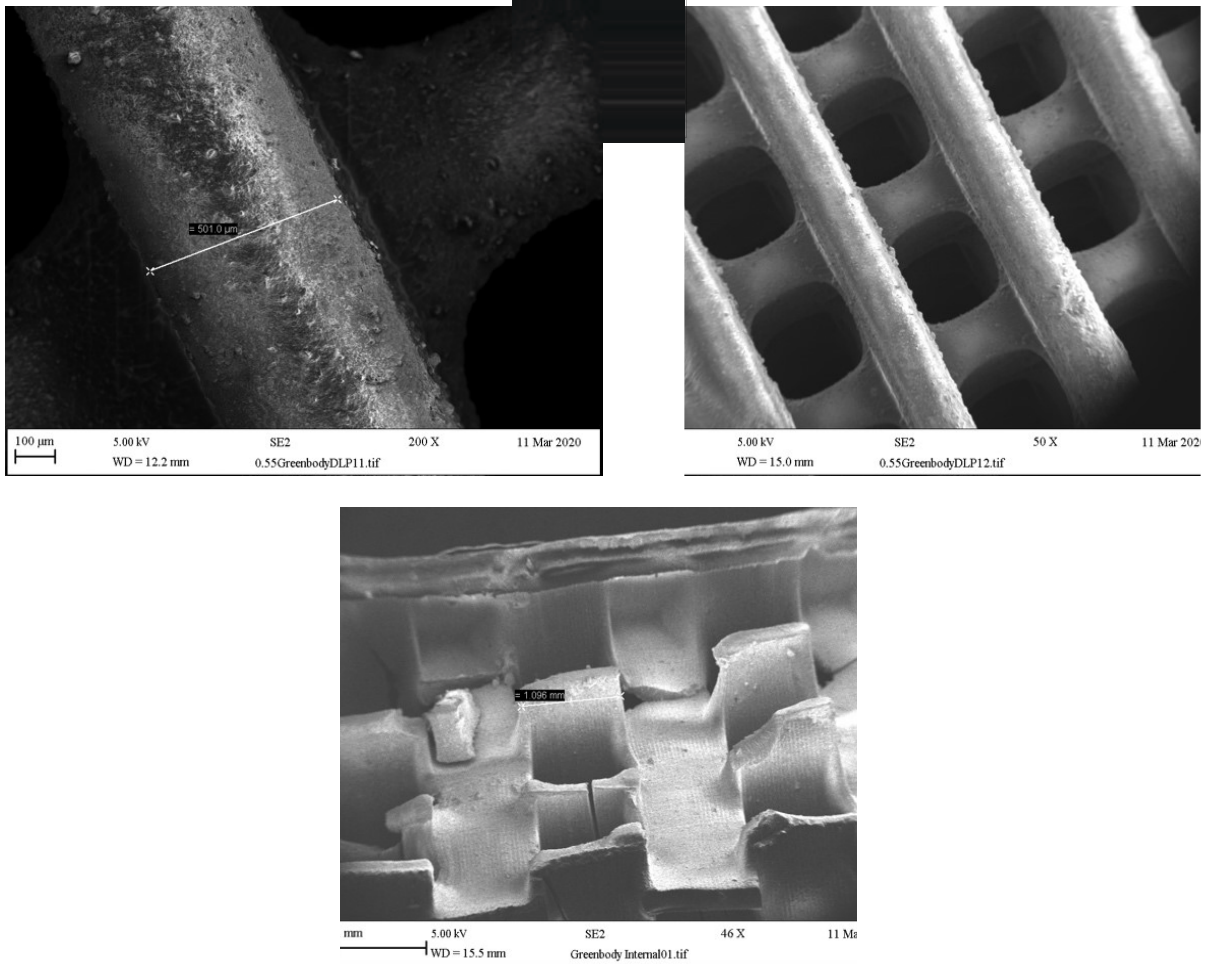


Figure 69: SEM images of the DLP substrate. A: An image of the individual horizontal fibre. B: An image of the crosssection of the substrate. C: An image of the internal cross-section showing the individual layers used to build up the monolith.

Further SEM images were taken after the green body had been subject to the heat treatment process. The images are displayed in Figure 70 below. Slight cracks can be seen on the surface of the substrate, which is to be expected. This is a result of the gaseous compounds escaping from inside the substrate via the surface. The width of the individual fibre was measured at 342.8 µm, a decrease of around 31 %.

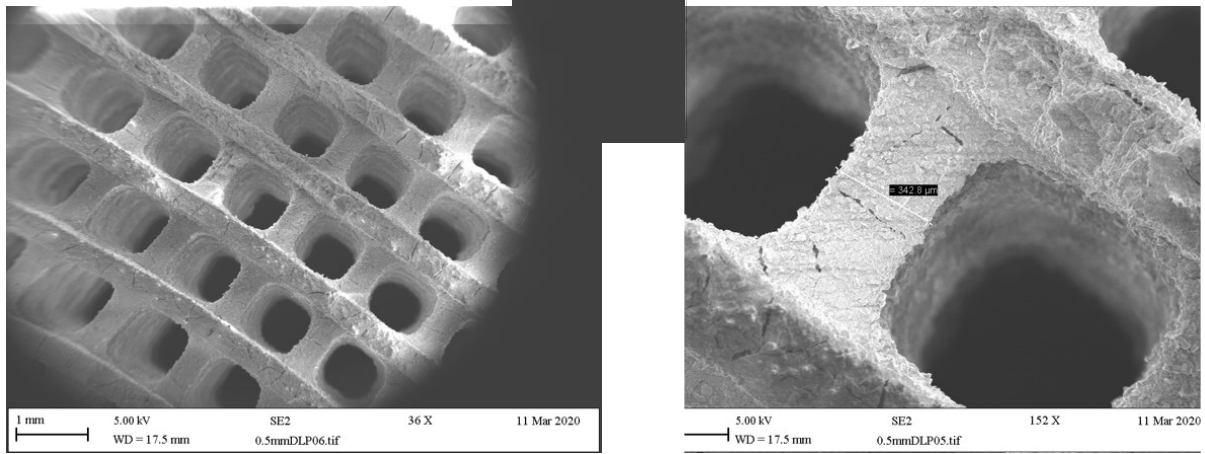


Figure 70: SEM images of the ceramic substrate produced using DLP technology. A: An image of the cross-section of the substrate. B: An image of an individual horizontal fibre.

Figure 71 below shows an SEM image of a DLP substrate with the washcoat applied. The catalyst washcoat can be seen on the surface of the substrate.

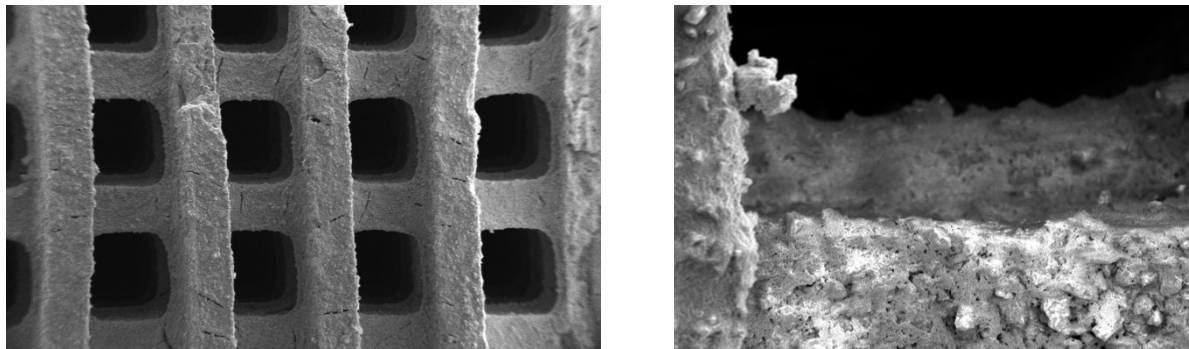


Figure 71: Image of a 0.5mm 90° wood stockpile design after the catalyst washcoat has been applied.

5.3.3. Conclusions

Autodesk Fusion 360 was then employed to produce various monolith designs which could be printed using Robocast or DLP 3D printing methods. An initial 90° wood stockpile design was produced before a further 15 designs were created, by rotating the same fibres used to construct the wood stockpile design in each of the X, Y and Z planes. CPSI, OFA, the number of exposed faces and the surface area were all measured using the CAD software. The properties of these designs were compared as the rotation angle increased through each design category.

Several catalysts were successfully synthesised for the purpose of completely oxidising methane. Sodalite was successfully synthesised using a geothermal waste product as a silica source resulting in a comparable zeolite to when using a wellknown reagent, Ludox. Two methods were then explored for precious metal application including an incipient wetness technique and a vortex mixing method. Both provided a successful method for the addition of platinum and palladium to a zeolite support.

Characterisation of the ceramic substrates and catalysts synthesised was discussed with techniques used including XRF, XRD and SEM imaging to confirm the catalysts compositions. The robocast substrate was confirmed to have a shrinkage of around 8 %. The DLP substrate had a recorded shrinkage of around 31 % which resulted in a substrate with a fibre width of around 342 μm . These results were then utilised to help produce active catalytic substrates for the purpose of methane oxidation which is discussed in greater detail in chapter 6.

6. Catalyst Activity Testing

Chapter 6 covers the catalytic testing aspect of this thesis. This helps to answer the ultimate aim of this thesis which is to try and reduce the amount of methane produced from an emissions stream. The testing protocol is explained, and the testing system used is shown. The substrates were then broken down into categories to help compare the effects of different designs. A commercial substrate having undergone the same catalyst wash coating process is included for comparison to a traditional monolith system. All tests were conducted three times with an average reading taken, unless stated otherwise.

6.1. Catalyst Testing Methodology

6.1.1. Testing Rig

The catalytic activity of each sample was studied in a steel tube fixed bed reactor positioned inside a temperature-controlled furnace (Vecstar type VCTF5, CAL Controls Ltd, CAL9500, CAL3300). Each substrate was loaded into the steel tube (20 mm internal diameter, 1 mm thickness, 20 mm length) between two glass wool plugs and wrapped in foil. A 50 mL/min feed mixture comprising He:O₂, equal to 4:1, was used to pre-treat all substrates. The feed mixture was then altered to 100 mL/min comprising of He:O₂:CH₄, equal to 85:10:5 for catalytic testing. All gases were supplied via main gas lines, and each flow was maintained using Bronkhorst UK GF40 Series mass flow controllers. The reaction products were measured by an Agilent 7890B series gas chromatograph equipped with a Carboxen 1006 Plot fused silica capillary column (30 m x 0.53 mm) connected via a 6-way gas sampling valve to a thermal conductivity detector. Measurements were recorded at 25 °C intervals (after holding the temperature for 10 minutes) starting at 200 °C using a ramp rate of 10 °C/min. Conversion was calculated using equation 10:

$$\text{Conversion} = \frac{\text{Inlet} - \text{Outlet}}{\text{Inlet}} \times 100\%$$

(Eqn 10)

Figure 72 shows an image and a schematic of the Mark 2 testing rig.

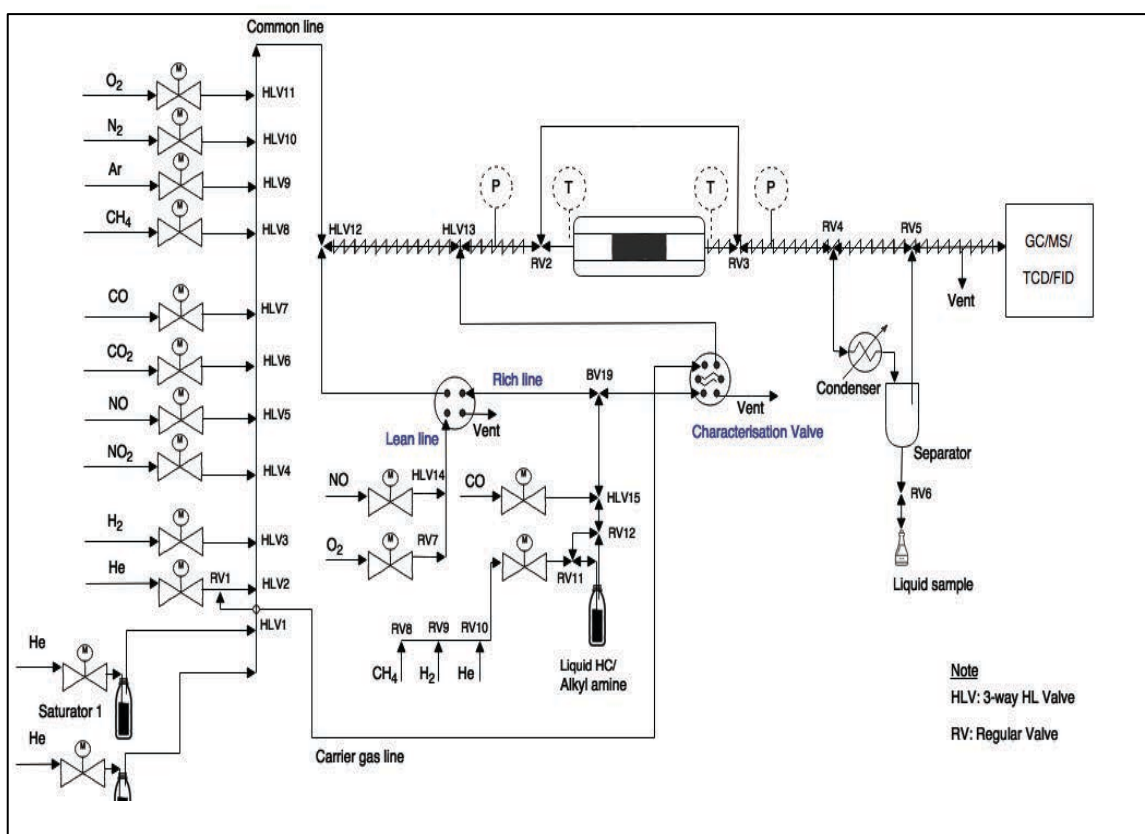


Figure 72: A photograph(top) and schematic(bottom) of the testing rig.

6.1.2. Gaseous Reactant Calibration Curve

The calibration curves for the Mark 2 testing rig were assembled by injecting a known amount of gas through the GC and measuring the peak area produced by the

TCD detector. By injecting a known concentration of gas, the raw TCD signals could then be used to convert future TCD signals to gas concentration measurements during catalytic testing.

Figures 73, 74 and 75 below show the graphical representation of the gas flow sent through the GC column and the corresponding response factor for CH₄, O₂ and CO₂. The regression line was taken from the plotted points, and the equation of the line was used to calculate the concentration of each gas which was present during catalytic testing using the area produced by the TCD detector. During low CH₄ concentration, CO₂ was utilised to assess the conversion of CH₄ by how much CO₂ had been produced.

Flow rates below 5.0 % (5.0 mL/min) were avoided due to both a higher chance of error from the mass flow controllers and the experimental conditions not requiring such low values.

6.1.2.1. Methane

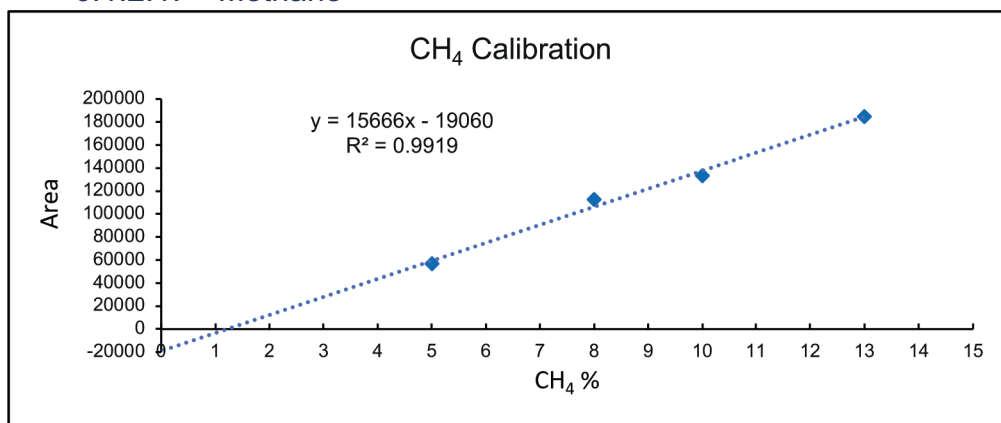


Figure 73: Calibration curve for methane.

6.1.2.2. Carbon Dioxide

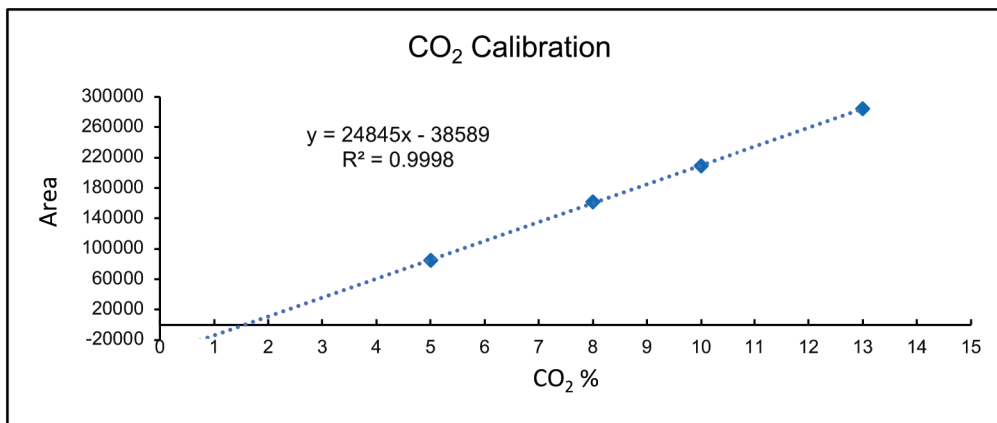


Figure 74: Calibration curve for carbon dioxide

6.1.2.3. Oxygen

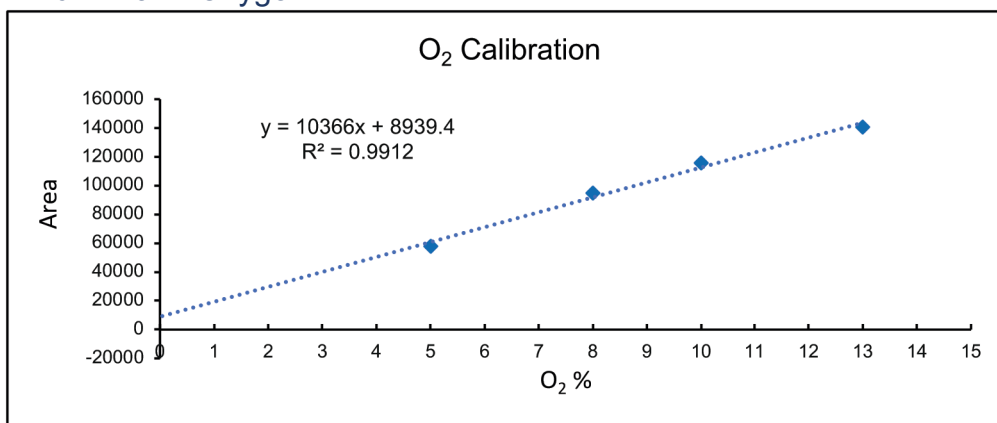


Figure 75: Calibration curve for oxygen.

6.2. Powder Catalyst Testing Results

Figure 76 displays the light-off curves for each of the five catalysts synthesised in section 8.4. All the catalysts synthesised were active for the complete oxidation of methane but at varying levels. Unsurprisingly, ZeoliteY-PdPt, loaded with around 10 % precious metal is the most active catalyst. This catalyst had the highest percentage conversion of methane at each temperature. However, the remaining four catalysts show an interesting pattern across the temperature range. In the lower temperature range between 240 – 350 °C, the best-performing sodalite catalyst is Lud-SOD-PdPt and the best zeolite-performing catalyst is HY-PdPt-VM. At the maximum temperature of 510 °C, all HY zeolites outperform the sodalite catalysts.

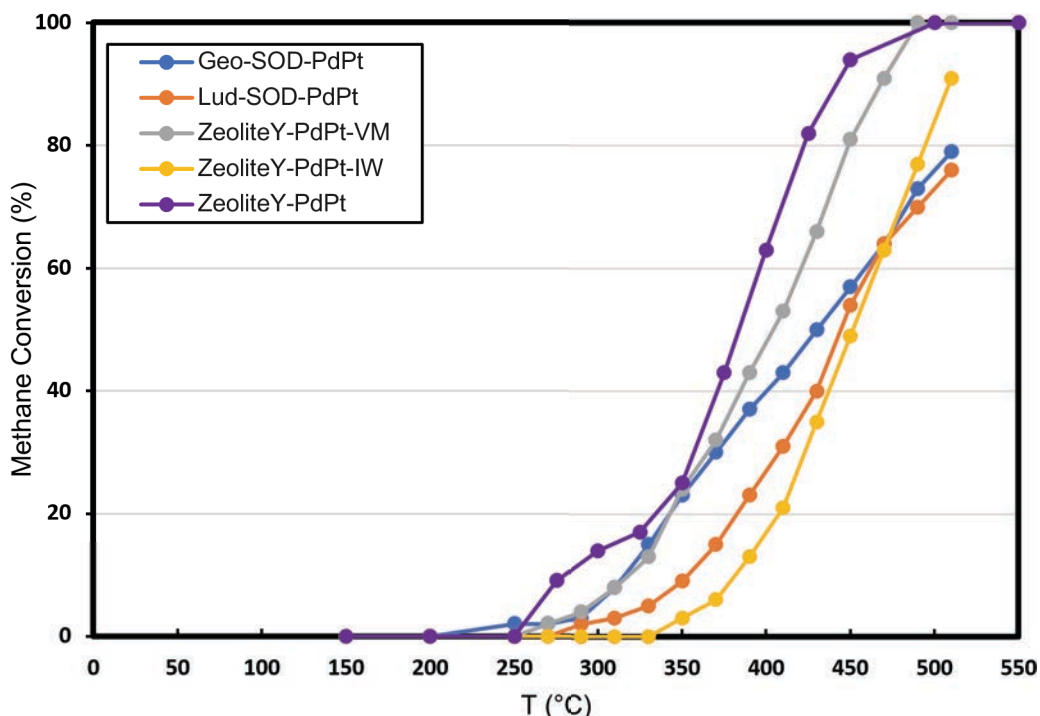


Figure 76: Light-off curve for each catalyst synthesised. Flow Rate = 100ml/min. Gas Composition: He= 85 %, O₂=10 %, CH₄=5 %.

Comparing the sodalite catalysts, the Ludox-synthesised sodalite has slightly better methane conversion at lower temperatures. However, by the higher temperature of 450 - 510 °C, the difference in conversion is a maximum of 3 %, implying a more consistent reactivity between the two sodalites at the higher temperature range. Both sodalite catalysts had a very similar precious metal loading, so it can be assumed that the difference in reactivity is most likely caused by the arrangement of the active sites and not the metal content. Using a different reactant during the sodalite synthesis could influence how the active sites and precious metals arrange themselves on the surface. However, further investigation would be required to confirm this.

Comparing both Y zeolite catalysts, the effect that the method for precious metal application can have on activity is much clearer. The vortex mixed catalyst displays a higher methane conversion across the entire temperature range whilst simultaneously achieving a much higher final conversion of 100 % compared to 91 % for the incipient wetness technique. These results align with a study by Banerjee et al. They compared the effect of vortex mixing and incipient wetness synthesis of a

Pd-Al₂O₃ catalyst for the purpose of complete methane oxidation.²²² The vortex mixing method produced precious metal particles with a slightly smaller diameter which was linked to higher activity at lower temperatures. The difference between their activity reduced as the temperature increased over 450 °C which is in line with the results in this study. However, this precious metal loading technique is much harder to replicate for larger volumes of catalysts.

The most active catalyst was the ZeoliteY-PdPt with a 10 wt.% precious metal loading. Due to being the most active, this catalyst was selected for the wash coating of the substrates. To understand the effect of using different samples of the same batch-synthesised catalyst, five samples were taken from the same batch, and each underwent a full methane activity study using the catalyst testing rig. The light-off curves are displayed in Figure 77. There is a slight spread in the results but the lightoff curves were consistent, producing the same shape and achieving over 90 % conversion at roughly the same temperature, just above 425 °C. Activation of all the samples occurred between 275 – 300 °C, with the majority occurring at the latter. A study by A. Doyle and L. Tosheva used the same gas composition with a lower total flow rate of 50 ml/min and achieved activation temperatures of around 250 °C for Pdloaded faujasite catalysts. No glass beads were used to support the catalyst, which could have created localised hot spots within the catalyst sample, which may account for the lower activation temperature. Additionally, the lower flow rate increases the reactant contact time with the catalyst resulting in an improved performance but generally, the catalyst samples performed similarly.²²³ A second publication by A. Doyle and J. Kamieniak used the same testing conditions again but using Pd-hydroxyapatite catalysts with a similar precious metal loading of around 10 %. There was no significant reactivity recorded above 450 °C. This is around 100 150 °C higher than the Pd-zeolite samples in this study shown in Figure 76. The

surface area was only averaging around 40 m²/g for the hydroxyapatite catalysts, which is approximately 680 m²/g lower than the Y zeolite and 20 m²/g lower than the sodalite zeolite, which could account for the lower activity.²²⁴

Due to the nature of synthesising catalysts, it is difficult to produce exact regularity per catalyst sample, meaning there will almost always be a slight difference between the activity of samples. For this reason, one large batch was synthesised in the hope of reducing any synthesising differences as much as possible.

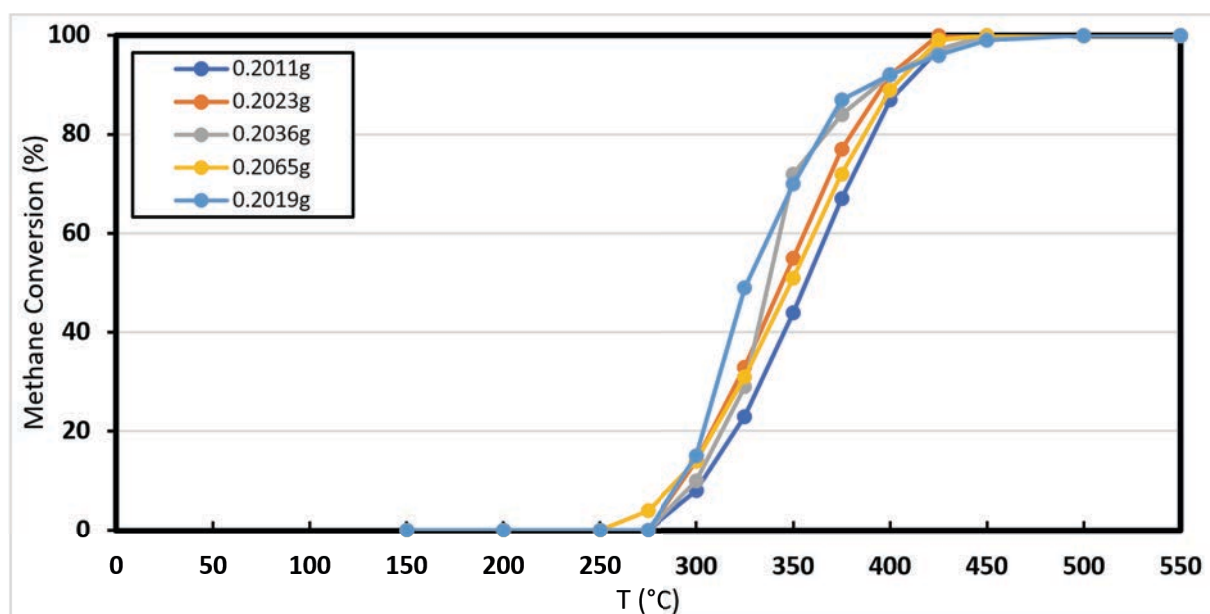


Figure 77: Light-off curves for five individual samples of the HY-PdPt batch catalyst synthesised. Flow Rate = 100ml/min. Gas Composition: He= 85 %, O₂=10 %, CH₄=5 %.

6.2.1. Substrate Testing Conditions

The washcoat applied to each substrate weighed approximately 0.2 g ± 0.005 g. The variation was due to the difficulty of reproducibility in the wash-coating method, a common issue when dip-coating monoliths.²²⁵ Each monolith design was printed and tested once unless stated otherwise. The methane conversion was measured three times at every temperature, and an average was calculated to obtain a conversion result for each individual temperature.

6.3. Substrate Activity Results

6.3.1. DLP Fibre Width

The first set of testing results consisted of reducing the fibre width of the monoliths. This was partly to find the lower limit capable of being printed whilst simultaneously allowing a study to further understand the effect that reducing a monolith's fibre width has on catalytic activity. As seen in section 6.4.2.1., these designs consisted of a 90° woodstock pile design with the fibre width labelled in the graph's key. Table 8 displays the properties of the designs tested in this category. At the lower temperature range, the monoliths all reacted very similarly. The $T_{10\%}$ value is the same for all four designs. There is an almost unrecognisable change of only 3 % in methane conversion up to around 400 °C. Over 400 °C, as the fibre width reduced, methane conversion increased more significantly. At the maximum temperature of 550 °C, the highest conversion was recorded using the 0.4 mm substrate, achieving a conversion of 89 %. In comparison, the lowest recorded methane conversion at this temperature was achieved using the 0.7 mm monolith, at which maximum conversion was recorded as 74 %, a difference of 15 %. One reason for the decline in the performance of the 0.6 and 0.7 mm substrates could be due to the application of the washcoat. Each substrate underwent the same washcoat process described in section 9.4. As the CPSI of a substrate decreases, the surface area also decreases. This change is most significant from the 0.5 mm to the 0.6 mm substrate. Since the catalyst loading was the same, this resulted in the washcoat thickness increasing. If the washcoat is too thick, even with a sufficient number of catalytic active sites, not all the sites are necessarily accessible, which results in reduced activity.^{226, 227}

Although the maximum conversion was achieved with the 0.4 mm substrate, when attempting to print more complex internal geometries, the structure's mechanical integrity became slightly compromised, so a fibre width of 0.5 mm was selected for future studies. This was also decided since there was only a slight decrease in

performance between the 0.5 and 0.4 mm monoliths, with the largest difference being a 5 % conversion at 450 °C.

Table 9: Properties of the substrates designed with a reduced fibre width.

	T _{10%} (°C)	T _{50%} (°C)	T _{50%} - T _{10%} (°C)	Surface (mm ²) 10755 Area	Number of Exposed Faces	Open Frontal Area	CPSI
0.4 mm	338	459	121		6684	0.58	330
0.5 mm	338	469	131	10538	5698	0.52	287
0.6 mm	338	503	165	10133	5313	0.48	252
0.7 mm	338	482	144	9758	4694	0.44	223

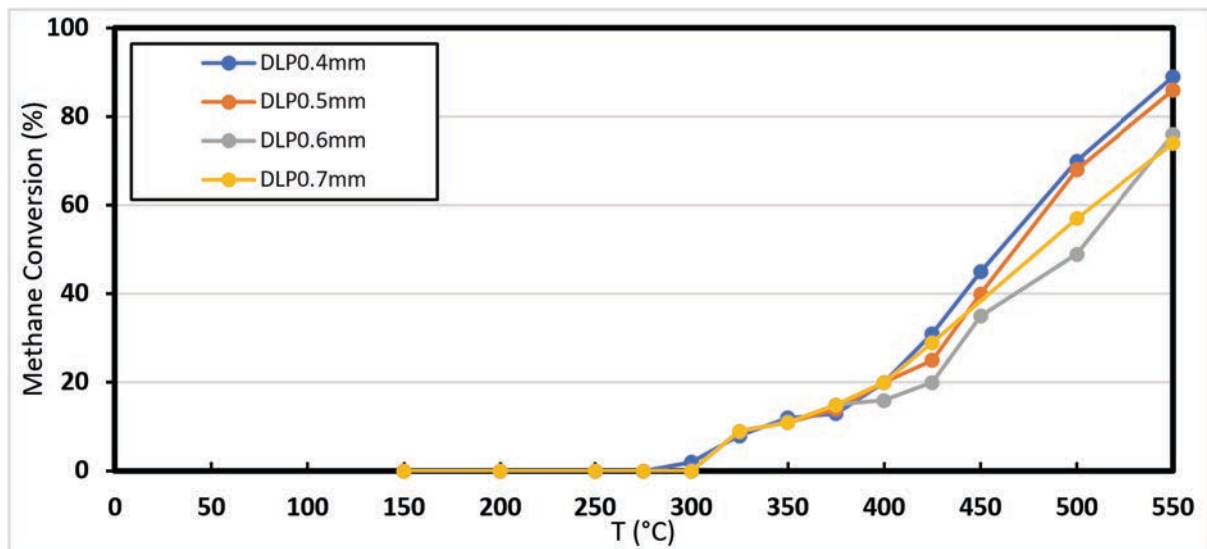


Figure 78: Light-off curve for 90° wood stockpile design, DLP printed substrates with a reducing fibre width. Flow Rate = 100ml/min. Gas Composition: He= 85%, O₂=10%, CH₄=5%.

6.3.2. X-Axis Variation

The next set of substrates tested included those with a variation in the X-axis rotation angle. These designs were capable of being produced using both robocast printing and DLP printing which allowed a useful comparison of the two printing techniques. The light-off curves for the DLP-printed and robocast-printed substrates are displayed in Figure 79 and Figure 80 respectively. Generally, the DLP substrates performed better than the robocast-printed substrates. However, their behaviour over the full temperature range displays interesting results. The robocast substrates were activated at a lower temperature than the DLP substrates. The DLP substrates were

consistently activated at 350 °C but with some variation in the activation conversion percentage, a range of 9 % across the DLP prints. The robocast substrates were activated over a larger temperature range starting at 300 °C but mostly at 325 °C. The lower activation temperature could potentially be accounted for by the lower OFA when compared to the DLP prints. The larger fibre width results in a larger initial contact surface, making it more likely for the incoming gas flow to encounter the catalyst and react, hence improving conversion.

As the temperature of the reaction increased, the DLP substrates displayed a greater improvement in conversion, more so at the higher temperature range above 500 °C.

At the highest temperature of 550 °C, the average conversion for the DLP substrates is 95 % compared to only 82 % for the robocast substrates. The range of conversion between both sets of samples was consistent at 10 %. Once activation had been achieved and the temperature surpassed 400 °C, the DLP substrates consistently achieved greater methane conversion, which could be accountable to the higher internal surface area and CPSI compared to the robocast samples.

Regarding the individual rotation in angle, there are consistencies across the two printing styles. The best-performing angle rotation was 75°. The 75° substrates achieved the highest final conversion percentage across both printing styles, achieving a maximum of 100 % for the DLP printed substrate at 550 °C. This may be related to the fact that the 75° substrate has the largest surface area in this group of substrates by 49 mm². The substrate which activated last for both sets of substrates is the 90° rotation. This could be rationalised by the fact it has the largest OFA of 0.52 compared to the next closest, 0.40, which belongs to the 30° substrate. A larger OFA means a smaller initial contact surface for the reactant gases to initially react, potentially reducing initial activity. The 90° substrate also has the lowest CPSI.

However, this is difficult to directly assign to the reason for the lower activity due to the variation in channel shape and size. These results offer insight into the improvement DLP printing can offer compared to robocast printing. The remaining designs tested were all printed using DLP technology after this discovery.

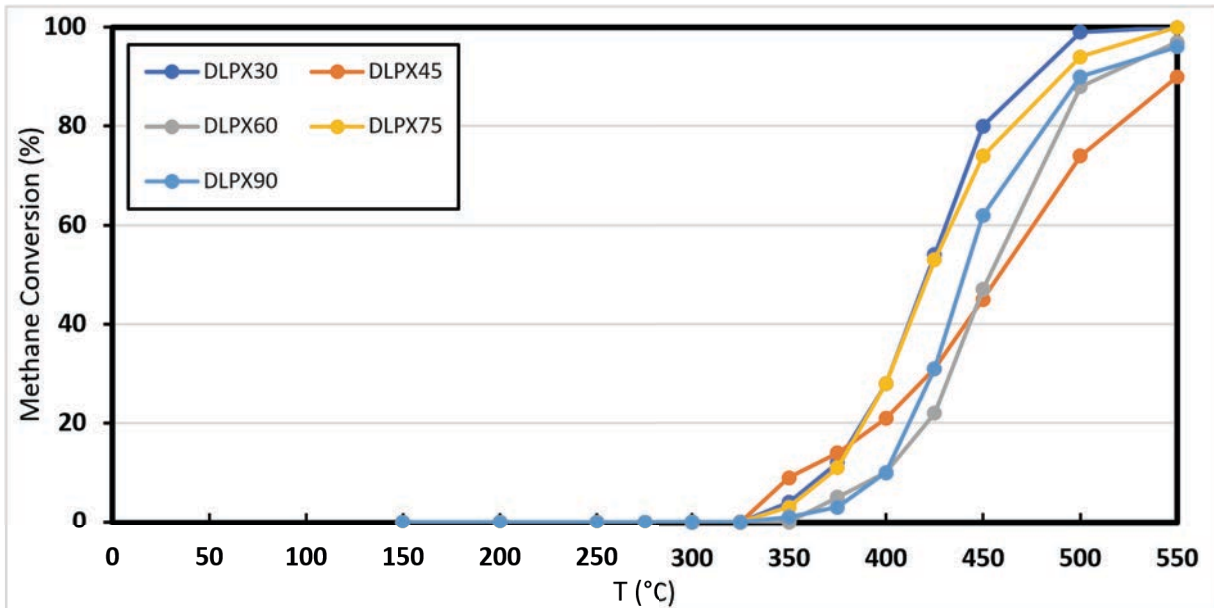


Figure 79: Light-off curve for DLP printed substrates with 0.5mm wide fibres rotated along the X-axis. Flow Rate = 100 ml/min. Gas Composition: He= 85 %, O₂=10 %, CH₄=5 %.

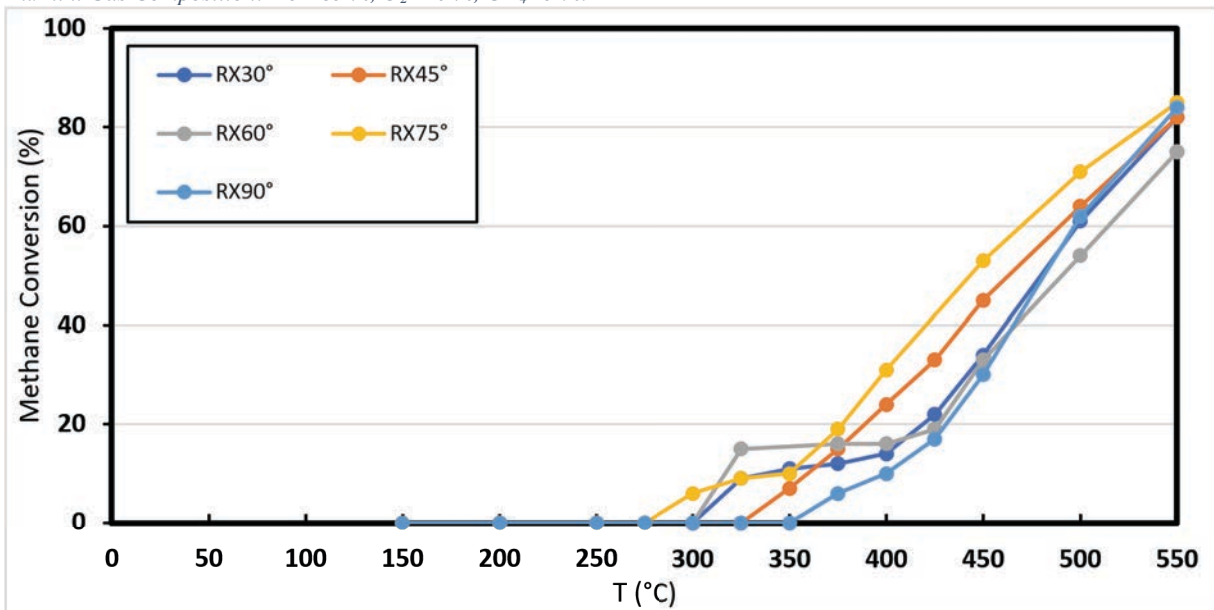


Figure 80: Light-off curve for robocast printed substrates with 0.7 mm wide fibres rotated along the X-axis. Flow Rate = 100 ml/min. Gas Composition: He = 85 %, O₂ = 10 %, CH₄ = 5 %.

Table 10: Properties of the DLP substrates designed with rotated fibres along the X-axis.

	T _{10%} (°C)	T _{50%} (°C)	T _{50%} - T _{10%} (°C)	Surface Area (mm ²)	Number of Exposed Faces	Open Frontal Area	CPSI
DLPX30	368	421	53	10505	3868	0.40	331

DLPX45	354	459	105	10523	4710	0.39	427
DLPX60	400	452	52	10516	5110	0.36	480
DLPX75	372	423	51	10587	5102	0.39	413
DLPX90	400	442	42	10538	5698	0.52	287

6.4. Advanced DLP substrate activity testing

6.4.1. DLP and Commercial Substrate Comparison

The third stage of testing involved a comparison between a 90° woodstock pile DLP printed substrates and a 400 CPSI commercial monolith. The design of the 90° woodstock pile substrate is the most comparable to the commercial monolith due to the same channel shape when analysing from the cross-sectional area in the direction of the gas flow. However, the interconnectivity of the channels differs, resulting in changes to several properties, such as the surface area and the number of exposed faces.

Testing began with a commercial monolith which had undergone the same washcoating procedure as all the other substrates. For reproducibility purposes, three individual samples were tested and the results are displayed in Figure 81. Methane activation occurred between 325 °C and 375 °C. Below 400 °C, methane conversion gradually increased before a sharper increase, per temperature increment, above 400 °C for all three samples. The final conversion at 550 °C for the three samples averaged 80 % with a range of 11 % across the three samples. All three samples exhibited a similar pattern of methane conversion.

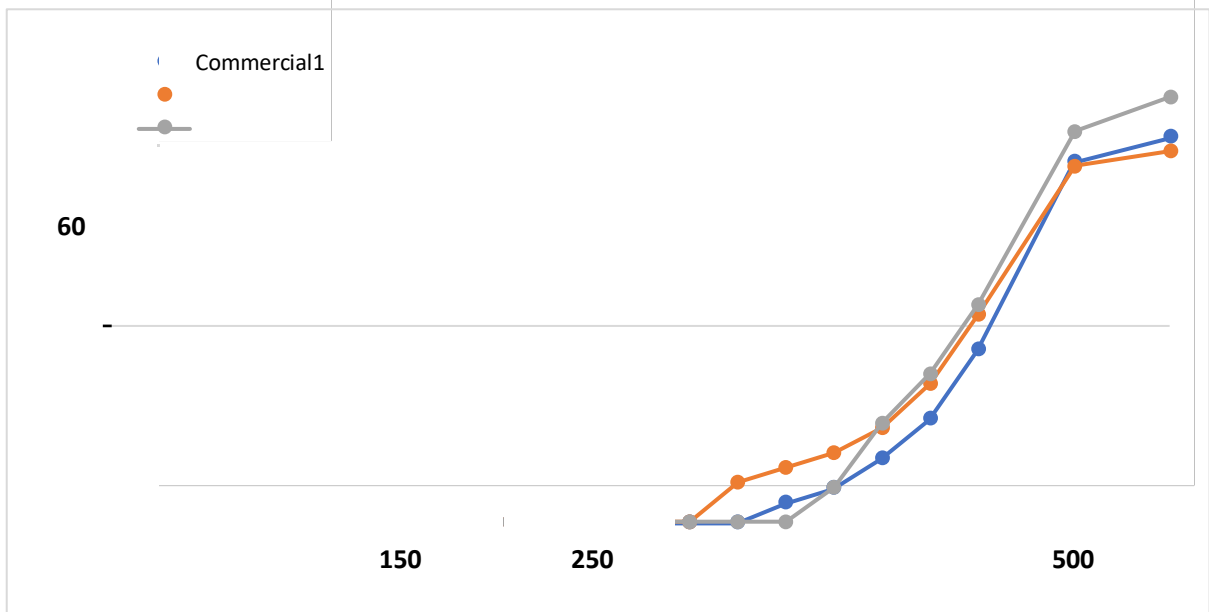


Figure 81: Light-off curve for three commercial monolith. Flow Rate = 100 ml/min. Gas Composition: He = 85 %, O₂ = 10 %, CH₄ = 5 %.

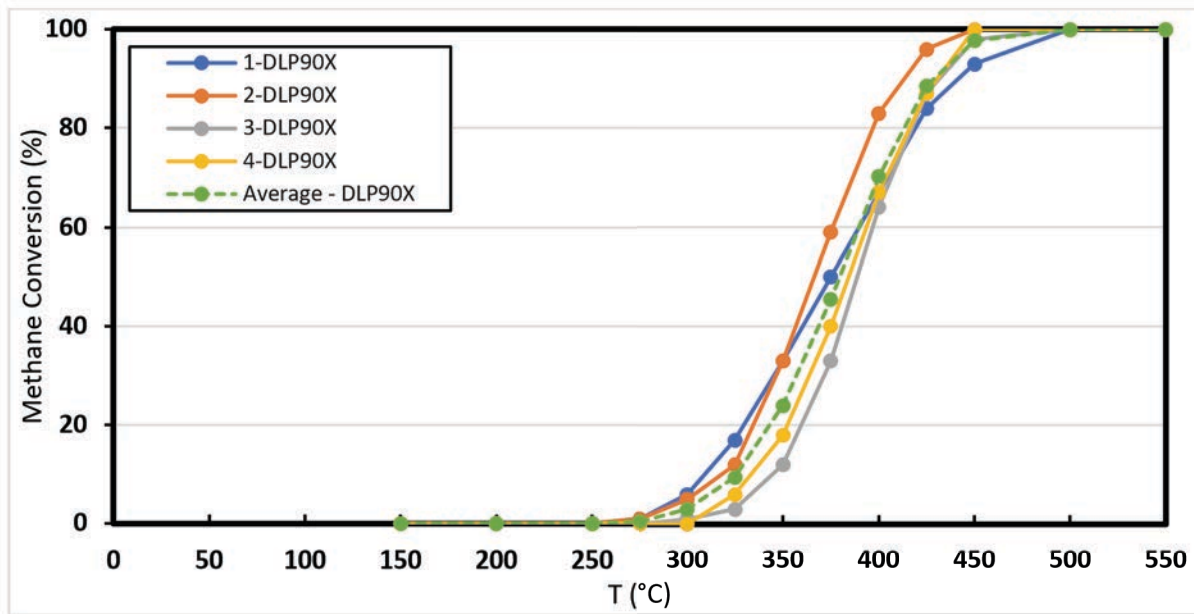


Figure 82: Light-off curve for four 90 woodstock pile DLP printed substrates with a 0.5 mm fibre width. Flow Rate = 100 ml/min. Gas Composition: He= 85 %, O₂ = 10 %, CH₄ = 5 %.

Table 11: Properties of a DLP-90°-0.5mm fibre width substrate and a commercial monolith.

	Average T _{10%} (°C)	Average T _{50%} (°C)	Average T _{50%} - T _{10%} (°C)	Surface Area (mm ²)	Number of Exposed Faces	Open Frontal Area	CPSI
Commercial	376	464	88	15740	870	0.76	400
DLP90X	325	380	55	10538	5698	0.52	287

The DLP-printed substrates showed a noteworthy improvement in converting methane. The light-off curves in Figure 82 reveal that these substrates exhibited better methane conversion across all the temperatures tested. Four samples were tested, each having been printed with a different batch of DLP resin and all having undergone the same wash coating procedure. Activation of all four samples occurred at a lower temperature range, 275 – 300 °C, compared to the commercial monoliths. This could be justified by the lower OFA of 0.24, but the most significant improvements were observed at the higher temperature range. All four substrates tested showed over 90 % methane conversion above 450 °C before achieving 100 % conversion above 500 °C. These activities were not achieved by the 400 CPSI commercial monolith at any temperature.

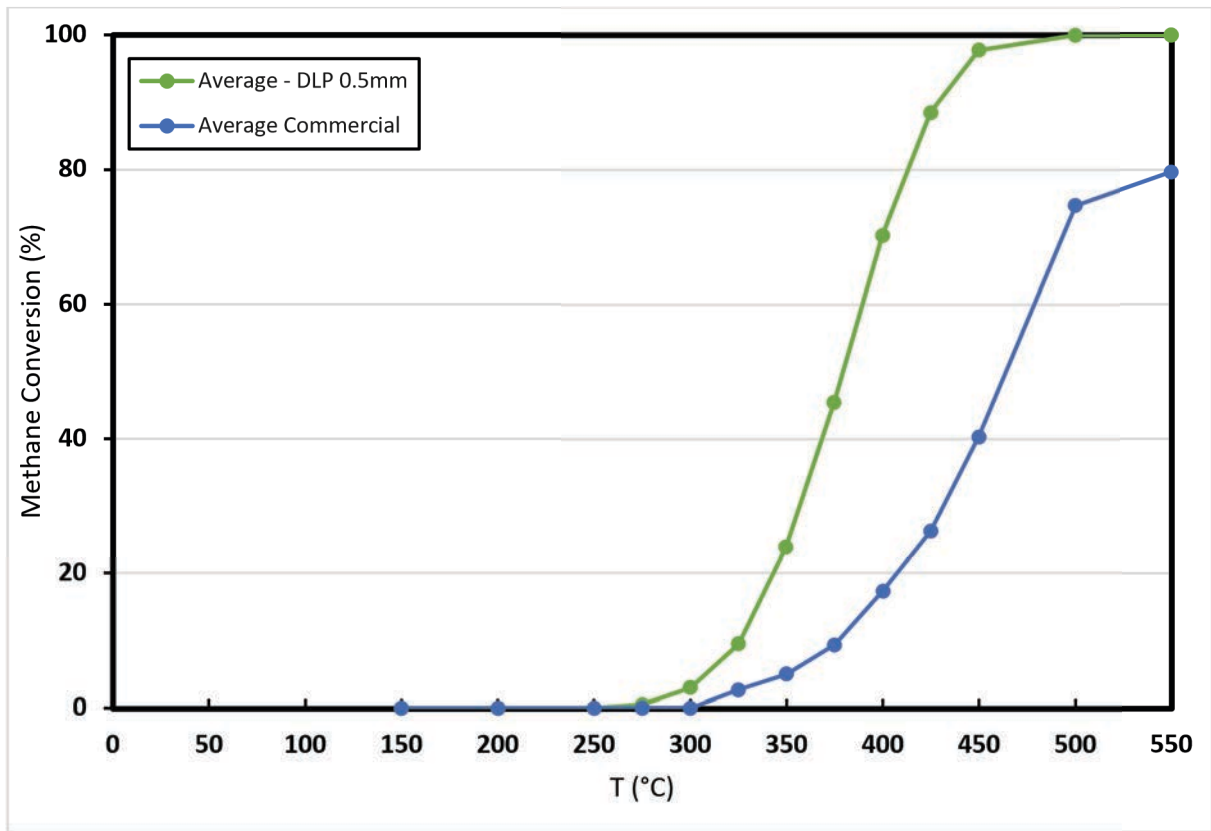


Figure 83: Light-off comparing the average conversion data for a commercial monolith and a 90° DLP substrate with a 0.5 mm fibre width. Flow Rate = 100 ml/min. Gas Composition: He= 85 %, O₂ = 10 %, CH₄ = 5 %.

6.4.2. Z-Axis Variation

The fourth testing category consisted of DLP printed substrates with a 0.5 mm fibre width, with each printed layer of fibres rotated along the Z axis. The light off curves are displayed in Figure 84. The key indicates the angle at which each substrate's fibres were rotated, for example, Z7.5 was a rotation of 7.5° producing the substrate designs seen in Figure 70.

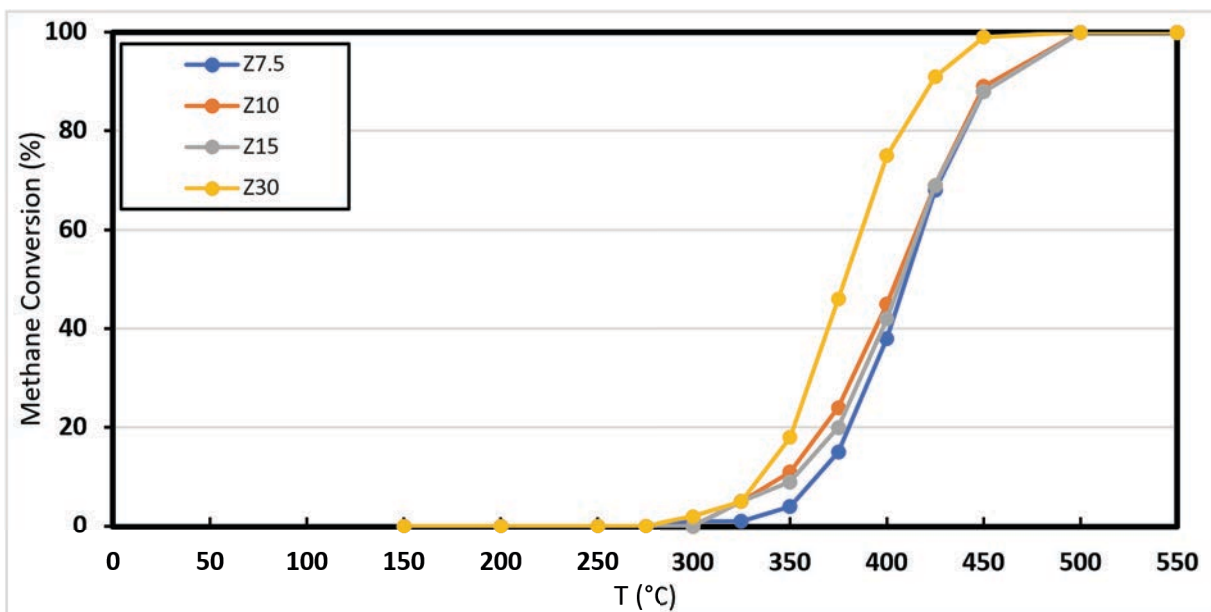


Figure 84: Light-off curve for four DLP printed substrates with a 0.5 mm fibre width and rotation of the fibres in the Z axis. Flow Rate = 100 ml/min. Gas Composition: He = 85 %, O₂ = 10 %, CH₄ = 5 %.

Table 12: Properties of a DLP substrate with 0.5 mm fibres rotated along the Z-axis.

	T _{10%} (°C)	T _{50%} (°C)	T _{50%} - T _{10%} (°C)	Surface Area (mm ²)	Number of Exposed Faces	Open Frontal Area	CPSI
Z7.5	363	410	47	10458	59.42	52	287
Z10	346	405	59	10498	58.18	52	287
Z15	353	407	54	10585	63.58	52	287
Z30	335	378	43	8827	44.86	52	287

The testing results show similarities between the 7.5°, 10° and 15° substrates. At temperatures above 400 °C, methane conversion is almost inseparable. All three substrates achieved 100 % methane conversion at 500 °C with no more than a 1 % difference at any given temperature above 400 °C. Below 400 °C, there is some variation in the results. Although all three substrates became active at 325 °C, between 325 °C and 400 °C there was a slight difference between methane conversion. The largest range observed was 9 % at 375 °C, with the Z10 performing slightly better than both the Z7.5 and Z15.

The outlier for this set of results is the Z30 substrate. It was activated 25 °C lower than the other three substrates and consistently outperformed them at every remaining temperature interval. The largest improvement was seen at 400 °C where

Z30 exhibits a 30 % improvement in methane conversion compared to the next best substrate, Z10.

Considering all four substrates have a consistent OFA and CPSI of 0.52 and 287, respectively, the remaining properties are of interest. Surprisingly, the substrate with the lowest surface area and the number of exposed faces performed the best, which contradicted the initial assumptions. However, upon reviewing the CAD drawings for these designs, the Z30 has a more intricate internal structure with more internal chambers. This could be responsible for the improvement in activity as the increased internal complexity increases the turbulence within the substrate. Further research, including CFD analysis, may help to prove this theory but was beyond the scope of this project's results.

6.4.3. Y-Axis Variation

The fifth category of substrate designs to be tested included the DLP printed substrates, with a 0.5 mm fibre width, with each layer of fibres rotated in the Y axis. Figure 84 displays the light-off curve results. The graphs key uses the same naming technique as the previous results. All the Y-axis substrates that were tested achieved 100 % conversion at 500 °C. Out of the four substrates tested, Y15 and Y30 performed best, surpassing the performance of Y5 and Y7.5 across the full temperature range. Even at 450 °C, Y15 and Y30 managed to achieve over 99 % conversion.

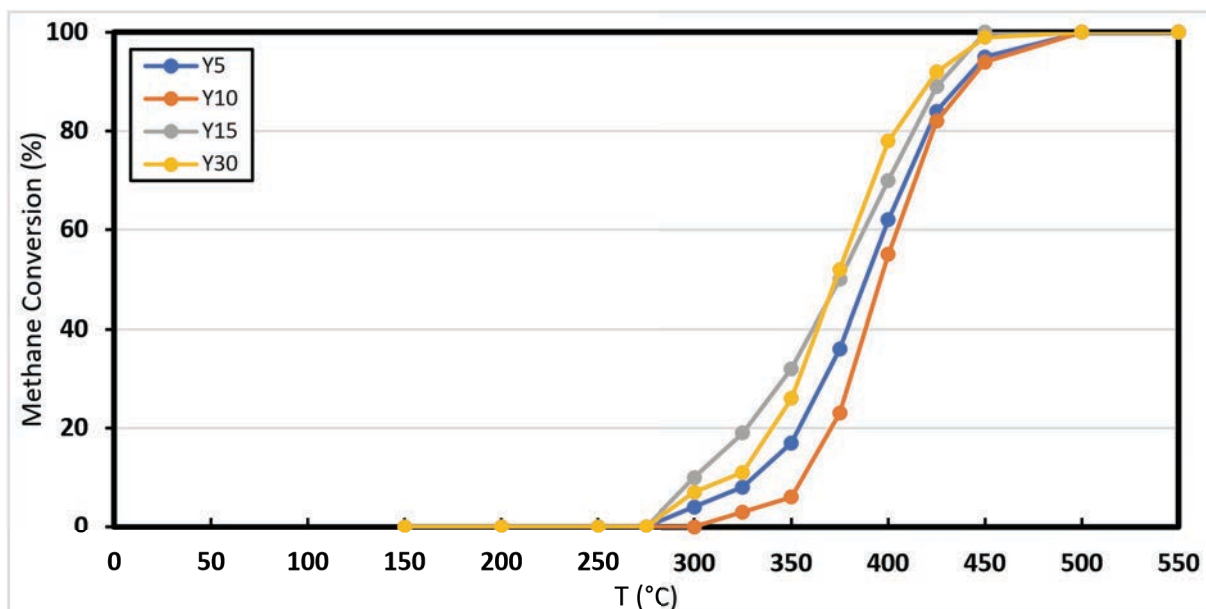


Figure 85: Light-off curve for four DLP printed substrates with a 0.5 mm fibre width and rotation of the fibres in the Y-axis. Flow Rate = 100 ml/min. Gas Composition: He = 85 %, O₂ = 10 %, CH₄ = 5 %.

Table 13: Properties of a DLP substrate with 0.5 mm fibres rotated along the Y-axis.

	T _{10%} (°C)	T _{50%} (°C)	T _{50%} - T _{10%} (°C)	Surface Area	Number of Exposed Faces	Open Frontal Area	CPSI
Y5	330	389	59	8638	26.12	39	292
Y10	356	396	40	8858	42.24	33	292
Y15	300	375	75	7962	41.62	22	292
Y30	318	373	55	7746	36.74	0	0

Most of the substrates were activated at 300 °C except for Y7.5 which activated at 325 °C. At 300 °C, Y5, Y15 and Y30 had a methane conversion range of 3 % with Y15 performing the best converting 10 % of the methane. As the temperature increased, the difference between the four substrates was more prominent. The largest difference was observed at 375 °C, where there was a methane conversion range of 23 % between Y7.5 and Y30.

At temperatures over 400 °C, the difference in methane conversion between the four substrates was smaller, with Y15 and Y30 still outperforming Y7.5 and Y5, but the difference in results narrows down to only 10 % at 425 °C. It is at temperatures

below 400 °C where the variation of the substrate design seems to have the most prominent effect. This could be related to the reduction in OFA. Y15 and Y30 perform best and have a significantly lower OFA, 0.22 and 0.00 respectively. This results in a larger initial surface area for the reactants to encounter the catalyst.

6.4.4. Best Performing Substrates

Figure 86 below displays the light-off curve for the best-performing substrates from each category of designs. The substrates that were 3D printed using DLP technology performed better than the commercial 400 CPSI substrate across the entire temperature range. This was especially notable at 425 °C, where there was over three times as much methane conversion. When the temperature was raised to 550 °C, the commercial monolith achieved a maximum conversion of 80 %, while all three DLP printed substrates achieved 100 %. Upon comparing the commercial substrate to the DLP printed substrates, some interesting differences were observed between certain properties.

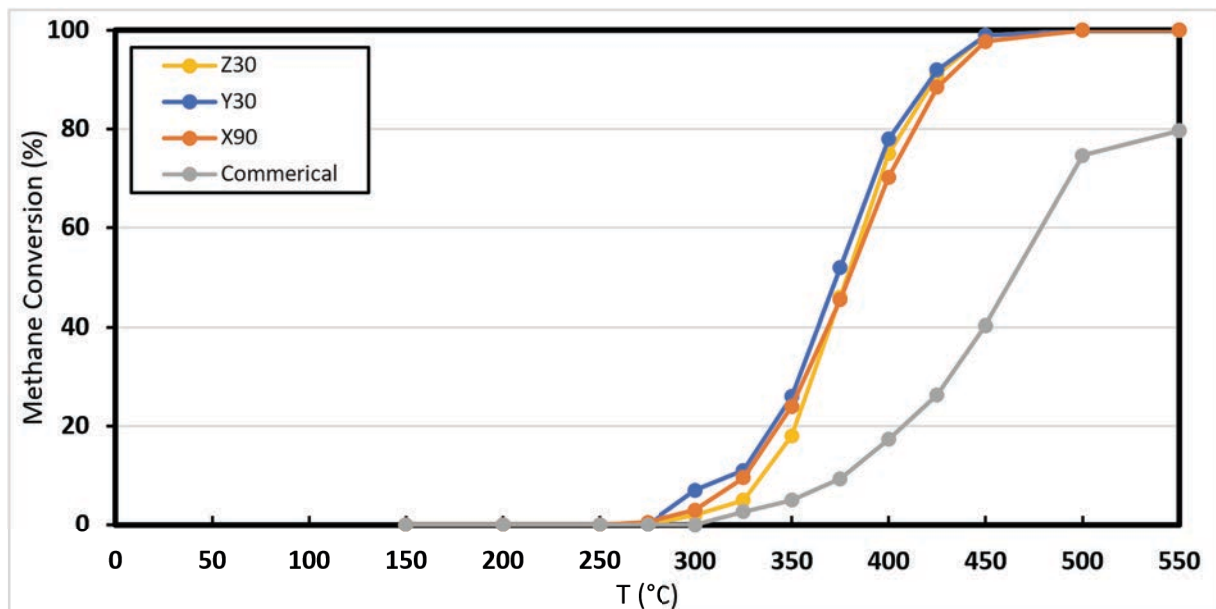


Figure 86: Light-off curve for the best-performing DLP printed substrate from each design category and a commercial substrate. Flow Rate = 100 ml/min. Gas Composition: He = 85 %, O₂ = 10 %, CH₄ = 5 %.

Table 14: Properties of the best performing DLP substrate and a commercial monolith.

	T _{10%} (°C)	T _{50%} (°C)	T _{50%} - T _{10%} (°C)	Surface (mm ²) 15740 Area	Number of Exposed Faces	Open Frontal Area	CPSI
Commercial	376	464	88	15740	870	0.76	400
Z30	335	378	43	8827	4486	0.52	287
Y30	318	373	55	7746	3674	0.00	0
X90	325	380	55	10538	5698	0.52	287

The commercial 400 CPSI monolith has a higher OFA compared to the 3D printed substrates by around 0.24 than the next closest substrate, Z30. This could contribute to the enhanced activity of Z30. However, as the OFA continues to decrease across the DLP printed substrates, this doesn't necessarily lead to a significant improvement in their activity. This suggests that there may be other factors contributing to the observed increase in activity. The CPSI is another property which is advantageous towards the 400 CPSI monolith, containing up to an extra 113 channels than the next closest substrate, X90 or Z30. However, Y30 has substantially fewer channels than any of the other four substrates without showing substantially better activity results. This implies the improvement in activity may not be solely attributed to CPSI. When it comes to surface area, the 400 CPSI monolith has the largest surface area of the four substrates, measuring at 15740 mm². In comparison, X90 measures at 10538 mm², a difference of 5202 mm², representing just over a 30 % decrease. If it was a simple connection of an increased surface area improving catalytic activity, the 400 CPSI commercial monolith should outperform the three DLP printed substrates; however, this is not the case.

The one property which stands out in comparison is the number of exposed faces. The commercial monolith only contains around 870 compared to 7746, 8827 and 10538 for Y30, Z30 and X90, respectively. This increase ranges from between 9 to 12-fold. A higher number of exposed faces is likely a cause for an increase in turbulence within the system, which has been proven in the literature to result in improved catalytic activity.^{228, 229}

6.4.5. Substrate Lifetime Study

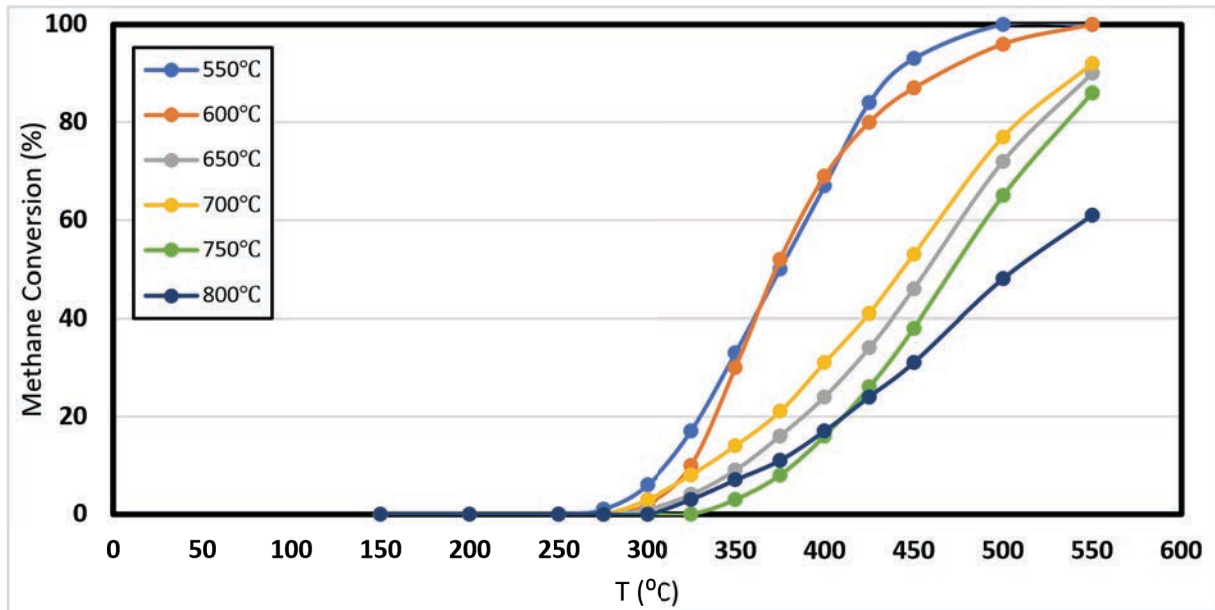


Figure 87: Light-off curve for a study of the lifetime of a 90° woodstock pile design substrate with a 0.5mm fibre width. Flow Rate = 100 ml/min. Gas Composition: He = 85 %, O₂ = 10 %, CH₄ = 5 %.

To understand the behaviour of the substrate over time, a lifetime study was conducted with the results displayed in Figure 87. A single washcoated monolith was subject to an activity test, before being soaked at a set temperature for 6 hours to simulate substrate ageing. The graphs key refers to the light-off curve for the substrate after the temperature it was aged at. For example, the 600 °C light-off curve had undergone a full activity test before the temperature was increased to 600 °C for 4 hours, then cooled back down to 150 °C. A complete activity run was then conducted with the results shown in the 600 °C light-off curve. After the activity run, the temperature of the substrate was increased to 650 °C for 6 hours, cooled back to 150 °C where another activity run was performed, with the results displayed in the 650 °C light-off curve and so on. The final temperature was concluded at 800 °C, mainly due to the safety of the furnace and a visually significant drop-off in activity. Based on the results, it has been observed that the substrate's activity experiences a significant decline across the temperature range once it hits over 600 °C. This

provides evidence that the catalyst loses its effectiveness as it ages, particularly when temperatures exceed 600 °C within the system. If this substrate is integrated into a real-life system that reaches such high temperatures, a more stable catalyst may be necessary, even if it means sacrificing some catalytic activity. Nevertheless, the substrate itself remains usable beyond these temperatures, indicating that the DLP printed substrate can be utilized for this purpose if required. To gain a deeper understanding of how different catalysts behave when wash-coated onto this substrate at higher temperatures, further investigation is necessary, which falls outside the scope of these results.

7. Conclusions

An investigation was conducted into the effectiveness of 3D printed substrates for the purpose of complete methane oxidation. The aim was to try and reduce the amount of methane produced by a vehicle exhaust stream.

24 CAD designs were produced with varying internal geometry, and their physical properties were recorded, including their surface area, open frontal area, channels per square inch and the number of exposed faces. This allowed a comparison between important properties which maybe influential to the catalytic effectiveness of monoliths.

Two 3D printing methods, namely robocasting and digital light processing, were first utilised to manufacture a simple 90° woodstock pile design substrate. It was concluded that DLP was more capable of creating a) more complex internal geometries and b) more refined printing definition, including thinner substrate walls, so was selected to investigate further. A unique DLP resin suitable for the printing purpose of this study was therefore produced, using a stepwise process consisting of over 50 wt.% solid cordierite loading with a cure time of under 10 seconds. This was the first of its kind mentioned in scientific literature and was an extremely time

consuming and difficult part of the research which required lots of trial and error. It is considered one of the greater achievements of this research.

Once the resin had been optimised, the 24 substrates were manufactured and compared for their catalytic activity at completely oxidizing methane. A top-of-the-line catalytic testing rig equipped with a gas chromatography analytical instrument and a thermal conductivity detector was utilised. To ensure accuracy, each sample was subjected to the same wash coating method with the same catalyst to generate catalytic active samples for testing.

The 3D printed substrates displayed a higher level of mass transfer compared to honeycomb monoliths, mostly due to the interconnectivity of their channels and therefore increased number of exposed faces increasing the level of internal turbulence in the system. Although the research showed the surface area is usually lower for 3D printed substrates, their catalytic activity is usually better. All the 3D printed substrates outperformed the commercial substrates at every temperature tested. When reviewing the best-performing 3D printed substrates, there was a substantial improvement of over three times as much methane conversion compared to the commercial monolith. These results display the improvement 3D printed substrates can offer catalytic activity.

8. Future Works

There is great potential to explore how turbulence can further improve catalytic conversion. Progressing the development of intricate designs which optimise the relationship between back pressure and catalytic activity could lead to even better substrates. An interesting avenue for this could be introducing the use of AI to try and produce an ideal design. Specific parameters, such as flow rate, temperature and reaction conditions could be fed into the program which could produce a design

maximising turbulent flow and mass transfer to gain the best results in terms of catalytic conversion.

Additionally, using DLP technology to produce a full-size catalytic converter for testing under industrial conditions would provide additional understanding of the effectiveness of 3D printed substrates for catalytic purposes. This allows result collection which closer aligns to real-life conditions, giving a more telling insight into the effectiveness of 3D printed substrates compared to commercial counterparts.

Considering the 3D printed substrate also has a lower surface area than a commercial monolith, there is potential for further research to see if a lower loading of catalyst could produce the same catalytic result which could result in a lower cost of catalyst per monolith if successful.

Furthermore, this thesis could act as a blueprint to trial additional gaseous catalytic reactions such as NO_x abatement. Depending on the substrate produced, further reactions could be trialled which utilise a different catalyst wash coated on the solid substrate.

All the above are viable options to further expand the scope of this work and would contribute to the larger scientific picture.

9. Bibliography

- (1) Boretti, A. Advantages and disadvantages of diesel single and dual-fuel engines. *Frontiers in Mechanical Engineering* **2019**, *5*, 64.
- (2) Ashok, B.; Denis Ashok, S.; Ramesh Kumar, C. LPG diesel dual fuel engine – A critical review. *Alexandria Engineering Journal* **2015**, *54* (2), 105-126. DOI: <https://doi.org/10.1016/j.aej.2015.03.002>.
- (3) Nugroho, A.; Sinaga, N.; Haryanto, I. Performance of a compression ignition engine four strokes four cylinders on dual fuel (diesel–LPG). *AIP Conference Proceedings* **2018**, *2014* (1), 020166. DOI: 10.1063/1.5054570.
- (4) Pham, Q.; Park, S.; Agarwal, A. K.; Park, S. Review of dual-fuel combustion in the compression-ignition engine: Spray, combustion, and emission. *Energy* **2022**, *250*, 123778.
DOI: <https://doi.org/10.1016/j.energy.2022.123778>.

- (5) Karim, G. A. *Dual-fuel diesel engines*; CRC Press, 2015.
- (6) Martin, P.; Smith, A. *Engine Fuel Supply System*. Europe 2013.
- (7) Ltd, G.-V. *The G-Volution Optimiser*. 2017. (accessed 2022 June 2022).
- (8) Ltd, G.-V. AN ALTERNATIVE WAY TO REDUCE CARBON, REDUCE COSTS - AND CLEAN THE AIR ON EXISTING RAIL ASSETS TODAY:. Committee, T., Ed.; UK Parliament: <https://committees.parliament.uk/writtenevidence/13913/pdf/>, 2020.
- (9) Arefin, M. A.; Nabi, M. N.; Akram, M. W.; Islam, M. T.; Chowdhury, M. W. A Review on Liquefied Natural Gas as Fuels for Dual Fuel Engines: Opportunities, Challenges and Responses. *Energies* **2020**, *13* (22), 6127.
- (10) GIIGNL. *The LNG Industry: GIIGNL Annual Report*. International Group of LNG Importers Neuilly-sur-Seine, France: 2018.
- (11) Wlodek, T.; Kuczyński, S.; Szurlej, A.; Łaciak, M. Impact of Liquefied Natural Gas Composition Changes on Methane Number as a Fuel Quality Requirement. *Energies* **2020**, *13*, 5060. DOI: 10.3390/en13195060.
- (12) Kumar, S.; Kwon, H.-T.; Choi, K.-H.; Lim, W.; Cho, J. H.; Tak, K.; Moon, I. LNG: An ecofriendly cryogenic fuel for sustainable development. *Applied Energy* **2011**, *88* (12), 42644273. DOI: <https://doi.org/10.1016/j.apenergy.2011.06.035>.
- (13) Stephenson, M. Chapter 3 - To Frack or Not to Frack? In *Shale Gas and Fracking*, Stephenson, M. Ed.; Elsevier, 2015; pp 57-72.
- (14) Engineering Toolbox. *Fuels-Higher and Lower Calorific Values*. 2003. (accessed 2022 June).
- (15) Mohammad, M.; Ehsani, M. An investigation of natural gas as a substitute for diesel in heavy duty trucks and associated considerations. *arXiv preprint arXiv:1512.01421* **2015**.
- (16) Wei, L.; Geng, P. A review on natural gas/diesel dual fuel combustion, emissions and performance. *Fuel Processing Technology* **2016**, *142*, 264-278. DOI: <https://doi.org/10.1016/j.fuproc.2015.09.018>.
- (17) Vermeulen, R. J. Emissions testing of a Euro VI LNG-diesel dual fuel truck in the Netherlands. 2019.
- (18) Stettler, M. E. J.; Midgley, W. J. B.; Swanson, J. J.; Cebon, D.; Boies, A. M. Greenhouse Gas and Noxious Emissions from Dual Fuel Diesel and Natural Gas Heavy Goods Vehicles. *Environmental Science & Technology* **2016**, *50* (4), 2018-2026. DOI: 10.1021/acs.est.5b04240.
- (19) Zarrinkolah, M. T.; Hosseini, V. Methane Slip Reduction of Conventional Dual-Fuel Natural Gas Diesel Engine Using Direct Fuel Injection Management and Alternative Combustion Modes. *Available at SSRN 4159439*.
- (20) Balcombe, P.; Heggo, D. A.; Harrison, M. Total Methane and CO2 Emissions from Liquefied Natural Gas Carrier Ships: The First Primary Measurements. *Environmental Science & Technology* **2022**, *56* (13), 9632-9640. DOI: 10.1021/acs.est.2c01383.
- (21) Hooftman, N.; Messagie, M.; Van Mierlo, J.; Coosemans, T. A review of the European passenger car regulations – Real driving emissions vs local air quality. *Renewable and Sustainable Energy Reviews* **2018**, *86*, 1-21. DOI: <https://doi.org/10.1016/j.rser.2018.01.012>.
- (22) Williams, M.; Minjares, R. A technical summary of Euro 6/VI vehicle emission standards. *International Council for Clean Transportation (ICCT), Washington, DC, accessed July 2016*, *10*, 2017.
- (23) Grigoratos, T.; Fontaras, G.; Giechaskiel, B.; Zacharof, N. Real world emissions performance of heavy-duty Euro VI diesel vehicles. *Atmospheric Environment* **2019**, *201*, 348-359. DOI: <https://doi.org/10.1016/j.atmosenv.2018.12.042>.

- (24) DieselNet. EU:Cars and Light Trucks. <https://dieselnet.com/standards/eu/ld.php>, 2022.
- (25) DieselNet. EU:Heavy-Duty Truck and Bus Engines. <https://dieselnet.com/standards/eu/hd.php>, 2021.
- (26) Lutsey, N. The ever-improving efficiency of the diesel engine. The International Council on Clean Transportation: <https://theicct.org/the-ever-improving-efficiency-of-the-dieselengine/>, 2015; Vol. 2022.
- (27) Association, A.-T. E. A. M. Fuel types of new trucks: diesel 97.9%, electric 0.2%, hybrid 0.1% market share in 2019. 2019.
- (28) Wang, Z.; Pan, X.; Zhang, W.; Zhao, Y.; Li, H.; Liu, P. The Development Trend of Internal Combustion Engine. *Journal of Physics: Conference Series* **2020**, 1626 (1), 012139. DOI: 10.1088/1742-6596/1626/1/012139.
- (29) Reşitoğlu, İ. A.; Altinişik, K.; Keskin, A. The pollutant emissions from diesel-engine vehicles and exhaust aftertreatment systems. *Clean Technologies and Environmental Policy* **2015**, 17 (1), 15-27. DOI: 10.1007/s10098-014-0793-9.
- (30) Manabe, S. Role of greenhouse gas in climate change**. *Tellus A: Dynamic Meteorology and Oceanography* **2019**, 71 (1), 1620078. DOI: 10.1080/16000870.2019.1620078. (31) Lamb, W.; Wiedmann, T.; Pongratz, J.; Andrew, R.; Crippa, M.; Olivier, J.; Wiedenhofer, D.; Mattioli, G.; Al Khourdajie, A.; House, J.; et al. A review of trends and drivers of greenhouse gas emissions by sector from 1990 to 2018. *Environmental Research Letters* **2021**, 16. DOI: 10.1088/1748-9326/abee4e.
- (32) Sydbom, A.; Blomberg, A.; Parnia, S.; Stenfors, N.; Sandström, T.; Dahlén, S. E. Health effects of diesel exhaust emissions. *European Respiratory Journal* **2001**, 17 (4), 733.
- (33) Johnson, T.; Joshi, A. *Review of Vehicle Engine Efficiency and Emissions*; 2017. DOI: 10.4271/2017-01-0907.
- (34) Treude, T. Anaerobic Oxidation of Methane in marine sediments. http://elib.suub.unibremen.de/publications/dissertations/E-Diss845_treude.pdf **2004**.
- (35) PubChem Compound Summary for CID 297, Methane. National Center for Biotechnology Information, 2022. (accessed 2022 June).
- (36) McMurry, J. E.; Fay, R. C. *General chemistry: Atoms first*; Pearson Higher Ed, 2013.
- (37) Stephanos, J. J.; Addison, A. W. Chapter 5 - Valence Bond Theory and Orbital Hybridization. In *Electrons, Atoms, and Molecules in Inorganic Chemistry*, Stephanos, J. J., Addison, A. W. Eds.; Academic Press, 2017; pp 281-330.
- (38) Li, Z.; Hoflund, G. A Review on Complete Oxidation of Methane at Low Temperatures. *Journal of Natural Gas Chemistry* **2003**, 12, 153-160.
- (39) ReviseZone. *Enthalpy Change*. revise zone, 2020. (accessed 2023 June).
- (40) Britannica, E. Haber-Bosch Process. Retrieved: 2017.
- (41) Chorkendorff, I.; Niemantsverdriet, J. W. *Concepts of modern catalysis and kinetics*; John Wiley & Sons, 2017.
- (42) Nm, D. Sintering process and catalysis. *International Journal of Nanomaterials, Nanotechnology and Nanomedicine* **2017**, 004-008. DOI: 10.17352/2455-3492.000023.
- (43) Tanaka, K.-i.; He, H. Activation of solid surface as catalyst. *Catalysis Today* **2013**, 201, 2-6. DOI: <https://doi.org/10.1016/j.cattod.2012.05.007>.
- (44) Liu, S.; Zhu, M.; Iqbal, M. Research Progress on Stability of Solid Acid Catalysts. *Catalysis Surveys from Asia* **2020**, 24. DOI: 10.1007/s10563-020-09305-5.
- (45) Palmisano, G.; Jitan, S. A.; Garlisi, C. Chapter 2 - Fundamentals of the adsorption process. In *Heterogeneous Catalysis*, Palmisano, G., Jitan, S. A., Garlisi, C. Eds.; Elsevier, 2022; pp 27-62.

- (46) Kakaei, K.; Esrafil, M. D.; Ehsani, A. Chapter 1 - Introduction to Catalysis. In *Interface Science and Technology*, Kakaei, K., Esrafil, M. D., Ehsani, A. Eds.; Vol. 27; Elsevier, 2019; pp 1-21.
- (47) Albertin, S. Preparation, characterization and testing of model catalysts for CO oxidation and CO₂ hydrogenation. Lund University, 2017.
- (48) Streeter, C. Catalytic converter. Dorling Kindersley: Getty Images, 2014.
- (49) Houdry, E. J. Catalytic structure and composition. United States 1952.
- (50) Taylor, K. C. Automobile Catalytic Converters. In *Studies in Surface Science and Catalysis*, Crucq, A., Frennet, A. Eds.; Vol. 30; Elsevier, 1987; pp 97-116.
- (51) Thakur, P. 11 - Diesel Exhaust Control. In *Advanced Mine Ventilation*, Thakur, P. Ed.; Woodhead Publishing, 2019; pp 157-187.
- (52) Prins, R.; Wang, A.; Li, X. *Introduction to Heterogeneous Catalysis*; WORLD SCIENTIFIC (EUROPE), 2015. DOI: doi:10.1142/q0024.
- (53) Kritsanaviparkporn, E.; Baena-Moreno, F. M.; Reina, T. R. Catalytic Converters for Vehicle Exhaust: Fundamental Aspects and Technology Overview for Newcomers to the Field. *Chemistry* **2021**, *3* (2), 630-646. DOI: 10.3390/chemistry3020044.
- (54) Singh, M. A Review on Catalytic converter for automotive exhaust emission. *International Journal of Scientific and Engineering Research* **2016**, *7*, 927-932.
- (55) Wade, J.; Farrauto, R. J. 12 - Controlling emissions of pollutants in urban areas. In *Metropolitan Sustainability*, Zeman, F. Ed.; Woodhead Publishing, 2012; pp 260-291.
- (56) Sathish Sharma, G.; Sugavaneswaran, M.; Prakash, R. Chapter 8 - NO_x reduction in IC engines through after treatment catalytic converter. In *NO_x Emission Control Technologies in Stationary and Automotive Internal Combustion Engines*, Ashok, B. Ed.; Elsevier, 2022; pp 223-253.
- (57) Xin, Q. 8 - Diesel aftertreatment integration and matching. In *Diesel Engine System Design*, Xin, Q. Ed.; Woodhead Publishing, 2013; pp 503-525.
- (58) Llorca, J. Monolithic Reactor. In *Encyclopedia of Membranes*, Drioli, E., Giorno, L. Eds.; Springer Berlin Heidelberg, 2015; pp 1-3.
- (59) Boger, T. Monolithic Catalysts for the Chemical Industry. *Industrial & Engineering Chemistry Research* **2004**, *43*. DOI: 10.1021/ie030730q.
- (60) Nijhuis, T. A.; Kapteijn, F.; Moulijn, J. A. Monolithic catalysts as more efficient reactors in three-phase applications. In *Studies in Surface Science and Catalysis*, Corma, A., Melo, F. V., Mendioroz, S., Fierro, J. L. G. Eds.; Vol. 130; Elsevier, 2000; pp 2735-2740.
- (61) Heck, R. M.; Gulati, S.; Farrauto, R. J. The application of monoliths for gas phase catalytic reactions. *Chemical Engineering Journal* **2001**, *82* (1), 149-156. DOI: [https://doi.org/10.1016/S1385-8947\(00\)00365-X](https://doi.org/10.1016/S1385-8947(00)00365-X).
- (62) Zamaniyan, A.; Mortazavi, Y.; Khodadadi, A. A.; Manafi, H. Tube fitted bulk monolithic catalyst as novel structured reactor for gas–solid reactions. *Applied Catalysis A: General* **2010**, *385* (1), 214-223. DOI: <https://doi.org/10.1016/j.apcata.2010.07.014>.
- (63) Heck, R. M.; Farrauto, R. J.; Gulati, S. T. Monolithic Reactors for Environmental Catalysis. In *Catalytic Air Pollution Control*, 2009; pp 63-78.
- (64) Wang, Z.; Zhao, K.; Xiao, B.; Gao, P.; He, D.; Cai, T.; Yuan, J. Fabrication of Monolithic Catalysts: Comparison of the Traditional and the Novel Green Methods. *Catalysts* **2019**, *9* (12), 981.
- (65) Williams, J. L. Monolith structures, materials, properties and uses. *Catalysis Today* **2001**, *69* (1-4), 3-9.
- (66) Baharudin, L.; Watson, M. Monolithic substrate support catalyst design considerations for steam methane reforming operation. *Reviews in Chemical Engineering* **2017**, *Ahead of Print*. DOI: 10.1515/revce-2016-0048.

- (67) Tomašić, V.; Jović, F. State-of-the-art in the monolithic catalysts/reactors. *Applied Catalysis A: General* **2006**, *311*, 112-121. DOI: <https://doi.org/10.1016/j.apcata.2006.06.013>.
- (68) Cornejo, I.; Garreton, G.; Hayes, R. E. On the Use of Dual Cell Density Monoliths. In *Catalysts*, 2021; Vol. 11.
- (69) Govender, S.; Friedrich, H. Monoliths: A Review of the Basics, Preparation Methods and Their Relevance to Oxidation. *Catalysts* **2017**, *7*, 62. DOI: 10.3390/catal7020062.
- (70) Hajimirzaee, S.; Doyle, A. M. 3D printed catalytic converters with enhanced activity for low-temperature methane oxidation in dual-fuel engines. *Fuel* **2020**, *274*, 117848. DOI: <https://doi.org/10.1016/j.fuel.2020.117848>.
- (71) Gupta, V.; Nesterenko, P.; Paull, B. *An Introduction to 3D Printing*; 2019.
- (72) Jandyal, A.; Chaturvedi, I.; Wazir, I.; Raina, A.; Ul Haq, M. I. 3D printing – A review of processes, materials and applications in industry 4.0. *Sustainable Operations and Computers* **2022**, *3*, 33-42. DOI: <https://doi.org/10.1016/j.susoc.2021.09.004>.
- (73) Jeong, S.-J.; Kim, W.-S.; Kim, T. An application of CFD to improve warm-up performance of the 3-way auto-catalyst by high surface area and low thermal mass. *International Journal of Vehicle Design* **2002**, *29*, 243-269. DOI: 10.1504/IJVD.2002.002012.
- (74) Ferrizz, R. M.; Stuecker, J. N.; Cesarano, J.; Miller, J. E. Monolithic Supports with Unique Geometries and Enhanced Mass Transfer. *Industrial & Engineering Chemistry Research* **2005**, *44* (2), 302-308. DOI: 10.1021/ie049468r.
- (75) *Important 3D printing software features.*; 2020.
- (76) Safonov, A.; Maltsev, E.; Chugunov, S.; Tikhonov, A.; Konev, S.; Evlashin, S.; Popov, D.; Pasko, A.; Akhatov, I. Design and Fabrication of Complex-Shaped Ceramic Bone Implants via 3D Printing Based on Laser Stereolithography. *Applied Sciences* **2020**, *10* (20), 7138.
- (77) Cesarano, J. A Review of Robocasting Technology. *MRS Proceedings* **1998**, *542*, 133.
- (78) WASP. *Delta WASP 4070*. (accessed).
- (79) Saggiomo, V. 3D Printed Devices for Catalytic Systems. 2020; pp 369-408.
- (80) Chhabra, D. Comparison and analysis of different 3d printing techniques. **2017**. DOI: 10.21172/1.841.44.
- (81) Khalasane, M. A review paper on catalytic converter for automotive exhaust emission. *Journal of information, knowledge and research in mechanical engineering* **2016**, *4* (1), 7. (82) Davoudinejad, A. Chapter 5 - Vat photopolymerization methods in additive manufacturing. In *Additive Manufacturing*, Pou, J., Riveiro, A., Davim, J. P. Eds.; Elsevier, 2021; pp 159-181.
- (83) Chaudhary, R.; Fabbri, P.; Leoni, E.; Mazzanti, F.; Akbari, R.; Antonini, C. Additive manufacturing by digital light processing: a review. *Progress in Additive Manufacturing* **2022**. DOI: 10.1007/s40964-022-00336-0.
- (84) Dream 3D. *Photocentric Liquid Crystal Precision 1.5*. (accessed 2022).
- (85) Bove, A.; Calignano, F.; Galati, M.; Iuliano, L. Photopolymerization of Ceramic Resins by Stereolithography Process: A Review. *Applied Sciences* **2022**, *12*, 3591. DOI: 10.3390/app12073591.
- (86) Hinczewski, C.; Corbel, S.; Chartier, T. Ceramic suspensions suitable for stereolithography. *Journal of the European Ceramic Society* **1998**, *18* (6), 583-590. DOI: [https://doi.org/10.1016/S0955-2219\(97\)00186-6](https://doi.org/10.1016/S0955-2219(97)00186-6).
- (87) Manapat, J. Z.; Chen, Q.; Ye, P.; Advincula, R. C. 3D printing of polymer nanocomposites via stereolithography. *Macromolecular Materials and Engineering* **2017**, *302* (9), 1600553. (88) Cho, J. D.; Hong, J. W. Curing kinetics of UV-initiated cationic photopolymerization of divinyl ether photosensitized by thioxanthone. *Journal of applied polymer science* **2005**, *97* (3), 1345-1351.

- (89) Bae, C.-J.; Ramachandran, A.; Chung, K.; Park, S. Ceramic Stereolithography: Additive Manufacturing for 3D Complex Ceramic Structures. *J. Korean Ceram. Soc* **2017**, *54* (6), 470477. DOI: 10.4191/kcers.2017.54.6.12.
- (90) Khudyakov, I. V. Fast photopolymerization of acrylate coatings: Achievements and problems. *Progress in Organic Coatings* **2018**, *121*, 151-159. DOI: <https://doi.org/10.1016/j.porgcoat.2018.04.030>.
- (91) van Rijswijk, K.; Bersee, H. E. N. Reactive processing of textile fiber-reinforced thermoplastic composites – An overview. *Composites Part A: Applied Science and Manufacturing* **2007**, *38* (3), 666-681. DOI: <https://doi.org/10.1016/j.compositesa.2006.05.007>.
- (92) Lee, J. H.; Prud'homme, R. K.; Aksay, I. A. Cure depth in photopolymerization: Experiments and theory. *Journal of Materials Research* **2001**, *16* (12), 3536-3544. DOI: 10.1557/JMR.2001.0485 From Cambridge University Press Cambridge Core.
- (93) Mucci, V.; Vallo, C. Efficiency of 2, 2-dimethoxy-2-phenylacetophenone for the photopolymerization of methacrylate monomers in thick sections. *Journal of Applied Polymer Science* **2012**, *123* (1), 418-425.
- (94) Wang, K.; Li, B.; Ni, K.; Wang, Z. Optimal photoinitiator concentration for light-cured dental resins. *Polymer Testing* **2021**, *94*, 107039. DOI: <https://doi.org/10.1016/j.polymertesting.2020.107039>.
- (95) Jacobs, P. F. Fundamentals of stereolithography. 1992.
- (96) Fan, R. N. Solid imaging method using photohardenable compositions containing hollow spheres. Google Patents: 1991.
- (97) Gentry, S. P.; Halloran, J. W. Depth and width of cured lines in photopolymerizable ceramic suspensions. *Journal of the European Ceramic Society* **2013**, *33* (10), 1981-1988.
- (98) Wu, K.; Seefeldt, K.; Solomon, M. J.; Halloran, J. W. Prediction of ceramic stereolithography resin sensitivity from theory and measurement of diffusive photon transport. *Journal of applied physics* **2005**, *98* (2), 024902.
- (99) Pan, Y.; Chen, Y. Meniscus process optimization for smooth surface fabrication in Stereolithography. *Additive Manufacturing* **2016**, *12*, 321-333.
- (100) Chaput, C.; Chartier, T. Fabrication of ceramics by stereolithography. In *RTjournalForum für Rapid Technologie*, 2007; Vol. 4, p 1.
- (101) Tarabeux, J.; Pateloup, V.; Michaud, P.; Chartier, T. Development of a numerical simulation model for predicting the curing of ceramic systems in the stereolithography process. *Journal of the European Ceramic Society* **2018**, *38* (11), 4089-4098.
- (102) Santoliquido, O.; Camerota, F.; Pelanconi, M.; Ferri, D.; Elsener, M.; Dimopoulos Eggenschwiler, P.; Ortona, A. Structured Alumina Substrates for Environmental Catalysis Produced by Stereolithography. *Applied Sciences* **2021**, *11* (17), 8239.
- (103) Ryu, K.; Kim, J.; Choi, J.; Kim, U. The 3D Printing Behavior of Photocurable Ceramic/Polymer Composite Slurries Prepared with Different Particle Sizes. *Nanomaterials* **2022**, *12* (15), 2631.
- (104) Pick, B.; Gonzaga, C. C.; Junior, W. S.; Kawano, Y.; Braga, R. R.; Cardoso, P. E. C. Influence of curing light attenuation caused by aesthetic indirect restorative materials on resin cement polymerization. *European Journal of Dentistry* **2010**, *4* (03), 314-323.
- (105) de Hazan, Y.; Penner, D. SiC and SiOC ceramic articles produced by stereolithography of acrylate modified polycarbosilane systems. *Journal of the European Ceramic Society* **2017**, *37* (16), 5205-5212. DOI: <https://doi.org/10.1016/j.jeurceramsoc.2017.03.021>.

- (106) Badev, A.; Abouliatim, Y.; Chartier, T.; Lecamp, L.; Lebaudy, P.; Chaput, C.; Delage, C. Photopolymerization kinetics of a polyether acrylate in the presence of ceramic fillers used in stereolithography. *Journal of Photochemistry and Photobiology A: Chemistry* **2011**, *222* (1), 117-122. DOI: <https://doi.org/10.1016/j.jphotochem.2011.05.010>.
- (107) Griffith, M. L.; Halloran, J. W. Freeform fabrication of ceramics via stereolithography. *Journal of the American Ceramic Society* **1996**, *79* (10), 2601-2608.
- (108) Brady, G. A.; Chu, T.-M.; Halloran, J. W. Curing behavior of ceramic resin for stereolithography. In *1996 International Solid Freeform Fabrication Symposium*, 1996.
- (109) Lee, J.-H.; Um, C.-M.; Lee, I.-b. Rheological properties of resin composites according to variations in monomer and filler composition. *Dental Materials* **2006**, *22* (6), 515-526. DOI: <https://doi.org/10.1016/j.dental.2005.05.008>.
- (110) Boukha, Z.; de Rivas, B.; González-Velasco, J. R.; Gutiérrez-Ortiz, J. I.; López-Fonseca, R. Comparative Study of the Efficiency of Different Noble Metals Supported on Hydroxyapatite in the Catalytic Lean Methane Oxidation under Realistic Conditions. *Materials* **2021**, *14* (13), 3612.
- (111) Kim, C. H.; Schmid, M.; Schmiege, S. J.; Tan, J.; Li, W. *The effect of Pt-Pd ratio on oxidation catalysts under simulated diesel exhaust*; SAE Technical Paper, 2011. (112) Ho, P. H.; Woo, J.-W.; Feizie Ilmasani, R.; Han, J.; Olsson, L. The role of Pd–Pt Interactions in the Oxidation and Sulfur Resistance of Bimetallic Pd–Pt/ γ -Al₂O₃ Diesel Oxidation Catalysts. *Industrial & Engineering Chemistry Research* **2021**, *60* (18), 6596-6612. DOI: 10.1021/acs.iecr.0c05622.
- (113) Specchia, S.; Finocchio, E.; Busca, G.; Palmisano, P.; Specchia, V. Surface chemistry and reactivity of ceria–zirconia-supported palladium oxide catalysts for natural gas combustion. *Journal of Catalysis* **2009**, *263* (1), 134-145.
- (114) Cullis, C. F.; Willatt, B. M. Oxidation of methane over supported precious metal catalysts. *Journal of Catalysis* **1983**, *83* (2), 267-285. DOI: [https://doi.org/10.1016/00219517\(83\)90054-4](https://doi.org/10.1016/00219517(83)90054-4).
- (115) Hellman, A.; Resta, A.; Martin, N.; Gustafson, J.; Trinchero, A.; Carlsson, P.-A.; Balmes, O.; Felici, R.; Rijn, R.; Frenken, J.; et al. The Active Phase of Palladium during Methane Oxidation. *The Journal of Physical Chemistry Letters* **2012**, *3*, 678–682. DOI: 10.1021/jz300069s.
- (116) Huang, F.; Chen, J.; Hu, W.; Li, G.; Wu, Y.; Yuan, S.; Zhong, L.; Chen, Y. Pd or PdO: Catalytic active site of methane oxidation operated close to stoichiometric air-to-fuel for natural gas vehicles. *Applied Catalysis B: Environmental* **2017**, *219*. DOI: 10.1016/j.apcatb.2017.07.037.
- (117) Fertal, D.; Bukhovko, M.; Ding, Y.; Billor, Z.; Banerjee, A. Particle Size and PdO–Support Interactions in PdO/CeO₂- γ Al₂O₃ Catalysts and Effect on Methane Combustion. *Catalysts* **2020**, *10*, 976. DOI: 10.3390/catal10090976.
- (118) Briot, P.; Primet, M. Catalytic oxidation of methane over palladium supported on alumina Effect of aging under reactants. *Applied Catalysis* **1991**, *68*, 301-314. DOI: 10.1016/S0166-9834(00)84110-X.
- (119) Kinnunen, N. M.; Hirvi, J. T.; Suvanto, M.; Pakkanen, T. A. Role of the Interface between Pd and PdO in Methane Dissociation. *The Journal of Physical Chemistry C* **2011**, *115* (39), 19197-19202. DOI: 10.1021/jp204360c.
- (120) Hurtado, P.; Ordóñez, S.; Sastre, H.; Diez, F. V. Development of a kinetic model for the oxidation of methane over Pd/Al₂O₃ at dry and wet conditions. *Applied Catalysis B: Environmental* **2004**, *51* (4), 229-238. DOI: <https://doi.org/10.1016/j.apcatb.2004.03.006>.

- (121) Mars, P.; Van Krevelen, D. W. Oxidations carried out by means of vanadium oxide catalysts. *Chemical Engineering Science* **1954**, *3*, 41-59.
- (122) Mkhwanazi, T. P. O.; Farahani, M. D.; Mahomed, A. S.; Singh, S.; Friedrich, H. B. Engineering of catalytic sites of Pd_x-Ce_{1-x}O_{2-δ} for dehydrogenation, oxygen insertion and reverse water gas shift reactions during methane combustion. *Applied Catalysis B: Environmental* **2020**, *275*, 119118. DOI: <https://doi.org/10.1016/j.apcatb.2020.119118>.
- (123) He, Y.; Guo, F.; Yang, K. R.; Heinlein, J. A.; Bamonte, S. M.; Fee, J. J.; Hu, S.; Suib, S. L.; Haller, G. L.; Batista, V. S. In situ identification of reaction intermediates and mechanistic understandings of methane oxidation over hematite: A combined experimental and theoretical study. *Journal of the American Chemical Society* **2020**, *142* (40), 17119-17130. (124) Qi, W.; Huang, Z.; Chen, Z.; Fu, L.; Zhang, Z. Experimental and theoretical investigation of oxidative methane activation on Pd–Pt catalysts. *RSC advances* **2019**, *9* (20), 1138511395.
- (125) Ciuparu, D.; Altman, E.; Pfefferle, L. Contributions of Lattice Oxygen in Methane Combustion over PdO-Based Catalysts. *Journal of Catalysis* **2001**, *203* (1), 64-74. DOI: <https://doi.org/10.1006/jcat.2001.3331>.
- (126) Müller, C. A.; Maciejewski, M.; Koepfel, R. A.; Tschan, R.; Baiker, A. Role of lattice oxygen in the combustion of methane over PdO/ZrO₂: combined pulse TG/DTA and MS study with ¹⁸O-labeled catalyst. *The Journal of Physical Chemistry* **1996**, *100* (51), 2000620014.
- (127) Au-Yeung, J.; Chen, K.; Bell, A. T.; Iglesia, E. Isotopic studies of methane oxidation pathways on PdO catalysts. *Journal of Catalysis* **1999**, *188* (1), 132-139.
- (128) Schwartz, W. R.; Pfefferle, L. D. Combustion of Methane over Palladium-Based Catalysts: Support Interactions. *The Journal of Physical Chemistry C* **2012**, *116* (15), 85718578. DOI: 10.1021/jp2119668.
- (129) Stotz, H.; Maier, L.; Boubnov, A.; Gremminger, A. T.; Grunwaldt, J. D.; Deutschmann, O. Surface reaction kinetics of methane oxidation over PdO. *Journal of Catalysis* **2019**, *370*, 152-175. DOI: <https://doi.org/10.1016/j.jcat.2018.12.007>.
- (130) Ciuparu, D.; Lyubovsky, M. R.; Altman, E.; Pfefferle, L. D.; Datye, A. CATALYTIC COMBUSTION OF METHANE OVER PALLADIUM-BASED CATALYSTS. *Catalysis Reviews* **2002**, *44* (4), 593-649. DOI: 10.1081/CR-120015482.
- (131) Jiang, D.; Khivantsev, K.; Wang, Y. Low-Temperature Methane Oxidation for Efficient Emission Control in Natural Gas Vehicles: Pd and Beyond. *ACS Catalysis* **2020**, *10* (23), 14304-14314. DOI: 10.1021/acscatal.0c03338.
- (132) Bernard, P.; Stelmachowski, P.; Broś, P.; Makowski, W.; Kotarba, A. Demonstration of the Influence of Specific Surface Area on Reaction Rate in Heterogeneous Catalysis. *Journal of Chemical Education* **2021**, *98* (3), 935-940. DOI: 10.1021/acs.jchemed.0c01101. (133) Firth, J. G.; Holland, H. B. Catalytic oxidation of methane on zeolites containing rhodium, iridium, palladium and platinum. *Transactions of the Faraday Society* **1969**, *65*, 1891-1896. DOI: 10.1039/TF9696501891.
- (134) Li, Y.; Armor, J. N. Catalytic combustion of methane over palladium exchanged zeolites. *Applied Catalysis B: Environmental* **1994**, *3* (4), 275-282. DOI: [https://doi.org/10.1016/0926-3373\(94\)0006Z-H](https://doi.org/10.1016/0926-3373(94)0006Z-H).
- (135) Friberg, I.; Clark, A. H.; Ho, P. H.; Sadokhina, N.; Smales, G. J.; Woo, J.; Auvray, X.; Ferri, D.; Nachttegaal, M.; Kröcher, O.; et al. Structure and performance of zeolite supported Pd for complete methane oxidation. *Catalysis Today* **2021**, *382*, 3-12. DOI: <https://doi.org/10.1016/j.cattod.2020.11.026>.
- (136) Khivantsev, K.; Jaegers, N. R.; Kovarik, L.; Wang, M.; Hu, J. Z.; Wang, Y.; Derewinski, M.

- A.; Szanyi, J. The superior hydrothermal stability of Pd/SSZ-39 in low temperature passive NO_x adsorption (PNA) and methane combustion. *Applied Catalysis B: Environmental* **2021**, *280*, 119449. DOI: <https://doi.org/10.1016/j.apcatb.2020.119449>.
- (137) Friberg, I.; Sadokhina, N.; Olsson, L. The effect of Si/Al ratio of zeolite supported Pd for complete CH₄ oxidation in the presence of water vapor and SO₂. *Applied Catalysis B: Environmental* **2019**, *250*, 117-131. DOI: <https://doi.org/10.1016/j.apcatb.2019.03.005>. (138) Lim, J. B.; Jo, D.; Hong, S. B. Palladium-exchanged small-pore zeolites with different cage systems as methane combustion catalysts. *Applied Catalysis B: Environmental* **2017**, *219*, 155-162. DOI: <https://doi.org/10.1016/j.apcatb.2017.07.032>.
- (139) Said Zina, M.; Ghorbel, A. Preparation and characterization of bimetallic PdMo/γ zeolite: catalytic properties in methane combustion. *Solid State Sciences* **2004**, *6* (9), 973980. DOI: <https://doi.org/10.1016/j.solidstatesciences.2004.04.013>.
- (140) Nomura, K.; Noro, K.; Nakamura, Y.; Yazawa, Y.; Yoshida, H.; Satsuma, A.; Hattori, T. Pd-Pt bimetallic catalyst supported on SAPO-5 for catalytic combustion of diluted methane in the presence of water vapor. *Catalysis Letters* **1998**, *53* (3-4), 167-169. DOI: 10.1023/a:1019082611978.
- (141) Park, J. H.; Kim, B.; Shin, C. H.; Seo, G.; Kim, S. H.; Hong, S. B. Methane combustion over Pd catalysts loaded on medium and large pore zeolites. *Topics in Catalysis* **2009**, *52* (12), 27-34. DOI: 10.1007/s11244-008-9135-7.
- (142) de Correa, C. M.; Ai'da Luz Villa, H. Combustion of methane over palladium ZSM-5 and mordenite catalysts. *Applied Catalysis B: Environmental* **1996**, *10* (4), 313-323. DOI: [https://doi.org/10.1016/S0926-3373\(96\)00039-2](https://doi.org/10.1016/S0926-3373(96)00039-2).
- (143) Korde, A.; Min, B.; Almas, Q.; Chiang, Y.-D.; Nair, S.; Jones, C. Effect of Si/Al Ratio on the Catalytic Activity of Two-Dimensional MFI Nanosheets in Aromatic Alkylation and Alcohol Etherification. *ChemCatChem* **2019**, *11*. DOI: 10.1002/cctc.201901042. (144) Wang, J.-g.; Liu, C.-j. Density functional theory study of methane activation over PdO/HZSM-5. *Journal of Molecular Catalysis A: Chemical* **2006**, *247* (1-2), 199-205. (145) Okumura, K.; Matsumoto, S.; Nishiaki, N.; Niwa, M. Support effect of zeolite on the methane combustion activity of palladium. *Applied Catalysis B: Environmental* **2003**, *40* (2), 151-159.
- (146) Zachariou, A.; Hawkins, A. P.; Howe, R. F.; Skakle, J. M. S.; Barrow, N.; Collier, P.; Nye, D. W.; Smith, R. I.; Stenning, G. B. G.; Parker, S. F.; et al. Counting the Acid Sites in a Commercial ZSM-5 Zeolite Catalyst. *ACS Physical Chemistry Au* **2023**, *3* (1), 74-83. DOI: 10.1021/acspchemau.2c00040.
- (147) Lapisardi, G.; Urfels, L.; Gélín, P.; Primet, M.; Kaddouri, A.; Garbowski, E.; Toppi, S.; Tena, E. Superior catalytic behaviour of Pt-doped Pd catalysts in the complete oxidation of methane at low temperature. *Catalysis Today* **2006**, *117* (4), 564-568. DOI: <https://doi.org/10.1016/j.cattod.2006.06.004>.
- (148) Doyle, A. M.; Postolache, R.; Shaw, D.; Rothon, R.; Tosheva, L. Methane oxidation over zeolite catalysts prepared from geothermal fluids. *Microporous and Mesoporous Materials* **2019**, *285*, 56-60. DOI: <https://doi.org/10.1016/j.micromeso.2019.04.069>.
- (149) Alketan, O.; Pelanconi, M.; Ortona, A.; Abu Al-Rub, R. Additive manufacturing of architected catalytic ceramic substrates based on triply periodic minimal surfaces. *Journal of the American Ceramic Society* **2019**, *102*. DOI: 10.1111/jace.16474.
- (150) Manzano, J. S.; Wang, H.; Slowing, I. I. High Throughput Screening of 3D Printable Resins: Adjusting the Surface and Catalytic Properties of Multifunctional Architectures. *ACS Applied Polymer Materials* **2019**, *1* (11), 2890-2896. DOI: 10.1021/acsapm.9b00598.

- (151) Kovacev, N.; Li, S.; Zeraati-Rezaei, S.; Hemida, H.; Tsolakis, A.; Essa, K. Effects of the internal structures of monolith ceramic substrates on thermal and hydraulic properties: additive manufacturing, numerical modelling and experimental testing. *The International Journal of Advanced Manufacturing Technology* **2021**, *112* (3), 1115-1132. DOI: 10.1007/s00170-020-06493-2.
- (152) Kovacev, N.; Li, S.; Li, W.; Zeraati-Rezaei, S.; Tsolakis, A.; Essa, K. Additive Manufacturing of Novel Hybrid Monolithic Ceramic Substrate. *Aerospace Engineering* **2022**, *9*. DOI: 10.3390/aerospace9050255.
- (153) Van Noyen, J.; De Wilde, A.; Schroeven, M.; Mullens, S.; Luyten, J. Ceramic Processing Techniques for Catalyst Design: Formation, Properties, and Catalytic Example of ZSM-5 on 3Dimensional Fiber Deposition Support Structures. *International Journal of Applied Ceramic Technology* **2012**, *9* (5), 902-910, <https://doi.org/10.1111/j.1744-7402.2012.02781.x>. DOI: <https://doi.org/10.1111/j.1744-7402.2012.02781.x> (accessed 2022/11/24).
- (154) Stuecker, J. N.; Miller, J. E.; Ferrizz, R. E.; Mudd, J. E.; Cesarano, J. Advanced Support Structures for Enhanced Catalytic Activity. *Industrial & Engineering Chemistry Research* **2004**, *43* (1), 51-55. DOI: 10.1021/ie030291v.
- (155) Leclerc, C.; Gudgila, R. Short Contact Time Catalytic Partial Oxidation of Methane over Rhodium Supported on Ceria Based 3-D Printed Supports. *Industrial & Engineering Chemistry Research* **2019**, *58*. DOI: 10.1021/acs.iecr.9b01169.
- (156) Hajimirzaee, S.; Shaw, D.; Howard, P.; Doyle, A. Industrial scale 3D printed catalytic converter for emissions control in a dual-fuel heavy-duty engine. *Chemical Engineering Science* **2020**, *231*, 116287. DOI: 10.1016/j.ces.2020.116287.
- (157) Griffith, M. L.; Halloran, J. W. Ultraviolet curing of highly loaded ceramic suspensions for stereolithography of ceramics. In *Proc. Solid Freeform Fabr. Symp*, 1994; pp 396-403.
- (158) Griffith, M. L.; Halloran, J. Freeform Fabrication of Ceramics Via Stereolithography. *Journal of the American Ceramic Society* **1996**, *79*, 2601-2608.
- (159) Smirnov, A.; Chugunov, S.; Kholodkova, A.; Isachenkov, M.; Tikhonov, A.; Dubinin, O.; Shishkovsky, I. The Fabrication and Characterization of BaTiO₃ Piezoceramics Using SLA 3D Printing at 465 nm Wavelength. *Materials* **2022**, *15* (3), 960.
- (160) Bai, X.; Ding, G.; Zhang, K.; Wang, W.; Zhou, N.; Fang, D.; He, R. Stereolithography additive manufacturing and sintering approaches of SiC ceramics. *Open Ceramics* **2021**, *5*, 100046. DOI: <https://doi.org/10.1016/j.oceram.2020.100046>.
- (161) Liu, C.; Qian, B.; Liu, X.; Tong, L.; Qiu, J. Additive manufacturing of silica glass using laser stereolithography with a top-down approach and fast debinding. *RSC advances* **2018**, *8* (29), 16344-16348.
- (162) Komissarenko, D. A.; Sokolov, P. S.; Evstigneeva, A. D.; Shmeleva, I. A.; Dosovitsky, A. E. Rheological and curing behavior of acrylate-based suspensions for the DLP 3D printing of complex zirconia parts. *Materials* **2018**, *11* (12), 2350.
- (163) Sun, J.; Binner, J.; Bai, J. 3D printing of zirconia via digital light processing: optimization of slurry and debinding process. *Journal of the European Ceramic Society* **2020**, *40* (15), 5837-5844. DOI: <https://doi.org/10.1016/j.jeurceramsoc.2020.05.079>.
- (164) Azarmi, F.; Amiri, A. Microstructural evolution during fabrication of alumina via laser stereolithography technique. *Ceramics International* **2019**, *45* (1), 271-278.
- (165) Xing, Z.; Liu, W.; Chen, Y.; Li, W. Effect of plasticizer on the fabrication and properties of alumina ceramic by stereolithography-based additive manufacturing. *Ceramics International* **2018**, *44* (16), 19939-19944.

- (166) Zimbeck, W.; Rice, R. Stereolithography of ceramics and metals. In *IS AND T ANNUAL CONFERENCE*, 1997; THE SOCIETY FOR IMAGING SCIENCE AND TECHNOLOGY: pp 649-655.
- (167) Sun, J.; Binner, J.; Bai, J. Effect of surface treatment on the dispersion of nano zirconia particles in non-aqueous suspensions for stereolithography. *Journal of the European Ceramic Society* **2019**, *39* (4), 1660-1667.
- (168) Sun, C.; Zhang, X. Experimental and numerical investigations on microstereolithography of ceramics. *Journal of Applied Physics* **2002**, *92* (8), 4796-4802.
- (169) Bae, C.-J.; Halloran, J. W. Integrally Cored Ceramic Mold Fabricated by Ceramic Stereolithography. *International Journal of Applied Ceramic Technology* **2011**, *8* (6), 1255-1262, <https://doi.org/10.1111/j.1744-7402.2010.02568.x>. DOI: <https://doi.org/10.1111/j.1744-7402.2010.02568.x> (accessed 2021/03/04).
- (170) Zhang, K.; Xie, C.; Wang, G.; He, R.; Ding, G.; Wang, M.; Dai, D.; Fang, D. High solid loading, low viscosity photosensitive Al₂O₃ slurry for stereolithography based additive manufacturing. *Ceramics International* **2019**, *45* (1), 203-208. DOI: <https://doi.org/10.1016/j.ceramint.2018.09.152>.
- (171) Li, X.; Hu, K.; Lu, Z. Effect of light attenuation on polymerization of ceramic suspensions for stereolithography. *Journal of the European Ceramic Society* **2019**, *39* (7), 2503-2509.
- (172) Zhang, K.; He, R.; Xie, C.; Wang, G.; Ding, G.; Wang, M.; Song, W.; Fang, D. Photosensitive ZrO₂ suspensions for stereolithography. *Ceramics International* **2019**, *45* (9), 12189-12195.
- (173) Goswami, A.; Ankit, K.; Balashanmugam, N.; Umarji, A. M.; Madras, G. Optimization of rheological properties of photopolymerizable alumina suspensions for ceramic microstereolithography. *Ceramics International* **2014**, *40* (2), 3655-3665.
- (174) Papetti, V.; Dimopoulos Eggenschwiler, P.; Della Torre, A.; Lucci, F.; Ortona, A.; Montenegro, G. Additive Manufactured open cell polyhedral structures as substrates for automotive catalysts. *International Journal of Heat and Mass Transfer* **2018**, *126*, 10351047. DOI: <https://doi.org/10.1016/j.ijheatmasstransfer.2018.06.061>.
- (175) Kovacev, N.; Doustdar, O.; Li, S.; Tsolakis, A.; Herreros, J. M.; Essa, K. The synergy between substrate architecture of 3D-printed catalytic converters and hydrogen for lowtemperature aftertreatment systems. *Chemical Engineering Science* **2023**, *269*, 118490. DOI: <https://doi.org/10.1016/j.ces.2023.118490>.
- (176) Oh, G.-J.; Yun, K.-D.; Lee, K.-M.; Lim, H.-P.; Park, S.-W. Sintering behavior and mechanical properties of zirconia compacts fabricated by uniaxial press forming. *J Adv Prosthodont* **2010**, *2* (3), 81-87.
- (177) Powder pattern simulations of disordered intergrowths. In *Collection of Simulated XRD Powder Patterns for Zeolites (Fifth Edition)*, Treacy, M. M. J., Higgins, J. B. Eds.; Elsevier Science B.V., 2007; pp 477-485.
- (178) Scintag, I. Chapter 7: Basics of X-ray Diffraction. *Providing Solution To Your Diffraction Needs* **1999**, 7.1-7.24.
- (179) Edington, J. W. Electron diffraction in the electron microscope. In *Electron Diffraction in the Electron Microscope*, Springer, 1975; pp 1-77.
- (180) Hammond, C. 135 Describing lattice planes and directions in crystals: Miller indices and zone axis symbols. In *The Basics of Crystallography and Diffraction*, Oxford University Press, 2015; p 0.
- (181) Giacobozzo, C.; Monaco, H. L.; Artioli, G.; Viterbo, D.; Milanesio, M.; Gilli, G.; Gilli, P.; Zanotti, G.; Ferraris, G.; Catti, M. 1573 The diffraction of X-rays by crystals. In *Fundamentals of Crystallography*, Giacobozzo, C. Ed.; Oxford University Press, 2011; p 0.

- (182) Ewald, P. P. The Principles of X-ray Diffraction. In *Fifty Years of X-Ray Diffraction: Dedicated to the International Union of Crystallography on the Occasion of the Commemoration Meeting in Munich July 1962*, Ewald, P. P. Ed.; Springer US, 1962; pp 82101.
- (183) Henry, D.; Eby, N.; Goodge, J.; Mogk, D. *X-Ray reflection in accordance with Bragg's Law*. 2016. (accessed 2022).
- (184) Le Pevelen, D. D. Small Molecule X-Ray Crystallography, Theory and Workflow. In *Encyclopedia of Spectroscopy and Spectrometry (Second Edition)*, Lindon, J. C. Ed.; Academic Press, 2010; pp 2559-2576.
- (185) Walton, K. S.; Snurr, R. Q. Applicability of the BET Method for Determining Surface Areas of Microporous Metal–Organic Frameworks. *Journal of the American Chemical Society* **2007**, *129* (27), 8552-8556. DOI: 10.1021/ja071174k.
- (186) Palchoudhury, S.; Baalousha, M.; Lead, J. R. Chapter 5 - Methods for Measuring Concentration (Mass, Surface Area and Number) of Nanomaterials. In *Frontiers of Nanoscience*, Baalousha, M., Lead, J. R. Eds.; Vol. 8; Elsevier, 2015; pp 153-181. (187) Lowell, S.; Shields, J.; Thomas, M.; Thommes, M. Surface Area Analysis from the Langmuir and BET Theories. 2004; pp 58-81.
- (188) Dollimore, D.; Spooner, P.; Turner, A. The bet method of analysis of gas adsorption data and its relevance to the calculation of surface areas. *Surface Technology* **1976**, *4* (2), 121-160. DOI: [https://doi.org/10.1016/0376-4583\(76\)90024-8](https://doi.org/10.1016/0376-4583(76)90024-8).
- (189) R. Barron, A.; M. V. Pavan, R. *BET Surface Area Analysis of Nanoparticles*. Chemistry LibreTexts, 2021. (accessed 2022 June).
- (190) *ASAP 2020 Developer/Analyst Operator's Manual*; 2015.
- (191) Reimer, L. Introduction. In *Scanning Electron Microscopy: Physics of Image Formation and Microanalysis*, Reimer, L. Ed.; Springer Berlin Heidelberg, 1998; pp 1-12.
- (192) Mohammed, A.; Abdullah, A. *Scanning Electron Microscopy (SEM): A Review*; 2019.
- (193) Nano Science Instruments. *Scanning Electron Microscope*. (accessed 2022).
- (194) Naeem, H. *Microstructure and Corrosion in Welded Aluminium Alloys*. 2019.
- (195) Reimer, L. Emission of Backscattered and Secondary Electrons. In *Scanning Electron Microscopy: Physics of Image Formation and Microanalysis*, Reimer, L. Ed.; Springer Berlin Heidelberg, 1998; pp 135-169.
- (196) JEOL. *SEM Scanning Electron Microscope A to Z: Basic Knowledge for Using the SEM*.
- (197) Usman, M.; Alotaibi, F.; Aslam, R. Dehydrogenation–hydrogenation of methylcyclohexane-toluene system on 1.0 wt% Pt/zeolite beta catalyst. *Progress in Reaction Kinetics and Mechanism* **2015**, *40*, 353-366. DOI: 10.3184/146867815X14413752286029.
- (198) Potts, P. J. X-ray fluorescence analysis: principles and practice of wavelength dispersive spectrometry. In *A Handbook of Silicate Rock Analysis*, Potts, P. J. Ed.; Springer Netherlands, 1987; pp 226-285.
- (199) Chen, Z.; Gibson, W. M.; Huang, H. High definition x-ray fluorescence: principles and techniques. *X-ray Optics and Instrumentation* **2008**, *2008*.
- (200) Analytical Methods Committee, A. N. X-ray fluorescence (XRF) analysis of porcelain: Background paper. *Analytical Methods* **2017**, *9* (16), 2371-2374, 10.1039/C7AY90044A. DOI: 10.1039/C7AY90044A.
- (201) Oyedotun, T. D. T. X-ray fluorescence (XRF) in the investigation of the composition of earth materials: a review and an overview. *Geology, Ecology, and Landscapes* **2018**, *2* (2), 148-154. DOI: 10.1080/24749508.2018.1452459.
- (202) Lim, S. X-Ray Fluorescence (XRF) Analyzer - Theory, Utility, and QA/QC for Environmental and Commercial Product Samples in Cambodia. https://digitalcommons.buffalostate.edu/multistudies_theses/8/, 2013.

- (203) Brown, M. E.; Gallagher, P. K. Chapter 1 - Introduction to Recent Advances, Techniques and Applications of Thermal Analysis and Calorimetry. In *Handbook of Thermal Analysis and Calorimetry*, Brown, M. E., Gallagher, P. K. Eds.; Vol. 5; Elsevier Science B.V., 2008; pp 1-12. (204) Bottom, R. Thermogravimetric Analysis. *Principles and Applications of Thermal Analysis* **2008**, 87-118, <https://doi.org/10.1002/9780470697702.ch3>. DOI: <https://doi.org/10.1002/9780470697702.ch3> (accessed 2022/08/25).
- (205) *TGA 4000 Thermogravimetric Analyzer*; 2017.
- (206) *Thermogravimetric Analysis A Beginner's Guide*; 2015.
- (207) Besendörfer, G.; Roosen, A.; Modes, C.; Betz, T. Factors Influencing the Green Body Properties and Shrinkage Tolerance of LTCC Green Tapes. *International Journal of Applied Ceramic Technology* **2007**, 4 (1), 53-59, <https://doi.org/10.1111/j.1744-7402.2007.02119.x>. DOI: <https://doi.org/10.1111/j.1744-7402.2007.02119.x> (accessed 2022/08/25).
- (208) Song, S.; Gao, Z.; Xu, H.; Bao, C.; Lu, B.; Zheng, B.; Dong, W.; Ma, H. Rapid preparation and performance of degradable ceramic scaffolds based on stereolithography. *Journal of Asian Ceramic Societies* **2022**, 10 (1), 58-68. DOI: 10.1080/21870764.2021.2008102.
- (209) Huang, X.; Dai, H.; Hu, Y.; Zhuang, P.; Shi, Z.; Ma, Y. Development of a high solid loading β -TCP suspension with a low refractive index contrast for DLP -based ceramic stereolithography. *Journal of the European Ceramic Society* **2021**, 41 (6), 3743-3754. DOI: <https://doi.org/10.1016/j.jeurceramsoc.2020.12.047>.
- (210) Hidber, P. C.; Graule, T. J.; Gauckler, L. J. Influence of the dispersant structure on properties of electrostatically stabilized aqueous alumina suspensions. *Journal of the European Ceramic Society* **1997**, 17 (2), 239-249. DOI: [https://doi.org/10.1016/S09552219\(96\)00151-3](https://doi.org/10.1016/S09552219(96)00151-3).
- (211) Chen, Z.; Li, J.; Liu, C.; Liu, Y.; Zhu, J.; Lao, C. Preparation of high solid loading and low viscosity ceramic slurries for photopolymerization-based 3D printing. *Ceramics International* **2019**. DOI: 10.1016/j.ceramint.2019.03.024.
- (212) Ding, G.; He, R.; Zhang, K.; Xia, M.; Feng, C.; Fang, D. Dispersion and stability of SiC ceramic slurry for stereolithography. *Ceramics International* **2020**, 46 (4), 4720-4729. DOI: <https://doi.org/10.1016/j.ceramint.2019.10.203>.
- (213) Liao, H. *Stereolithography using compositions containing ceramic powders*; University of Toronto, 1998.
- (214) Jakubiak, J.; Rabek, J. Three-dimensional (3D) photopolymerization in stereolithography - Part I. Fundamentals of 3D photopolymerization. *Polimery/Polymers* **2000**, 45, 759-770. DOI: 10.14314/polimery.2000.759.
- (215) Zakeri, S.; Vippola, M.; Levänen, E. A comprehensive review of the photopolymerization of ceramic resins used in stereolithography. *Additive Manufacturing* **2020**, 35, 101177. DOI: <https://doi.org/10.1016/j.addma.2020.101177>.
- (216) Pfaffinger, M.; Mitteramskogler, G.; Gmeiner, R.; Stampfl, J. Thermal debinding of ceramic-filled photopolymers. In *Materials Science Forum*, 2015; Trans Tech Publ: Vol. 825, pp 75-81.
- (217) Krongauz, V. Diffusion in polymers dependence on crosslink density. Eyring approach to mechanism. *Journal of Thermal Analysis and Calorimetry - J THERM ANAL CALORIM* **2010**, 102, 435-445. DOI: 10.1007/s10973-010-0922-6.
- (218) Eing, K.; Johar, B.; Ho, L.; Zabar, Y. Influence of Sintering Temperature on Crystallization Behavior of Cordierite synthesized from Non-Stoichiometric Formulation. In *MATEC Web of Conferences*, 2016; EDP Sciences: Vol. 78, p 01099.

- (219) Powder pattern identification table. In *Collection of Simulated XRD Powder Patterns for Zeolites (Fifth Edition)*, Treacy, M. M. J., Higgins, J. B. Eds.; Elsevier Science B.V., 2007; pp 10-16.
- (220) Sim, J.-H.; Koo, B.-K.; Jung, M.; Kim, D.-S. Study on Debinding and Sintering Processes for Ceramics Fabricated Using Digital Light Processing (DLP) 3D Printing. *Processes* **2022**, *10*, 2467. DOI: 10.3390/pr10112467.
- (221) Kovalenko, I.; Ramachandran, Y.; Garan, M. Experimental shrinkage study of ceramic DLP 3D printed parts after firing green bodies in a KILN. *MM Science Journal* **2019**, *2019*, 2767-2771. DOI: 10.17973/MMSJ.2019_03_2018113.
- (222) Banerjee, C. A.; Golub, W. K.; Hakim, A. M.; Billor, Z. M. Comparative Study of the Characteristics and Activities of Pd/ γ -Al₂O₃ Catalysts Prepared by Vortex and Incipient Wetness Methods. *Catalysts* **2019**, *9* (4). DOI: 10.3390/catal9040336.
- (223) Doyle, A.; Postolache, R.; Shaw, D.; Rothon, R.; Tosheva, L. Methane oxidation over zeolite catalysts prepared from geothermal fluids. *Microporous and Mesoporous Materials* **2019**, *285*. DOI: 10.1016/j.micromeso.2019.04.069.
- (224) Kamieniak, J.; Kelly, P. J.; Banks, C. E.; Doyle, A. M. Methane emission management in a dual-fuel engine exhaust using Pd and Ni hydroxyapatite catalysts. *Fuel* **2017**, *208*, 314320. DOI: <https://doi.org/10.1016/j.fuel.2017.07.012>.
- (225) Balzarotti, R.; Cristiani, C.; Francis, L. F. Combined dip-coating/spin-coating depositions on ceramic honeycomb monoliths for structured catalysts preparation. *Catalysis Today* **2019**, *334*, 90-95. DOI: <https://doi.org/10.1016/j.cattod.2019.01.037>.
- (226) Ibáñez, M.; Sanz, O.; Egaña, A.; Reyero, I.; Bimbela, F.; Gandía, L. M.; Montes, M. Performance comparison between washcoated and packed-bed monolithic reactors for the low-temperature Fischer-Tropsch synthesis. *Chemical Engineering Journal* **2021**, *425*, 130424. DOI: <https://doi.org/10.1016/j.cej.2021.130424>.
- (227) Stutz, M. J.; Poulikakos, D. Optimum washcoat thickness of a monolith reactor for syngas production by partial oxidation of methane. *Chemical Engineering Science* **2008**, *63* (7), 1761-1770. DOI: <https://doi.org/10.1016/j.ces.2007.11.032>.
- (228) Davo-Quinonero, A.; Sorolla-Rosario, D.; Bailon-Garcia, E.; Lozano-Castello, D.; BuenoLopez, A. Improved asymmetrical honeycomb monolith catalyst prepared using a 3D printed template. *Journal of hazardous materials* **2019**, *368*, 638-643.
- (229) Quintanilla, A.; Vega, G.; López, P.; García, F.; Madurga, E.; Belmonte, M.; Casas, J. A. Enhanced Fluid Dynamics in 3D Monolithic Reactors to Improve the Chemical Performance: Experimental and Numerical Investigation. *Industrial & Engineering Chemistry Research* **2021**, *60* (41), 14701-14712. DOI: 10.1021/acs.iecr.1c03098.